VERSATILE SPIN-WAVE APPROACHES TO THE SPIN DYNAMICS OF TRANSITION-METAL INSULATORS

A Thesis
Presented to
The Academic Faculty

By

Luwei Ge

In Partial Fulfillment
of the Requirements for the Degree
Doctor of Philosophy in the
School of Physics

Georgia Institute of Technology

May 2020

VERSATILE SPIN-WAVE APPROACHES TO THE SPIN DYNAMICS OF TRANSITION-METAL INSULATORS

Approved by:

Dr. Martin Mourigal, Advisor
School of Physics
Georgia Institute of Technology

Dr. Dragomir Davidovic
School of Physics
Georgia Institute of Technology

Dr. Michael Pustilnik
School of Physics
Georgia Institute of Technology

Dr. Zhigang Jiang
School of Physics
Georgia Institute of Technology

Dr. Martin Maldovan
School of Chemical & Biomolecular Engineering
Georgia Institute of Technology

Date Approved: March 11, 2020

The fundamental cause of the trouble is that in the modern world the stupid are cocksure while the intelligent are full of doubt.

Bertrand Russell

To my parents.

ACKNOWLEDGEMENTS

I am extremely grateful to my parents, Yuming and Linying, for their love, caring and sacrifices for making me an educated person who stays curious with knowledge. I am very thankful to my wife, Huiwen, for her understanding and continuing support to my research work.

I would like to express my sincere gratitude to my advisor, Martin, for offering me the chance of exploring the rich physics of quantum magnetism. Many baffling yet important concepts got demystified through numerous conversations with him. It was a great privilege and honor to work under his supervision.

Nowadays almost no research work can be accomplished by a single person. Through the journey of my research, tremendous help was received from many collaborators. Namely, I would like to thank Joe, Yoshi, Jie and Qing for their involvement on different parts of the projects. It was very pleasant working and collaborating with them.

I would like to thank my friends, Yiran, Jeremy, Xiaojian, Marcus, Zhiling and Sai, the friendship with whom has made the journey so wonderful.

TABLE OF CONTENTS

LIST OF FIGURES

SUMMARY

Quantum magnetism is one of the most important branches in condensed matter physics because it serves as an excellent platform to realize model quantum many-body systems which are difficult to find elsewhere. Good understanding of the nature of magnetic excitations in such systems demands both experimental and theoretical efforts. This thesis presents comprehensive studies of the magnetic properties of several $3d$ transition-metal oxides. Primarily relying on advances in neutron scattering instrumentation and spin-wave theory, the work carefully examines the effectiveness of the theory of weakly interacting magnons in describing the elementary magnetic excitations of these insulators. By revealing the microscopic interactions of these systems and testing the applicability of spin-wave theory quantitatively, the work also hopes to offer useful insights or guidance to future investigations.

The thesis comprises six chapters. The first chapter is centered around the $3d$ transition-metal oxides and introduces the origin of the magnetism, and the concepts of magnetic ordering with many-body nature and elementary magnetic excitations. The second chapter introduces the neutron scattering technique by formalizing the scattering cross section as well as presenting typical inelastic neutron scattering spectrometers. Chapters 3 to 5 present the detailed work on different compounds and discuss about their magnetic properties and the usefulness of spin-wave theory to understand their spin dynamics in detail. The last chapter gives a holistic conclusion and outlook on all demonstrated work.

CHAPTER 1

MAGNETISM IN $3D$ TRANSITION-METAL OXIDES

1.1 Origin of magnetic moments in $3d$ transition-metal elements

The magnetism of $3d$ transition-metal elements and the derived insulating solids originate from the partially filled $3d$ orbital shell of the constituting ions. The presence of localized magnetic moments stems from the angular momentum of all the $3d$ electrons as well as their charge. The single-electron orbital angular momentum quantum number is usually denoted l and the spin denoted s. Capital letters L and S are the sum of all electrons and J refers to the total angular momentum.

Three factors interplay in this single-ion picture: (1) the Coulomb repulsion between electrons; (2) the coupling between the electronic spin and its orbit (spin-orbit coupling); (3) the electric potential from the environment when the ion is located in a crystal (crystal electric field). It would require solving the Dirac equation for those electrons to gain a precise knowledge. This is obviously a challenging task and not always feasible. Fortunately, phenomenological rules, which often work well to describe things, have been developed.

The notorious Hund's rules take into account the effect of the Coulomb repulsion and the spin-orbit coupling on the energy of the orbitals. These rules for a partially filled orbitals are the following: (1) the value of the sum of the electron spins on the orbitals is maximal; (2) the value of the sum of the orbital angular momentum is maximal; (3) if the orbitals are less than half filled the total angular momentum is $J = |L - S|$, if the orbitals are more than half filled then $J = L + S$. The third rule is the result of the spin-orbit coupling.

Hund's rules work well for free ions but do not consider the crystal electric field. Because the symmetry in a crystal is discrete and lower than the spherically symmetric Coulomb potential, some terms in the spherical harmonics have to vanish. Empirically,

crystal field prefers zero L while spin-orbit coupling as we have seen from the Hund's rules favors large L. $3d$ transition elements typically have dominant crystal field while spin-orbit coupling is sub-leading. Therefore, the so-called angular momentum quenching occurs and the magnetization can be explained with $L = 0$ and $J = S$. Consequentially, most of the Cu^{2+} oxides can be safely assumed to possess a spin-$\frac{1}{2}$ degree of freedom and Co^{2+} with spin-$\frac{3}{2}$. There are exceptions sometimes including the case which will be introduced in Chapter. IV.

1.2 Magnetic ordering with many-body origin

While the single-ion magnetism is itself an interesting subject, it is far from occupying the whole picture. The many-body nature of the interactions between magnetic moments is the source of almost all fascinating phenomena observed in quantum magnetism. Essentially, electronic wave functions across ions have a finite direct or indirect overlap.

A practical starting point to understand this phenomenom is the single-band Hubbard model [1]. It should be thought of as an effective model for low energies and temperatures. It has the following generic form,

$$\mathcal{H} = -\sum_{i,j} t_{ij} \left(a^\dagger_{i\uparrow} a_{j\uparrow} + a^\dagger_{i\downarrow} a_{j\downarrow} \right) + U \sum_i n_{i\uparrow} n_{i\downarrow}, \tag{1.1}$$

where $a^\dagger_i$ and a_i are the creation and annihilation operators for electrons in the second-quantized language. $n_i \equiv a^\dagger_i a_i$ is the number operator. $\uparrow$ and $\downarrow$ denote the spin polarizations. This is evidently a model living on a lattice system. $t_{i,j}$ represents the hopping of electrons from site-i to site-j, while $U > 0$ is the Coulomb repulsion of electrons on the same site. Note that people do study as well the negative-U Hubbard model where "Coulomb repulsion" will no longer be an appropriate phrase to describe U.

In insulating magnets, the large-U limit can be applied to derive the so-called t-J model,

the surviving term of which in the half-filled limit $n_i = 1$ is,

$$\mathcal{H} = \sum_{i,j} J_{ij} \mathbf{S}_i \cdot \mathbf{S}_j, \tag{1.2}$$

which is the quantum Heisenberg model [2]. $\mathbf{S}_i$ represents the spin operators associated with the localized magnetic moments. $J_{ij} \equiv 4t_{ij}^2/U > 0$ is the antiferromagnetic exchange interaction. The reason it is always antiferromagnetic here is due to the case represented by the Hubbard model being too simplistic. As far as a general transition metal oxide is concerned, the electron hopping is mediated through the p orbitals of the oxygens as well as the d orbitals of the ions. Depending on the geometrical configuration of the orbitals, the resulting exchanges can become either antiferromagnetic or ferromagnetic. In cases where the inversion symmetry is broken around the center of the bond, the anti-symmetric interaction which appears as a Dzyaloshinki-Moriya term may also occur.

It is difficult to compute those interaction parameters using first-principle approaches such that when applying those models researchers are usually guided by the system symmetry and rely on experiments to reversely establish a well-defined understanding. Nevertheless, it is important and indeed beneficial to know the path from which these models originate. For example, in the context of high-temperature superconducting copper oxides such as the parent compound La_2CuO_4 [3], the effect of electron or hole doping which deviates the system from the half-filled limit has been intensively studied and remains as an attractive subject.

One fundamental phenomenon originating from those interactions between localized spins is the magnetic ordering, which normally refers to dipolar magnetic moment correlations. Apart from the trivial ferromagnetic case, the most conventional magnetic order is the collinear antiferromagnetic order or Néel order [Figure 1.1(left)] where the nearest-neighbor spins are anti-parallel with each other to lower the bonding energy. The situation can become more interesting with the introduction of another important concept, magnetic

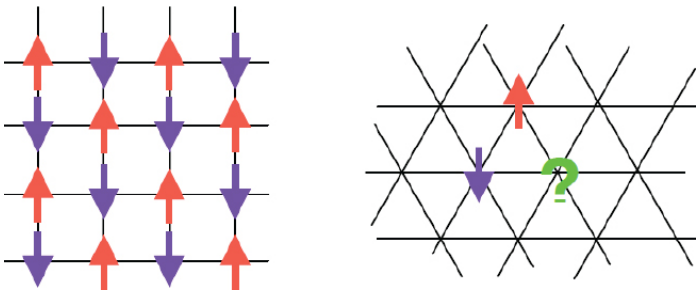

Figure 1.1: The figure is borrowed from [4]. Left: The antiferromagnetic structure on a bi-partite square lattice. Right: Illustration of geometrical frustration on a 2D triangular lattice with Ising spins.

frustration. It is essentially the competition between different bonds involving the same spin. Frustration yields degeneracies which are sometimes extensive in the system's size in the low-energy manifold such that it becomes tricky to pick a ground state for the system. The simplest example of frustration due to geometrical configuration can be illustrated on a triangle [Figure 1.1(right)]. Magnetic frustration has motivated numerous studies on disordered yet highly-entangled quantum states. This has contributed to making magnetism an excellent platform for investigations on many-body quantum physics. The work here focuses on systems forming long-range or incipient magnetic order at low temperature despite the frustration they may host and therefore will not elaborate too much on those subjects.

1.3 Magnon or spin wave - a prominent type of elementary magnetic excitations

What makes magnetism a fascinating platform is not just the presented collective magnetic ordering but also the nature of its excitations around these ordered states. There is a large family of different magnetic excitations. Similar to other fields in condensed matter physics, the concept of quasi-particles is crucial as those emergent collective excitations tend to behave like weakly-interacting particles in momentum space. Among all the quasi-particles in magnetism, magnons are arguably the most important ones because of their remarkable usefulness to describe many real observation for systems. Since it can be classically visualized as a propagating wave in an ordered spin array, it is also referred to as

spin wave. These two terms will be used interchangeably hence after.

There is more than one way to formulate spin-wave theory. At the classical level, one often starts from the Landau-Lifshitz-Gilbert equation of the motion of spin dynamics [5]. This picture is fairly accurate when dealing with macroscopic spins and is often applied in studies on micromagnets. For instance, the equation is used to model the effects of a magnetic field on ferromagnets. The equation of motion is nonlinear, but by linearizing the equation around some stable point in the phase space, magnons can be vividly understood as collective precession of the ordered spins.

For atomic spins which are of relevance here, the fact that spins are quantum mechanical objects becomes more important. Analogous to how quantum mechanics is formalized, one can derive spin-wave theory from the spin coherent-state path integral approach or the operator expansion approach [2]. The latter is better-defined in terms of truncation order and mathematically more tangible such that it appears to be more popular. In particular, the Holstein-Primakoff transformation [6] is widely used. It writes each individual spin operator $\mathbf{S}_i$ in its local quantization coordinates into,

$$S_i^+ = \sqrt{2S - a_i^\dagger a_i} a_i \approx \sqrt{2S}\left(1 - \frac{a_i^\dagger a_i}{4S}\right) a_i, \tag{1.3}$$

$$S_i^- = a_i^\dagger \sqrt{2S - a_i^\dagger a_i} \approx \sqrt{2S} a_i^\dagger \left(1 - \frac{a_i^\dagger a_i}{4S}\right), \tag{1.4}$$

$$S_i^z = S - a_i^\dagger a_i, \tag{1.5}$$

where S is the spin number and a_i is the Holstein-Primakoff boson. As indicated above, the transformation is often expanded in terms of $1/S$ and those terms with higher order than cubic are truncated. The justification for this truncation can be either a large spin number S or a low density $\left\langle a_i^\dagger a_i \right\rangle$. It is also not difficult to see from Equation (1.5) that, the excitation of one magnon corresponds to the quantum number S^z being reduced by 1.

With the above transformation, any arbitrary spin Hamiltonian can be rewritten with respect to the orders of the boson operators,

$$\mathcal{H} = \mathcal{H}^{(0)} + \mathcal{H}^{(1)} + \mathcal{H}^{(2)} + \mathcal{H}^{(3)} + \mathcal{H}^{(4)} + ... \tag{1.6}$$

The above form is so generic that it is applicable in any weak coupling expansion about free quasi-particles. What makes the Holstein-Primakoff transformation special, however, is that only with the correct magnetic order will it become a valid expansion, where $\mathcal{H}^{(1)}$ in Equation (1.6) vanishes and $\mathcal{H}^{(2)}$ satisfies the positive definiteness. This means the quantization z-axis has to be where the magnetic moment is aligned, which is why it is regarded as a semi-classical approach.

Ignoring everything but $\mathcal{H}^{(2)}$ leads to the so-called linear spin-wave theory (LSWT). It solves the quadratic Hamiltonian where magnons behave as free particles. The theory is supposed to work very well with large spin numbers because it is based on $1/S$ expansion. Moreover, remarkable success is often found in cases with low spin numbers.

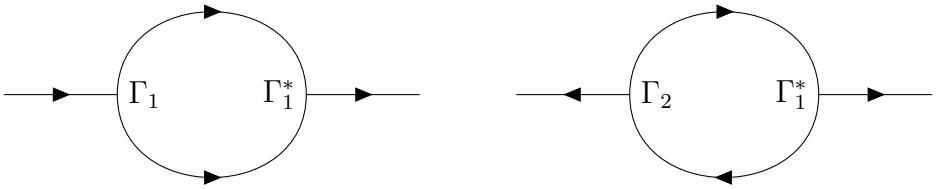

Figure 1.2: Examples of Feynman diagrams representing normal (left) and anomalous (right) magnon self-energies generated by cubic vertices Γ_i's.

As a low-order approximation, linear spin-wave theory is unable to capture all the subtle details of the excitation spectrum of magnetic insulators. In order to obtain more physical insights, one can taken into account some magnon-magnon interaction in a perturbative fashion. The cubic and quartic terms are often considered to account for the three-magnon or four-magnon scattering processes which let magnons acquire finite life time and potentially decay into multiple magnons [Figure 1.2]. This can often be used to explain the

renormalized magnon bandwidth and the reduction of its spectral weight. Such theoretical studies have been carried out for various systems [7, 8, 9]. There are also scenarios where this diagrammatic perturbation theory does not work well. One famous example is the $(\pi, 0)$ wave-vector anomaly observed in spin-1/2 square-lattice Heisenberg antiferromagnets [10, 11, 12, 13, 14]. While the picture of fractional excitation with unbounded spinons has been proposed, there also seems to be some success with a non-perturbative approach within the magnon framework [15].

The work reported in this thesis attempts to conduct a comprehensive examination of spin-wave theory in magnetic systems of which the effective spin Hamiltonian forms quasi-1D, quasi-2D or 3D lattices. This work points out the effectiveness as well as discrepancies encountered in a detailed manner. It involves innovation in the experimental techniques and analytical methods aiming for a better understanding of those specific systems. From a wider perspective, the work should also be considered as complimenting the effort to widen the scope of quantum magnetism and reveal the nature of fundamental spin excitations. Now that the theoretical framework has been covered, one may naturally ask what is the most powerful tool to study magnetic excitations in real materials. Therefore, it is worthwhile to walk through the unparalleled technique used to experimentally probe magnetic excitations - inelastic neutron scattering.

CHAPTER 2

NEUTRON SCATTERING

2.1 General theory of neutron scattering

Neutrons are massive particles identified by J. Chadwick [16] in 1932. It was soon discovered that the wavelength range of thermal neutrons is similar to the interatomic distances in solids. While neutrons are stable in atomic nuclei, they decay after a mean life time of 15 minutes during which they are free. With the advent of the world's first nuclear reactor that produced large quantities of free neutrons, neutrons started to become a valuable probe for condensed matter studies. As electrically neutral particles, neutrons can easily penetrate most materials while weakly interacting with them. As such, neutron scattering is primarily a probe of the bulk properties of solids. Moreover, neutrons possess an intrinsic magnetic moment that enables their interaction with the unpaired electrons of samples (magnetism). Since there are already many textbooks [17, 18, 19, 20, 21, 22] that give a detailed and rigorous theoretical treatment of the thermal neutron scattering process, this chapter will briefly present the formalism of the neutron scattering cross-section and provide the necessary context for understanding the later work.

A scattering process occurs when an incident neutron with a wave vector $\mathbf{k}_\mathrm{i}$ is scattered by a sample through an angle of 2θ into a final wave vector $\mathbf{k}_\mathrm{f}$. The momentum, spin and energy of the neutron can change during this process, while obeying the conservation laws,

$$\hbar\mathbf{k} = \hbar\mathbf{k}_\mathrm{i} - \hbar\mathbf{k}_\mathrm{f}, \tag{2.1}$$

$$E = E_\mathrm{i} - E_\mathrm{f},$$

$$\Delta S = \sigma_\mathrm{i} - \sigma_\mathrm{f},$$

where $\hbar\mathbf{k}$, E and ΔS are momentum, energy and spin transfer to the sample.

As thermal neutrons are non-relativistic particles, conservation of their energy can be expressed as

$$E = \frac{\hbar^2}{2m_\mathrm{n}} \left(k_\mathrm{i}^2 - k_\mathrm{f}^2\right), \tag{2.2}$$

where m_n is the mass of a neutron and $k_\mathrm{i,f} = |\mathbf{k}_\mathrm{i,f}|$. For an elastic scattering process, $E = 0$ and $k_\mathrm{i} = k_\mathrm{f}$. In the case of elastic scattering from crystalline matter, constructive interferences are observed following the Bragg's law,

$$n\lambda = 2d \sin\theta, \tag{2.3}$$

where d is the spacing between planes from which the neutron scatters, λ is the neutron wavelength and n is an integer describing the order of the reflection.

In order to quantify the scattering intensity, the partial differential scattering cross-section, $\mathrm{d}^2\sigma/\,\mathrm{d}\Omega\,\mathrm{d}E_\mathrm{f}$, is defined as the probability of some normalized flux of neutrons per second with the incident wave vector $\mathbf{k}_\mathrm{i}$ being scattered into the solid angle $\mathrm{d}\Omega$ perpendicular to the direction of the final wave vector $\mathbf{k}_\mathrm{f}$ with the final neutron energy falling into the range between E_f and $E_\mathrm{f} + \mathrm{d}E_\mathrm{f}$.

The cross-section can be separated into two parts, the coherent and incoherent ones,

$$\frac{\mathrm{d}^2\sigma}{\mathrm{d}\Omega\,\mathrm{d}E_\mathrm{f}} = \left.\frac{\mathrm{d}^2\sigma}{\mathrm{d}\Omega\,\mathrm{d}E_\mathrm{f}}\right|_\mathrm{coh} + \left.\frac{\mathrm{d}^2\sigma}{\mathrm{d}\Omega\,\mathrm{d}E_\mathrm{f}}\right|_\mathrm{inc}. \tag{2.4}$$

It is primarily the coherent part that is valuable as it provides information on the cooperative effects in solids while incoherent scattering reflects random isotropic and nuclear spin distributions in the target.

A more detailed derivation of the cross section comes from the Fermi's golden rule and

yields,

$$\left.\frac{\mathrm{d}^2\sigma}{\mathrm{d}\Omega\,\mathrm{d}E_\mathrm{f}}\right|_{\lambda_\mathrm{i},\sigma_\mathrm{i}\to\lambda_\mathrm{f},\sigma_\mathrm{f}} = \frac{k_\mathrm{f}}{k_\mathrm{i}}\left(\frac{m_\mathrm{n}}{2\pi\hbar^2}\right)^2 \left|\langle\lambda_\mathrm{f}\sigma_\mathrm{f}|\,V\left(\mathbf{k}\right)|\lambda_\mathrm{i}\sigma_\mathrm{i}\rangle\right|^2 \delta\left(E+E_\mathrm{i}-E_\mathrm{f}\right), \tag{2.5}$$

where the $V(\mathbf{k})$ is the Fourier transition of the effective interaction potential between neutrons and the sample,

$$V(\mathbf{k}) = \int V(\mathbf{r})e^{i\mathbf{kr}}\,\mathrm{d}\mathbf{r}, \tag{2.6}$$

with $\mathbf{r}$ being the position of the scattering centers. σ_i and σ_f are the initial and final spin polarizations of neutrons. A key step after this is to sum over all final states of the sample λ_f and final polarization states σ_f while taking an thermal average of the initial states, which leads to

$$\frac{\mathrm{d}^2\sigma}{\mathrm{d}\Omega\,\mathrm{d}E_\mathrm{f}} = \frac{k_\mathrm{f}}{k_\mathrm{i}}\left(\frac{m_\mathrm{n}}{2\pi\hbar^2}\right)^2 \sum_{\lambda_\mathrm{f},\sigma_\mathrm{f}}\sum_{\lambda_\mathrm{i},\sigma_\mathrm{i}} p_{\lambda_\mathrm{i}}p_{\sigma_\mathrm{i}}\left|\langle\lambda_\mathrm{f}\sigma_\mathrm{f}|\,V\left(\mathbf{k}\right)|\lambda_\mathrm{i}\sigma_\mathrm{i}\rangle\right|^2 \delta\left(E+E_\mathrm{i}-E_\mathrm{f}\right). \tag{2.7}$$

Note that one also uses $\mathbf{Q}$ quite often to denote the momentum transfer $\mathbf{k}$ here.

In general, when the neutron beam is unpolarized, the above equation reduces to

$$\frac{\mathrm{d}^2\sigma}{\mathrm{d}\Omega\,\mathrm{d}E_\mathrm{f}} = \frac{k_\mathrm{f}}{k_\mathrm{i}}S(\mathbf{k},E), \tag{2.8}$$

where the response function $S(\mathbf{k},E)$ is by definition

$$S(\mathbf{k},E) = \frac{1}{2\pi\hbar}\left(\frac{m_\mathrm{n}}{2\pi\hbar^2}\right)^2 \int_{-\infty}^{\infty}\langle V(\mathbf{k},0)V(-\mathbf{k},t)\rangle\, e^{-iEt/\hbar}\,\mathrm{d}t. \tag{2.9}$$

This is within the framework of linear response theory, which coheres with the fact that neutron scattering probes the bulk properties.

2.2 Magnetic neutron scattering

As neutrons interact with both nuclei and unpaired electrons in the material, the response function can be further separated into different pieces. The pertinent part to our work is the magnetic scattering for which a brief introduction will be presented here.

As mentioned, neutrons carry a intrinsic magnetic moment. Therefore, neutrons can sense the sample through the dipole-dipole interaction between the moment of neutron and the internal magnetic fields of the sample produced by spin and angular momentum of unpaired electrons. The neutron moment is,

$$\boldsymbol{\mu}_{\mathrm{n}} = -\gamma \mu_{\mathrm{N}} \boldsymbol{\sigma}, \tag{2.10}$$

where $\mu_{\mathrm{N}} = e\hbar/2m_{\mathrm{p}}$ is the nuclear magneton and $\gamma \approx 1.913$ is the gyromagnetic ratio. $\boldsymbol{\sigma}$ is the vector of Pauli spin operators. The potential felt by a dipole in an inhomogeneous field $\mathbf{B}$ from the sample is,

$$V_{\mathrm{M}}(\mathbf{r}) = -\boldsymbol{\mu}_{\mathrm{n}} \cdot \mathbf{B}(\mathbf{r}). \tag{2.11}$$

The field at a distance $\mathbf{R}$ from an electron with momentum $\mathbf{p}$ and magnetic moment $\boldsymbol{\mu}_{\mathrm{e}} = -2\mu_{\mathrm{B}}\mathbf{s}$ due to its spin angular momentum $\mathbf{s}$ is the sum of the magnetic field contributions from to the electrons's spin and orbital,

$$\mathbf{B} = \mathbf{B}_S + \mathbf{B}_L = \frac{\mu_0}{4\pi R^2}\left(\nabla \times \boldsymbol{\mu}_{\mathrm{e}} \times \hat{\mathbf{R}} - \frac{2\mu_{\mathrm{B}}}{\hbar}\mathbf{p} \times \hat{\mathbf{R}}\right). \tag{2.12}$$

The Fourier transform of such a potential is

$$V_{\mathrm{M}}(\mathbf{k}) = -\mu_0 \boldsymbol{\mu}_{\mathrm{n}} \cdot \mathbf{M}_{\perp}(\mathbf{k}), \tag{2.13}$$

where

$$\mathbf{M}_{\perp}(\mathbf{k}) = \hat{\mathbf{k}} \times \mathbf{M}(\mathbf{k}) \times \hat{\mathbf{k}} = -2\mu_{\mathrm{B}} \sum_{j} e^{i\mathbf{k}\mathbf{r}_j} \left(\hat{\mathbf{k}} \times \mathbf{s}_j \times \hat{\mathbf{k}} + \frac{i}{\hbar k} \mathbf{p}_j \times \hat{\mathbf{k}} \right), \tag{2.14}$$

is the component of the real-space magnetization perpendicular to $\mathbf{k}$. The index j sums over all the electrons. Again, with regard to unpolarized neutrons, it is rather straightforward to get

$$\frac{\mathrm{d}^2\sigma}{\mathrm{d}\Omega\, \mathrm{d}E_{\mathrm{f}}} = \frac{k_{\mathrm{f}}}{k_{\mathrm{i}}} \left(\frac{\gamma r_0}{2\mu_{\mathrm{B}}} \right)^2 \left[\left| \mathbf{M}_{\perp}(\mathbf{k}) \right|^2 \delta(E) + \tilde{S}(\mathbf{k}, E) \right], \tag{2.15}$$

where $r_0 \equiv \mu_0 e^2/(4\pi m_{\mathrm{e}})$ is the classical radius of the electron. And $\tilde{S}(\mathbf{k}, E)$ is the inelastic part,

$$\tilde{S}(\mathbf{k}, E) \propto \left| \mathcal{F}(\mathbf{k}) \right|^2 \sum_{\alpha\beta} \left(\delta_{\alpha\beta} - \hat{k}_{\alpha} \hat{k}_{\beta} \right) \int \left\langle S^{\alpha}\left(-\mathbf{k}, 0\right) S^{\beta}\left(\mathbf{k}, t\right) \right\rangle e^{-i\omega t} \mathrm{d}t, \tag{2.16}$$

with $\mathcal{F}(\mathbf{k})$ being the magnetic form factor. that corresponds to the Fourier transform of the local magnetic ion density from which the neutron is scattering Most importantly, the integral on the right side is the spin dynamical structure factor. This enables neutron scattering to directly measure the dynamical spin correlation as a function of energy and momentum transfer. Due to selection rules, neutrons can either alter the spin number by one or simply not flip it. Such a quantized spin flip can often well correspond with the excitation of one magnetic quantum or one magnon. This is why spin-wave theory can efficiently obtain the spin dynamical structure factor.

2.3 Instrumentation for neutron spectroscopy

There are many different types of neutron instruments each of which specializes in certain fields or problems. The majority of the work in this thesis involves two common types of neutron spectrometers, triple-axis and time-of-flight spectrometers. Therefore, this

section will introduce these two types.

2.3.1 Triple-axis spectrometer

The triple-axis spectrometer (TAS) is used with steady neutron sources that produce continuous neutron beams. It is capable of measuring very precisely the change of momentum and energy of neutrons that scatter from samples. Therefore, it is useful in looking at detailed excitations for which high resolution scans are required. TAS has a long history and has been used in understanding of condensed matter physics for decades. A typical configuration of the spectrometer is shown in Figure 2.1.

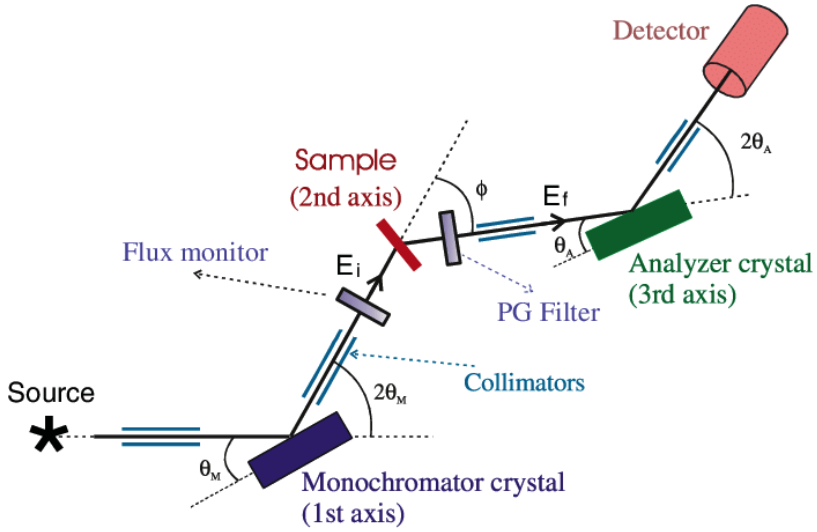

Figure 2.1: Schematic view of a triple-axis neutron scattering spectrometer. The figure is adapted from Ref. [23].

The wave vector $\mathbf{k}_\mathrm{i}$ of the incident neutrons is selected by Bragg reflections on a single-crystal monochromator from the polychromatic neutron beam generated by the source. By varying the scattering angle $2\theta_\mathrm{M}$, different wave vectors can be selected. The monochromator is usually made of materials such as pyrolytic graphite (PG), copper or other crystals. Very similar to the monochromator, the analyzer selectively reflects the scattered neutrons through the same mechanism and results in the outgoing neutrons with a final wave vector $\mathbf{k}_\mathrm{f}$.

The monitors are low-efficiency neutron detectors which typically rely on some nuclear reaction to generate detectable electric charges. ^{3}He is widely considered as the best element to detect neutrons. When a ^{3}He absorbs a neutron, it emits a proton and turns into ^{3}H. The ^{3}H nucleus eventually decays to form another ^{3}He such that the detector is in principle self sufficient. However, it is possible to saturate a detector with very high neutron flux because of the finite relaxation time.

Since there are two tunable parameters $\mathbf{k}_\mathrm{i}$ and $\mathbf{k}_\mathrm{f}$, there exists numerous ways to measure a given $(\mathbf{k}, E)$ point. They do not lead to the same intensity or resolution characteristics. In general, the final wave vector $\mathbf{k}_\mathrm{f}$ is fixed while the incident one $\mathbf{k}_\mathrm{i}$ is allowed to vary. This can often help maximize the incident neutron flux as well as avoid the necessary correction of the scattering intensity which is both $\mathbf{k}_\mathrm{f}$ and analyzer reflectivity dependent.

As one geometrical configuration can only measure one $(\mathbf{k}, E)$ point at a time, it can take a significant amount of time to measure a detailed spectrum. It also adds to the difficulty in finding the proper $\mathbf{k}$-E space. To alleviate this problem, a variant of TAS, which is the multi-axis spectrometer, has been developed. One example is the multi-axis crystal spectrometer (MACS) [24] at National Institute of Standard and Technology. Essentially, instead of having one neutron detector with one analyzer, it has a horizontal array of twenty detectors each with an analyzer. As a result, when E_f is fixed, multiple $\mathbf{k}_\mathrm{f}$'s can be captured. This has tremendously helped the data collection efficiency with the work in this thesis.

2.3.2 Time-of-flight spectrometer

The time-of-flight (TOF) spectrometer mostly operates on pulsed neutron sources. The pulsed beam can either be generated by a spallation neutron source that is intrinsically pulsed or a chopper system which cuts out pulses from a continuous neutron beam. A spallation source works by using accelerated protons to hit a heavy-metal target to produce fast neutrons.

The TOF measurements can have two settings of geometry. The direct geometry spectrometer has a well-defined incident neutron energy E_{i} from a crystal or a chopper while the final neutron energy E_{f} is found from time of flight. The indirect geometry spectrometer illuminates the sample with a polychromatic beam with E_{i} determined by time of flight and E_{f} is fixed by a crystal or filter. The direct geometry [Figure. 2.2] is more common and will be discussed further.

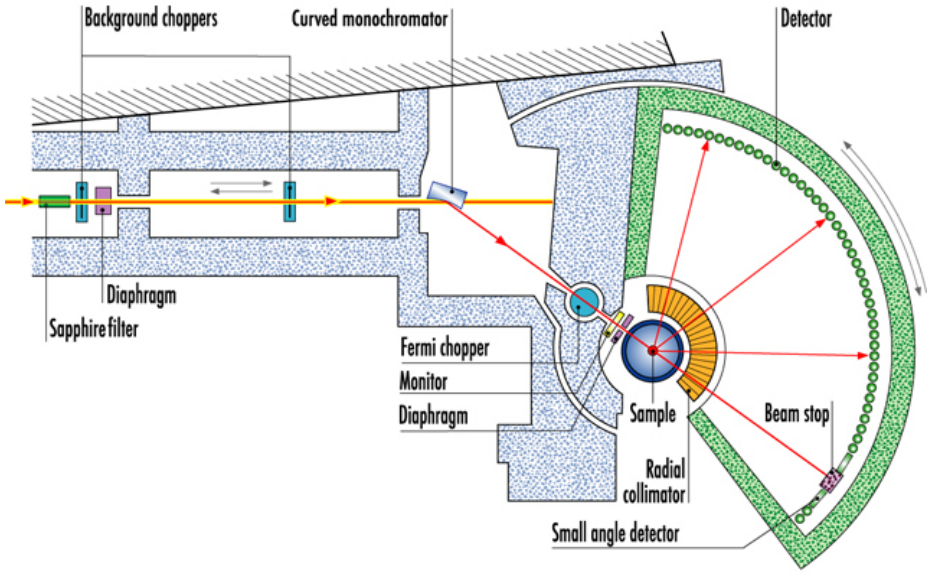

Figure 2.2: Schematic view of IN4C at ILL, an example for time-of-flight neutron scattering spectrometer.

Thermal neutrons can be treated as particles when encountering the slits on the choppers since the neutron wavelength is much smaller than the slits. The initial neutron beam from the source contains an ensemble of neutrons with velocities $\langle v \rangle \pm \delta v$. For a spallation source, fast neutrons produced in the instant of proton spallation will be blocked with a background chopper. A Fermi chopper, which is a rotating drum synchronized with the neutron pulse, is then used to define the incident neutron energy. As a result, only a narrow range of neutrons with the desired energy shall pass, while the remainder will be absorbed by the chopper made of highly absorbing material. The energy width can

be varied by adjusting the chopper frequency. The adjustment that benefits the energy resolution typically hurts the intensity [25].

The scattered beam from the sample will reach the detector banks. The precision of measured neutron position is within around 1 cm and that of the neutron arrival time is around 1 ns. When the chopper-sample and sample-detector distances are L_1 and L_2, respectively, the time interval for neutrons with certain E_i and E_f to travel the distance can be found by solving,

$$t_{12} = \left(\frac{m_\mathrm{n}}{2}\right)^{1/2} \left(\frac{L_1}{E_\mathrm{i}^{1/2}} + \frac{L_2}{E_\mathrm{f}^{1/2}}\right). \tag{2.17}$$

Consequently, the corresponding $(\mathbf{k}, E)$ can be calculated. Since it is a large detector bank that is capturing neutrons, it is much more efficient than a TAS to collect data in a wide $\mathbf{k}$-E space. When a single-crystal is being measured, it is also necessary to rotate the sample to capture the three-dimensional excitation spectrum. However, experiments can still face strong limitations from either the instrumental configuration or the lattice structure of the sample, which end up narrowing down the range of the measurement.

2.4 Keys to a successful neutron scattering experiment

As said, neutrons interact weakly with matters. It inevitably leads to rather weak scattering intensity compared with other techniques like X-ray spectroscopy. Inelastic neutron scattering, of which the scattering cross-section is typically several thousands of times smaller than elastic ones, especially struggles with this. Since the flux of the neutron beam cannot vary much without instrumental upgrades, a large quantity of sample in the beam is often crucial.

Meanwhile, single-crystal samples are always the most desirable form if one wants to get as much information as possible in the momentum space. Having a definite orientation also makes the interpretation more meaningful when an external magnetic field is applied.

Unfortunately, synthesis of big single crystals is and will always be a challenge in condensed matter physics. Many experiments are inevitably conducted with polycrystalline samples, including many of those in this thesis.

Lastly, effective cooling for the sample is also very important in order to probe the desired properties in the correct phase, especially when the sample quantity is large. As such, copper or aluminum is often used as sample holders or containers. And it is common to have helium as exchange gas inside sealed containers. The scattering process between the sample and neutrons does not produce much heat. Therefore, it is feasible and common to carry out neutron experiments at temperatures as low as $T = 30$ mK.

CHAPTER 3

REALIZATION OF DIAMOND-LATTICE ANTIFERROMAGNETS ON *A*-SITE SPINELS

3.1 Diamond lattice antiferromagnets

Three-dimensional systems are very suitable to study spin-wave excitations for which the formalism is based on symmetry breaking. Because of the Mermin-Wagner theorem [26], one-dimensional and two-dimensional systems with short-range interactions shall not spontaneously break any continuous symmetry at finite temperature. In fact, one-dimensional systems do not have any finite order parameter even at zero temperature.

Among all the possible 3D structures, the pyrochlore lattice has been drawing the most attention due to its inherent geometrical frustration. Typical examples are realized in rare-earth compounds [27, 28, 29, 30]. The diamond lattice, in contrast, has been less attractive for the exact same reason. However, since it is sufficiently simple and bi-partite, it is ideal to validate the spin-wave picture.

A common way to realize the diamond-lattice structure is through the *A*-site spinels. Recent studies have revealed some exotic physics on diamond-lattice Heisenberg antiferromagnets. Examples include the observation of some spin-liquid phase in the *A*-site spinel $MnSc_2S_4$ [31, 32], the spin-orbital entanglement in $FeSc_2S_4$ [33, 34, 35, 36, 37, 38] and the glassy magnetic behavior in $CoAl_2O_4$ [39, 40, 41, 42].

The work that is going to be presented here does not aim for the novelty claimed in the above examples. Among the big family of spinels, comprehensive investigations are carried out on the largely overlooked rhodites, ARh_2O_4 (A = Cu, Co) with the hope to carefully examine and validate the spin-wave theory applied to 3D systems.

The samples used for the research in this chapter were grown by Joshua Flynn at Oregon

State University [43].

3.2 $CoRh_2O_4$ - a canonical spin-$\frac{3}{2}$ antiferromagnet on a diamond lattice

3.2.1 Crystal structure

$CoRh_2O_4$ crystalizes in the cubic spinel structure [Figure 3.1] with space group $Fd\bar{3}m$. Occupying the tetrahedrally coordinated *A*-site, Co^{2+} ions form a perfect diamond-lattice. Nearest-neighbor magnetic exchange interactions between Co^{2+} ions are mediated by direct exchange or more likely by Co-O-Rh-O-Co super-exchange paths [44].

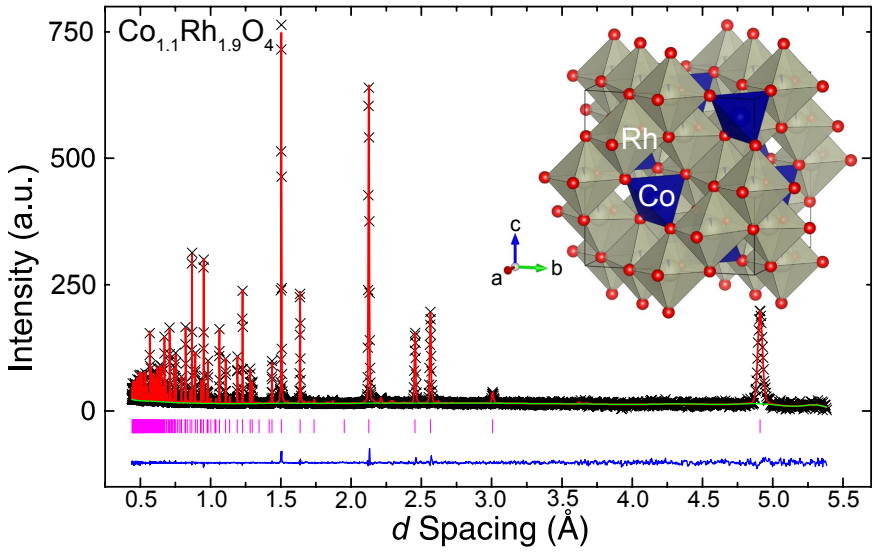

Figure 3.1: Room temperature time-of-flight neutron powder diffraction results for $CoRh_2O_4$. Rietveld refinement evidences a small degree of site mixing with $\%5.0(6)$ of Co on the B-site. The inset depicts the crystal structure with O represented as red spheres, Rh octahedra with gray faces and Co tetrahedra with blue faces.

3.2.2 Thermodynamic properties

Magnetic and thermodynamic measurements for $CoRh_2O_4$ are presented in Figure 3.2. A Curie-Weiss fit to the high-temperature regime of the inverse magnetic susceptibility [Figure 3.2(a)] yields a negative Weiss temperature $\Theta_W = -35.8(4)$ K and an effective moment $\mu_{\text{eff}} = 4.43(1)\ \mu_B$. In the undistorted tetrahedral crystal-field environment, Co^{2+}

adopts the $e_g^4 t_{2g}^3$ electronic configuration with one unpaired electron in each d_{xy}, d_{xz} and d_{yz} orbitals [45]. For such $S = 3/2$ magnetic moments, the experimental value of μ_{eff} yields a gyro-magnetic ratio $g \approx 2.18$. At low temperature regime, both magnetic susceptibility [Figure 3.2(a)-inset] and heat capacity [Figure 3.2(b)] show a transition at $T_{\text{N}} \approx 25$ K, indicating a long-range antiferromagnetic ordering. The magnetic contribution to the specific heat can be obtained by removing the phonon part from a Debye fit. From the lowest temperature it follows the $C_p = \alpha T^3$ behavior, as expected for gapless antiferromagnetic magnons, until a feature around $T^* = 12$ K shows up. Overall, the low frustration ratio [46] $f = |\Theta_{\text{W}}| / T_{\text{N}} = 1.4$ suggests $CoRh_2O_4$ behave as a canonical antiferromagnet with an average exchange interaction between nearest-neighbor magnetic moments ($z = 4$), $J_{\text{avg}} = 3k_{\text{B}}\Theta_{\text{W}}/zS(S+1) = 0.62$ meV.

3.2.3 Neutron diffraction and magnetic structure determination

To determine the magnetic structure of $CoRh_2O_4$ below the transition temperature, neutron powder diffraction was carried out on HB-2A at ORNL's High Flux Isotope Reactor. Results are presented in Figure 3.3. Symmetry analysis along with the Rietveld refinement on the observed magnetic Bragg peaks confirms that the compound orders in a simple two-sublattice antiferromagnetic structure [Figure 3.4(b)] at $T_{\text{N}} \approx 25$ K and places an upper bound of 5% on any reduction of the ordered moment due to quantum fluctuations at $T = 4$ K.

3.2.4 Inelastic neutron scattering and linear spin-wave calculation

As expected from all the aforementioned experimental results, the inelastic neutron scattering measurements on SEQUOIA at ORNL's Spallation Neutron Source reveal a simple magnetic excitation spectrum associated with non-interacting magnons [Figure3.5(a)]. The magnetic spectrum appears gapless within the resolution of instrumental configuration, with characteristic acoustic spin-wave branches emerging from the strong magnetic

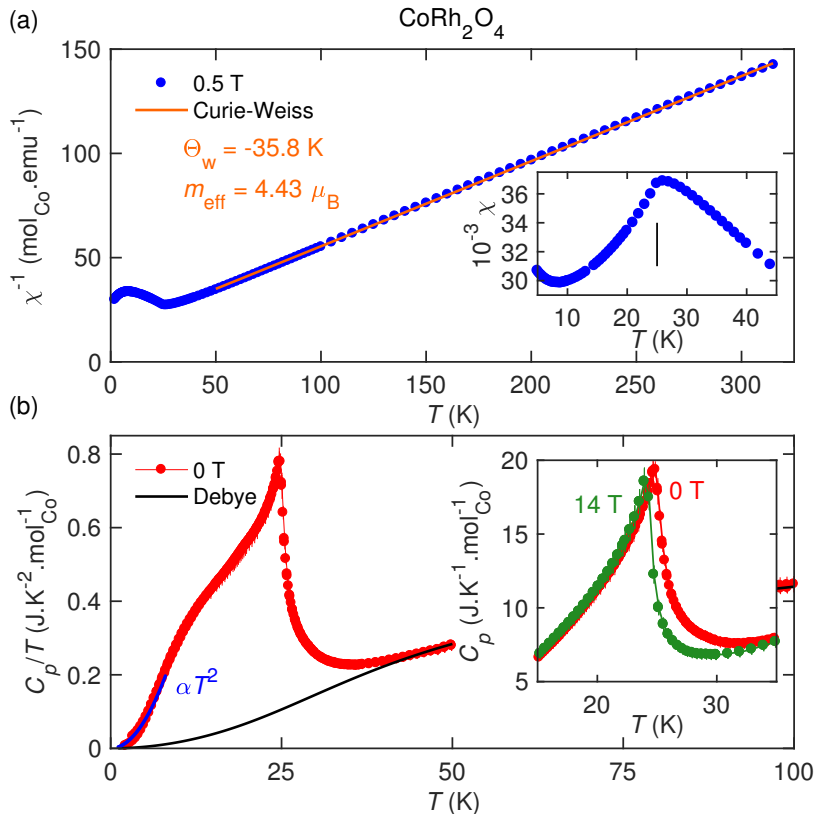

Figure 3.2: Magnetic and thermodynamic measurements for $CoRh_2O_4$. (a) Inverse magnetic susceptibility $\chi(T)^{-1}$ (blue circles) with a Curie-Weiss fit (orange line). Temperature dependence of the magnetic susceptibility $\chi(T)$ is plotted as inset with a turning point (black vertical line) associated with the Néel ordering transition. (b) Total specific heat over temperature C_p/T in zero magnetic field (red circles) and the Debye fit (black line). Field dependence is shown in inset.

Bragg peak positions. Using linear spin-wave theory with the help of the program SpinW [47], one can obtain an excellent agreement between the data and the simulated spectrum [Figure 3.5(b)] with a single nearest neighbor exchange parameter $J_1 = 0.63$ meV [Figure 3.4(a)]. This value matches very well with the average exchange interaction strength extracted from the magnetic susceptibility $J_{\text{avg}} = 0.62$ meV, indicating the further neighbor exchanges are negligible.

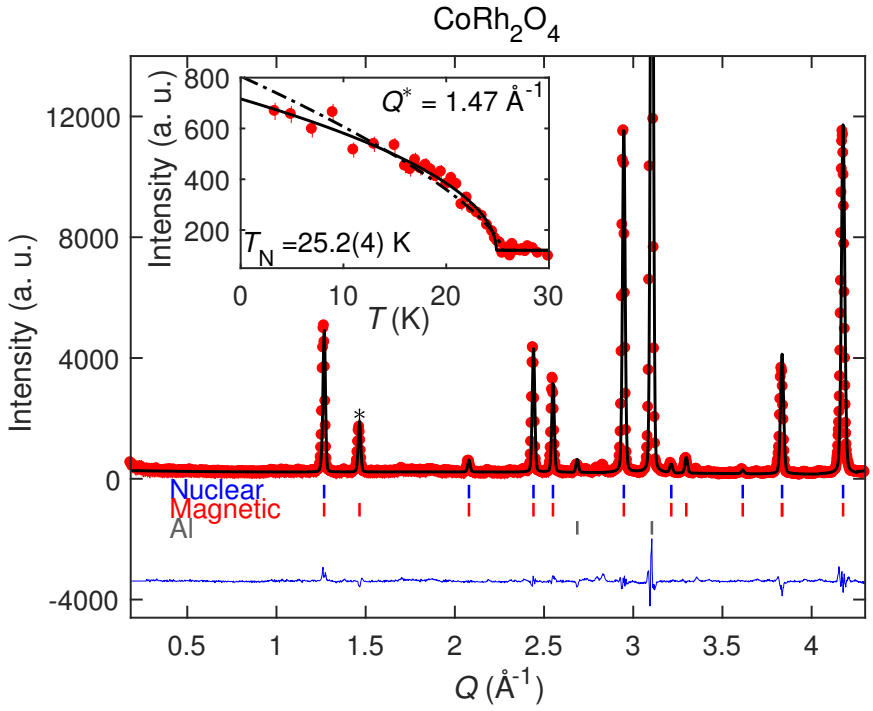

Figure 3.3: Neutron powder diffraction pattern of $CoRh_2O_4$ measured at $T = 4$ K with a neutron wavelength of $\lambda = 2.41$ Å(red dots), and corresponding Rietveld refinements (black line) of the nuclear (blue ticks), magnetic (red ticks) and aluminum background (gray ticks) contributions. The inset shows the temperature dependence of the most intense magnetic peak (highlighted with an asterisk). Black curves are order parameter fits to estimate the value of T_N.

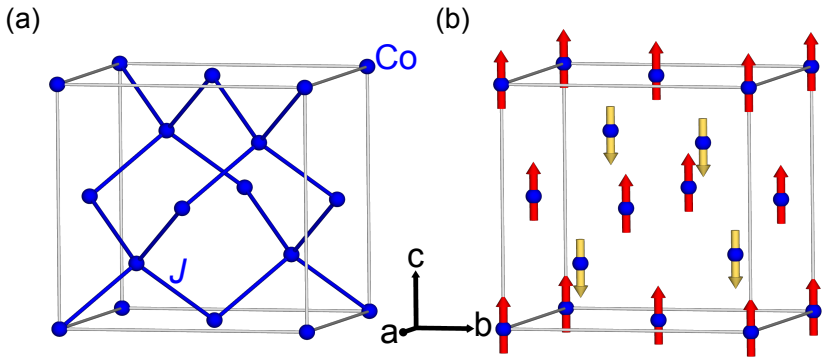

Figure 3.4: Conventional body-centerd unit cell for Co atoms (blue spheres) in $CoRh_2O_4$ showing (a) the diamond-lattice connectivity of the nearest neighbor bonds (blue lines) and (b) the two sublattice antiferromagnetic structure (red and yellow arrows).

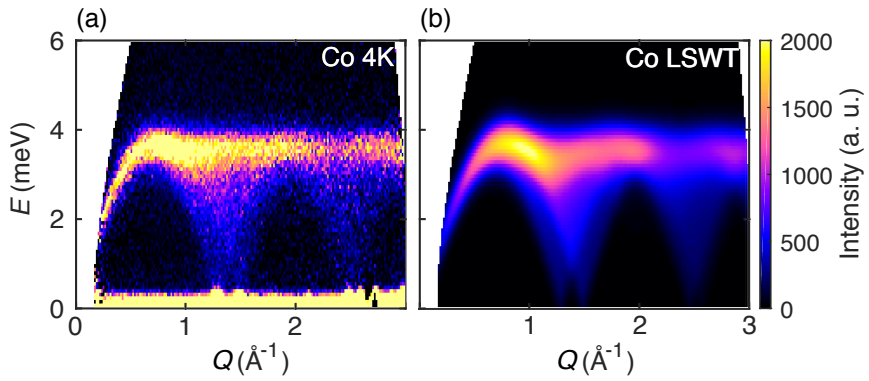

Figure 3.5: Magnetic excitations of $CoRh_2O_4$. (a) Momentum and energy dependence of the powder inelastic neutron scattering intensity $I(Q, E)$ at $T = 4$ K. (b) Linear spin-wave theory simulation of $I(Q, E)$, for the magnetic structure of Figure 3.4 with a nearest-neighbor exchange $J_1 = 0.63$ meV.

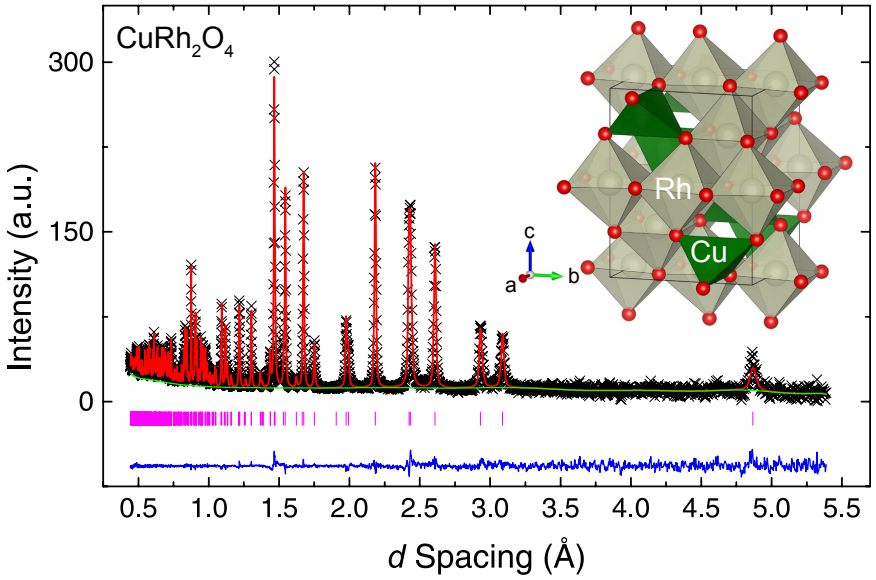

Figure 3.6: Room temperature time-of-flight neutron powder diffraction results for $CuRh_2O_4$. The inset depicts the crystal structure with O represented as red spheres, Rh octahedra with gray faces and Cu tetrahedra with green faces.

3.3 $CuRh_2O_4$ - the Jahn-Teller distorted variant

3.3.1 Crystal structure

Unlike $CoRh_2O_4$, $CuRh_2O_4$ crystallizes in a lower-symmetry structure due to the Jahn-Teller distortion around $T_{JT} \approx 850$ K. As a result, it has been described as a tetragonally

distorted spinel. The room temperature neutron diffraction results, as shown in Figure 3.6, yield $I4_1/amd$ as the appropriate room-temperature space group. Overall, the tetragonal distortion leads to four nearest neighbor Cu-Cu distances within 0.2% of each other such that all Cu^{2+} ions effectively remain organized on a diamond lattice at an average distance of $3.61(5)$ Å. However, next-nearest-neighbor Cu-Cu distances are split into four short and eight long links. The profound consequences shall be seen for the magnetic properties of $CuRh_2O_4$.

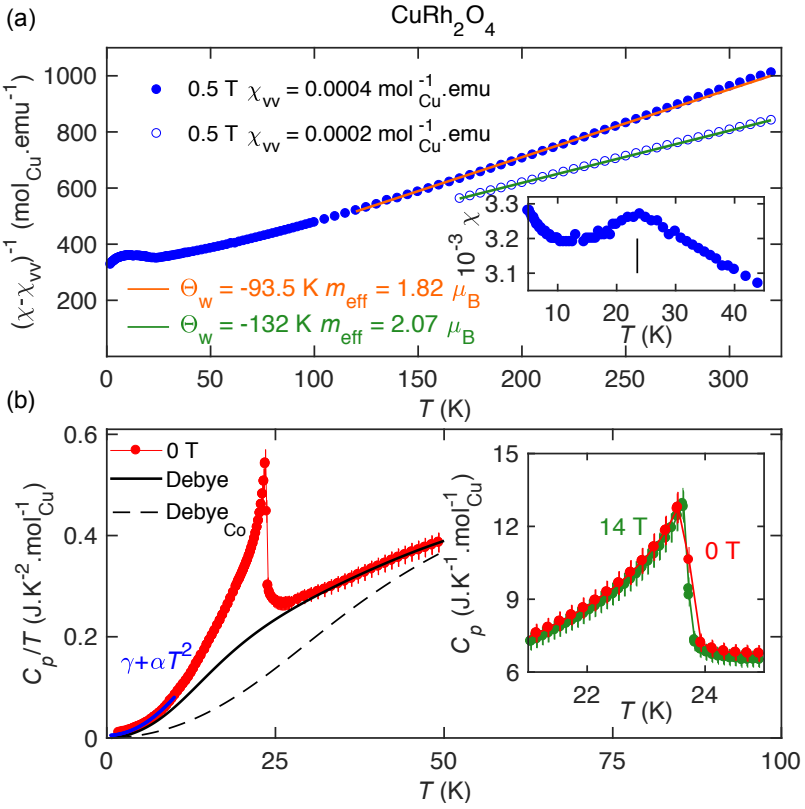

Figure 3.7: Magnetic and thermodynamic measurements for $CuRh_2O_4$. (a) Inverse magnetic susceptibility $\chi(T)^{-1}$ (blue circles) with a Curie-Weiss fit (orange line). Temperature dependence of the magnetic susceptibility $\chi(T)$ is plotted as inset with a turning point (black vertical line) associated with the Néel ordering transition. (b) Total specific heat over temperature C_p/T in zero magnetic field (red circles) and the Debye fit (black line). Field dependence is shown in inset.

3.3.2 Thermodynamic properties

Magnetic and thermodynamic measurements for $CuRh_2O_4$, as presented in Figure 3.7, resemble those for $CoRh_2O_4$. Both magnetic susceptibility and specific heat data indicate a magnetic phase transition around $T_N = 23.5$ K. The possible Van-Vleck contribution χ_{VV} leads to an ambiguity in determining the Curie-Weiss constant Θ_W and effective moment μ_{eff}. However, the magnitude of Θ_W ($\sim$ 100 K) implies stronger magnetic frustration in this system.

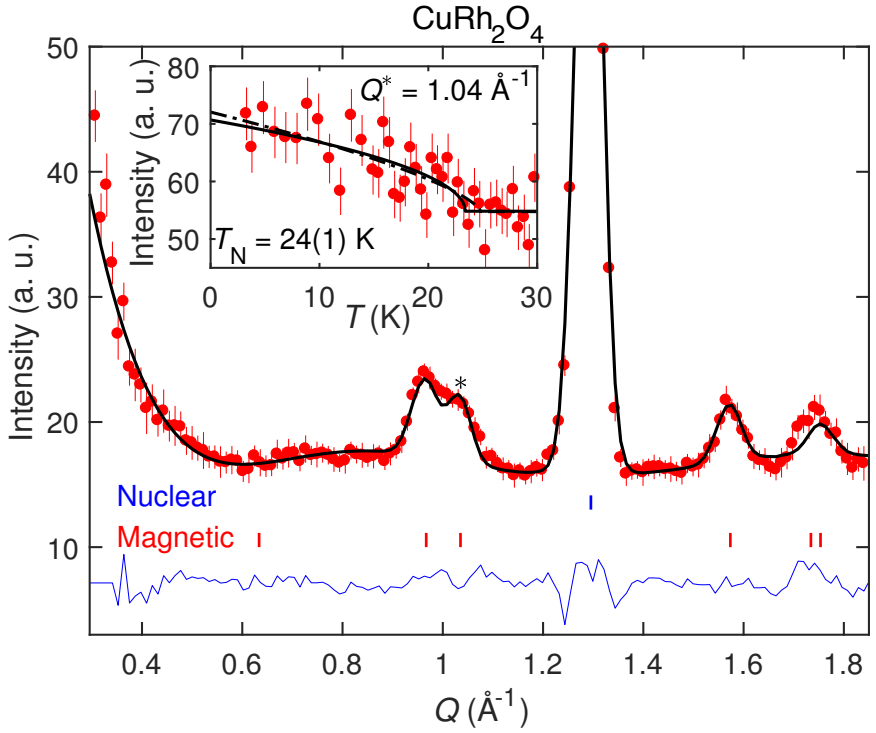

Figure 3.8: Rietveld refinement on $CuRh_2O_4$ elastic scattering results measured at $T = 4$ K, extracted from an energy-integrated elastic cut through the inelastic data. The inset shows the temperature dependence of the most intense magnetic peak (highlighted with an asterisk) from neutron diffraction. Black curves are order parameter fits to estimate the value of T_N.

3.3.3 Neutron diffraction and magnetic structure determination

Low-temperature neutron diffraction provides more evidence for the presence of frustration. New Bragg peaks were observed after the sample of $CuRh_2O_4$ was cooled down

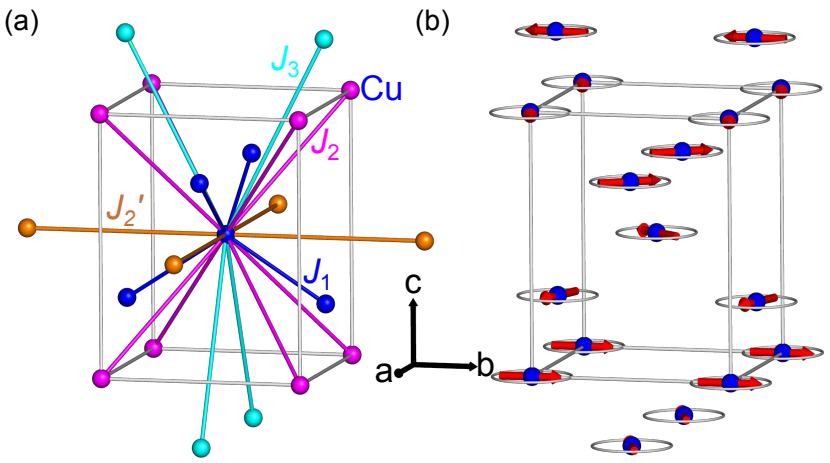

Figure 3.9: Conventional body-centerd unit cell for Cu atoms (blue spheres) in $CuRh_2O_4$ showing (a) the connectivity of up to third-neighbor bonds and (b) incommensurate magnetic structure with $\mathbf{k}_\mathrm{m} = (0, 0, 0.79)$.

from 25 K to 4 K [Figure 3.8], which were identified as magnetic peaks emerging with the long-range magnetic order. The temperature dependence of the integrated intensity of one selected peak [Figure 3.8-inset] yields $T_\mathrm{N} = 24(1)$ K.

Those magnetic Bragg peaks are able to be indexed using an incommensurate magnetic propagation vector $\mathbf{k}_\mathrm{m} = (0, 0, 0.79)$. Symmetry group analysis of reveals the magnetic structure of $CuRh_2O_4$ as a circular helix, shown in Figure 3.9(b), which probably originates from competing exchange interactions. The subsequent Rietveld refinement further confirms the magnetic wave vector $\mathbf{k}_\mathrm{m}$ and also a strongly reduced ordered moment $\mu_\mathrm{ord} = 0.56(6)\mu_\mathrm{B}$ from its maximum expected value $1.05\mu_\mathrm{B}$. This is related to quantum fluctuations, which will be further discussed via spin-wave theory later.

3.3.4 Inelastic neutron scattering and linear spin-wave calculation

Like what was observed from $CoRh_2O_4$, the magnetic excitation of $CuRh_2O_4$ from inelastic neutron scattering is also gapless within the instrumental resolution. However the features [Figure 3.10(a)] are much more complex in this case, which is anticipated from the more frustrated nature of the system.

This calls for a look at further neighbor interactions, which gives a large parameter space. Therefore, it is useful to apply mean-field theory to narrow down the microscopic Hamiltonian from the known magnetic structure. Its starting point is a Heisenberg model with up to third-nearest neighbor interactions. The mean-field theory follows the steps of Bertaut [48] and Chapon [49].

Calculations are performed in a primitive unit cell, which is less symmetric than the conventional cell but contains the smallest possible number of atoms and thus more concise and efficient. The Heisenberg model is of the following form,

$$\mathcal{H} = \frac{1}{2} \sum_{i,j,m,n} J_{ij}(\mathbf{R}_n - \mathbf{R}_m)\, \mathbf{S}_i(\mathbf{R}_m) \cdot \mathbf{S}_j(\mathbf{R}_n), \tag{3.1}$$

where $\mathbf{S}_i(\mathbf{R}_m)$ denotes the i-th spin of a primitive unit cell located at a lattice vector $\mathbf{R}_m$ from the origin, and $J_{ij}(\mathbf{R}_n - \mathbf{R}_m) \equiv J_d$ is the exchange interaction between spins $\mathbf{S}_i(\mathbf{R}_m)$ and $\mathbf{S}_j(\mathbf{R}_n)$. The selected exchange interactions J_1, J_2, J_2' and J_3 shown in Figure 3.9(a) are considered while possible exchange anisotropies are neglected.

Now one can take the Fourier transform of the exchange interactions,

$$J_{ij}(\mathbf{q}) = \sum_n J_{ij}(\mathbf{R}_n) e^{-\mathrm{i}\mathbf{q}\cdot\mathbf{R}_n}, \tag{3.2}$$

where $i \in \{1, 2\}$ labels the two Cu ions in the primitive unit cell. $J_{ij}(\mathbf{q})$ describes a 2×2 Hermitian matrix for each momentum $\mathbf{q}$ in the first Brillouin zone,

$$J(\mathbf{q}) = -\begin{pmatrix} J_{11} & J_{12} \\ J_{12}^* & J_{11} \end{pmatrix}, \tag{3.3}$$

where $J_{ij}^*(\mathbf{q}) = J_{ij}(-\mathbf{q})$. The matrix elements are evaluated by identifying the lattice translation vectors that connect pairs of spins dressed by a given interaction. Converting

from primitive to conventional indices, one obtains

$$\begin{aligned} J_{11}(\mathbf{q}) &= 2J_2\{\cos[\pi(h+k+l)] + \cos[\pi(h+k-l)] \\ &\quad + \cos[\pi(k+l-h)] + \cos[\pi(h+l-k)]\} \\ &+ 2J_2'[\cos(2\pi h) + \cos(2\pi k)], \end{aligned} \tag{3.4}$$

$$\begin{aligned} J_{12}(\mathbf{q}) &= J_1\{1 + e^{2\pi ik} + e^{\pi i(h+k+l)} + e^{\pi i(-h+k+l)}\} \\ &+ J_3\{e^{-\pi i(h-k+l)} + e^{\pi i(h+k-l)} + e^{2\pi il} + e^{2\pi i(k+l)}\}, \end{aligned} \tag{3.5}$$

where (h, k, l) are expressed in reciprocal lattice units of the conventional unit cell.

The interaction matrix has two eigenvalues at each wave vector $\mathbf{q}$, given by

$$\lambda_{\pm}(\mathbf{q}) = J_{11}(\mathbf{q}) \pm |J_{12}(\mathbf{q})|. \tag{3.6}$$

The wave vector $\mathbf{k}$ for which $\max[\lambda_{\pm}(\mathbf{k})]$ reaches a global maximum in the first Brillouin zone is associated with the propagation vector $\mathbf{k}_{\mathrm{m}}$ of the ordered magnetic state. Usually only a small number of $\mathbf{k}$ points related by symmetry fulfill this condition. Highly-frustrated systems are exceptions for which $\max[\lambda(\mathbf{q})]$ can be degenerate over large regions of the Brillouin zone [50]. The classical ground-state energy in our particular system can be minimized with analytical solution, which is consistent with the mean-field method above and can speed up the computation.

The mean-field phase diagram as a function of J_2/J_1 and J_2'/J_1 for different values of J_3 is shown in Figure 3.11. In addition to the Néel phase, it consists of three different incommensurate phases for which the magnetic propagation vectors take the form $\mathbf{k}_{\mathrm{m},1} = (\xi, \xi, 0)$, $\mathbf{k}_{\mathrm{m},2} = (\xi, 0, 0)$ (which is equivalent to $(0, \xi, 0)$) or $\mathbf{k}_{\mathrm{m},3} = (0, 0, \xi)$. $CuRh_2O_4$ falls into the last phase, which helps constrain J_3/J_1 to J_2/J_1 and significantly reduces the parameter space.

With one degree of freedom eliminated, a set of J_i's that yields a good agreement

$J_1 = 10.1$ meV	$J_2 = 0.32\ J_1$
$J_3 = 0.098\ J_1$	$J_2' = 0.18\ J_1$

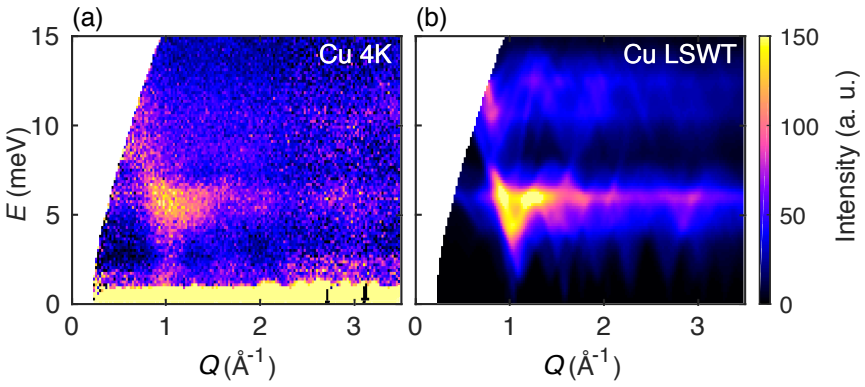

Figure 3.10: (Color online) Magnetic excitations of $CuRh_2O_4$. (a) Momentum and energy dependence of the powder inelastic neutron scattering intensity $I(Q, E)$ at $T = 4$ K. (b) Linear spin-wave theory simulation of $I(Q, E)$, for the magnetic structure of Figure 3.9(b), stabilized by the magnetic exchange interactions listed above the plot and defined in Figure 3.9(a).

between the neutron data and the spin-wave spectrum [Figure 3.10] was successfully found.

3.3.5 Ordered moment reduction

In addition to the spin-wave excitation spectrum, it is worthwhile to understand the strong moment reduction in $CuRh_2O_4$ by evaluating the strength of quantum effects in the obtained Hamiltonian. This is achieved by calculating the $1/S$ zero-point reduction on the ordered moment within the spin-wave framework.

In general, the spin reduction ΔS_i is sub-lattice dependent and reads

$$\Delta S_i \equiv S - \left\langle S^z_{i,\mathbf{R}_n} \right\rangle = \left\langle a^\dagger_{i,\mathbf{R}_n} a_{i,\mathbf{R}_n} \right\rangle = \frac{1}{\mathcal{N}} \sum_{\mathbf{k}\in \mathrm{B.Z.}} \left\langle a^\dagger_{i,\mathbf{q}} a_{i,\mathbf{q}} \right\rangle , \tag{3.7}$$

where $\langle \cdots \rangle$ is the thermal average and $\mathcal{N}$ is the number of unit cells in the entire system. The approach to evaluate ΔS_i uses the transformation from a-bosons into b-bosons,

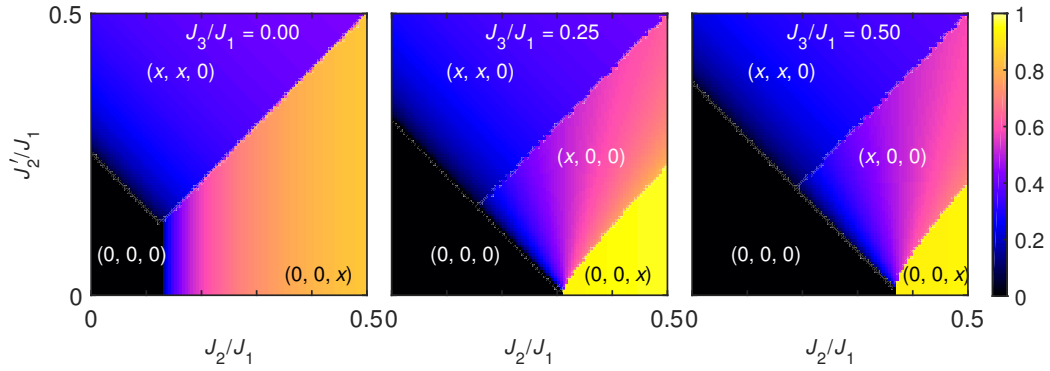

Figure 3.11: Mean-field phase diagram for the $CuRh_2O_4$ Hamiltonian with different J_2/J_1, J_2'/J_1 and J_3/J_1. The color represents the free components of the magnetic propagation vector in the different phases we uncover.

denoted as matrix $V_{\mathbf{q}}$. As a result,

$$\begin{aligned}\left\langle a_{i,\mathbf{q}}^{\dagger} a_{i,\mathbf{q}} \right\rangle = &\sum_{j=1}^{2} V_{j+2,i}^{\dagger} V_{i,j+2} \\ &+ \left[V_{ji}^{\dagger} V_{ij} + V_{j+2,i}^{\dagger} V_{i,j+2} \right] \left\langle b_{j,\mathbf{q}}^{\dagger} b_{j,\mathbf{q}} \right\rangle ,\end{aligned} \tag{3.8}$$

where boson commutation relations are applied. As $\left\langle b_{i,\mathbf{q}}^{\dagger} b_{i,\mathbf{q}} \right\rangle$ vanishes in the limit $T = 0$, this yields the general formula for the zero-point spin reduction

$$\begin{aligned}\Delta S_i &= \frac{1}{\mathcal{N}} \sum_{\mathbf{q}\in \mathrm{B.Z.}} \sum_{j=1}^{2} V_{j+2,i}^{\dagger} V_{i,j+2} \\ &= \int_{\mathbf{q}\in \mathrm{B.Z.}} \mathrm{d}^3\mathbf{q} \sum_{j=1}^{2} V_{j+2,i}^{\dagger} V_{i,j+2} \; (\mathcal{N} \to \infty).\end{aligned} \tag{3.9}$$

The numerical calculation of Equation 3.9 was implemented in C++ with the help of the adaptive multidimensional integration algorithm [51, 52]. Estimated integration errors are generally under 0.5% except for some of critical values of J's, for instance, $J_2 = J_2'$, for which integration errors are slightly larger.

Figure 3.12 was obtained by scanning through a certain slice of the exchange parameter space. Setting J_2, J_2' and J_3 to zero yields the spin reduction value for the nearest-neighbor 3D diamond-lattice antiferromagnet, $\Delta S_{\diamondsuit} = 0.11973(1)$, relevant for $CoRh_2O_4$. It is worth

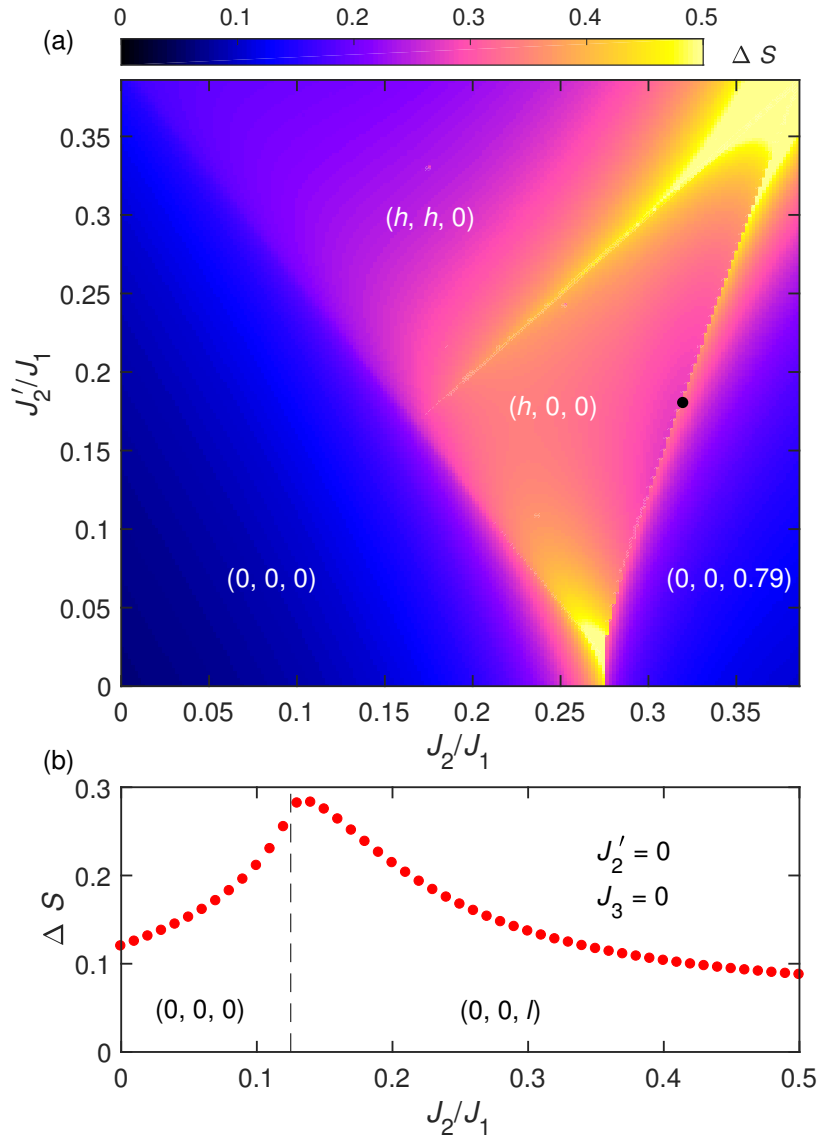

Figure 3.12: Zero-point spin reduction calculation for $CuRh_2O_4$. (a) ΔS as a function of J_2/J_1 and J_2'/J_1 with J_3 varying to maintain the propagation vector $\mathbf{k}_{\rm m} = (0, 0, 0.79)$ whenever possible. The black dot corresponds to the parameters for $CuRh_2O_4$. (b) ΔS as a function of J_2/J_1 with J_2' and J_3 fixed to zero. The vertical dashed line indicates the classical transition ratio from the Néel state to the incommensurate spiral state.

mentioning this number is significantly smaller than for the nearest-neighbor 2D square-lattice antiferromagnet, $\Delta S_{\square} = 0.19660$ [53]. For the exchange parameters of $CuRh_2O_4$, the spin-reduction is $\Delta S_{\rm Cu} = 0.330(1)$ which gives an ordered moment of $0.36\ \mu_{\rm B}$. This is in qualitative agreement with the experimental observation $\mu_{\rm ord} = 0.56(6)\ \mu_{\rm B}$.

3.4 Conclusions

In conclusion, $CoRh_2O_4$ is identified at a canonical nearest-neighbor Heisenberg antiferromagnet on the diamond lattice. It develops long range magnetic order below the Néel temperature $T_{\rm N} \approx 25$ K, while the magnetic excitation is successfully described by linear spin-wave theory.

In contrast, the tetragonally-distorted $S = 1/2$ spinel $CuRh_2O_4$ shows much richer magnetism led by the competing exchange interactions. While behaving similarly in thermodynamic measurements, the system forms an incommensurate spin helix with a propagation wave vector $\mathbf{k}_{\rm m} = (0, 0, 0.79)$ and indicates strong quantum reduction of the ordered magnetic moment.

Overall, both systems possess features of a typical 3D system which exhibits spontaneous symmetry breaking at some finite temperature. The resulting excitations are well contained in the linear spin-wave framework of which the validity is effectively demonstrated.

CHAPTER 4

ORIGIN OF INCOMMENSURATE SPIN CORRELATION IN THE FRUSTRATED FERROMAGNETIC SPIN-$\frac{1}{2}$ CHAIN

4.1 Spin chain systems

Spin chains are comparatively simple systems and thus very extensively studied from the theoretical point of views. This is mainly because both analytical and numerical methods tend to be more applicable on 1D systems. In particular, the density matrix renormalization group (DMRG) technique significantly reduces the effective Hilbert space while accurately capturing the ground state properties. As a result, remarkably rich physics can be explored and discussed on such systems.

The simplest yet non-trivial example is undoubtedly the spin-$1/2$ antiferromagnetic chain of which the exact ground state is solvable with Bethe Ansatz [54]. The elementary magnetic excitation of such a system is the fractional spin-$1/2$ quasi-particle called spinon. The excitations are detected from neutron scattering as a continuum of multi-spinon (dominantly two-spinon) excitations since the technique probes overall integer spin excitations. With concrete examples like $KCuF_3$ [55] and $CuSO_4{\cdot}5D_2O$ [56], this has achieved remarkable success. It is worth mentioning that the lower bound of the continuum which looks like an excitation band can somehow still be quantified as spin-waves with a band-width renormalization by $\pi/2$.

Diving further into the spin chain family, the J_1-J_2 frustrated spin chain system has been attracting much attention due to the rich physics it implies. A prototype of frustrated

spin chains has the following generic form of the Hamiltonian,

$$\mathcal{H} = \sum_i J_1 \mathbf{S}_i \cdot \mathbf{S}_{i+1} + J_2 \mathbf{S}_i \cdot \mathbf{S}_{i+2} - h S_i^z, \tag{4.1}$$

with J_1 being the nearest neighbor coupling and J_2 the next nearest neighbor coupling. h takes into account the external magnetic field when applicable.

The frustration here comes from the competition between J_1 and J_2. Theorists primarily focus on the cases where J_2 is antiferromagnetic ($J_2 > 0$) and J_1 can have either sign. In the case where J_1 is ferromagnetic, theoretical studies propose that the system may go through a vector chiral state to spin density-wave and/or spin nematic states with the increasing external field before reaching saturation [57]. None of these quantum states in principle has any finite order parameter. However, one may picture the vector chiral state using the classical incommensurate helical states. The spin nematic state is quite special in that it does break the continuous symmetry while retaining some discrete ones such as time-reversal symmetry [58].

It is non-trivial to discover such states experimentally due to the lack of a directly measurable order parameter. Most importantly, one needs to realize compounds that are confirmed to host such a spin Hamiltonian. This has motivated various studies on edge-sharing CuO_6 octahedra materials [59, 60], since the Cu^{2+} ion serves as a well-defined spin-half and the super-exchange mediated through Cu-O bonds can often lead to the desired form of ferromagnetic nearest-neighbors and antiferromagnetic next nearest neighbors. The study on $LiCuSbO_4$ which will be presented in this chapter is such a case. While the compound does not exhibit any long-range magnetic ordering down to the lowest temperature, it shall be shown here how spin-wave theory turns out to be surprisingly successful in revealing the nature of the system.

The sample used for the research in this chapter was grown by Sian Dutton at Princeton University.

4.2 $LiCuSbO_4$ - a distorted case with broken inversion symmetry

4.2.1 Crystal structure

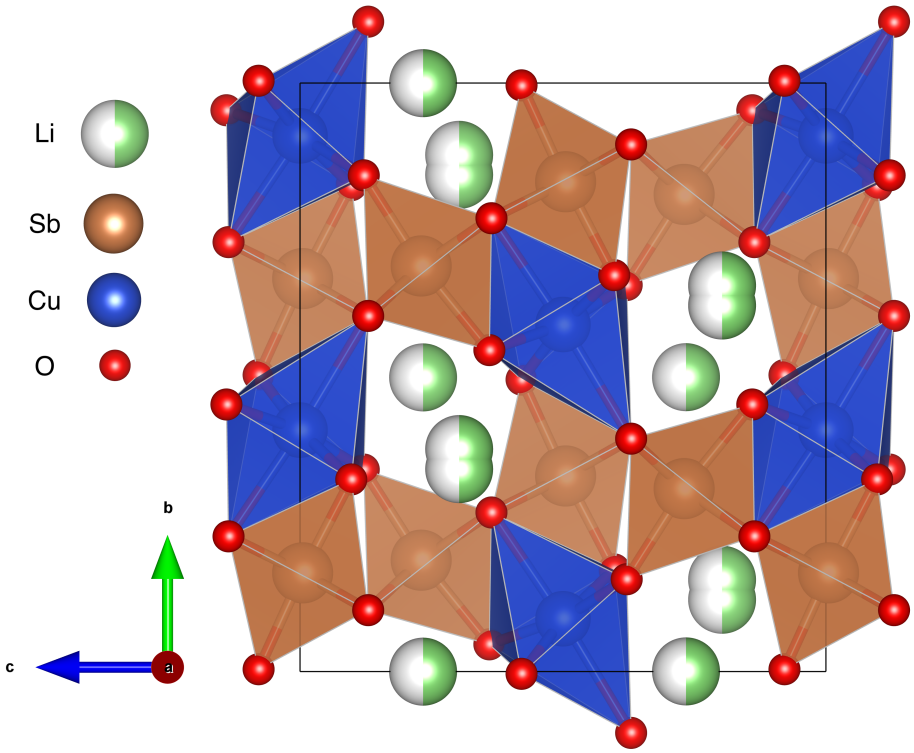

Figure 4.1: The crystal structure of $LiCuSbO_4$ viewed from the side.

$LiCuSbO_4$ is a quasi-1D spin-1/2 chain compound realized by edge sharing CuO_6 octahedra. Individual chains are well separated by Sb^{5+} ions, as shown in Figure 4.1. While the connectivity is quite similar as other frustrated ferromagnetic spin-1/2 chains [60], the Cu-O-Cu angles on two adjacent nearest bonds, as illustrated in Figure 4.2(a), are different due to Jahn Teller distortion [61]. Although the nearest-neighbor (NN) distance remains uniformly half the lattice constant a, the bond is split into two distinct ones and permits Dzyaloshinski-Moriya (DM) interactions by breaking the inversion symmetry about the bond center. More precisely, the space group $Cmc2_1$ allows any DM component onto the NN bonds perpendicular to the chains. Meanwhile, from the symmetry point of view, the next-nearest-neighbor (NNN) bond remains uniform but permits any kind of (anti-

)symmetric terms. Potential anisotropy will be neglected here since there is no experimental evidence implying it to be substantial.

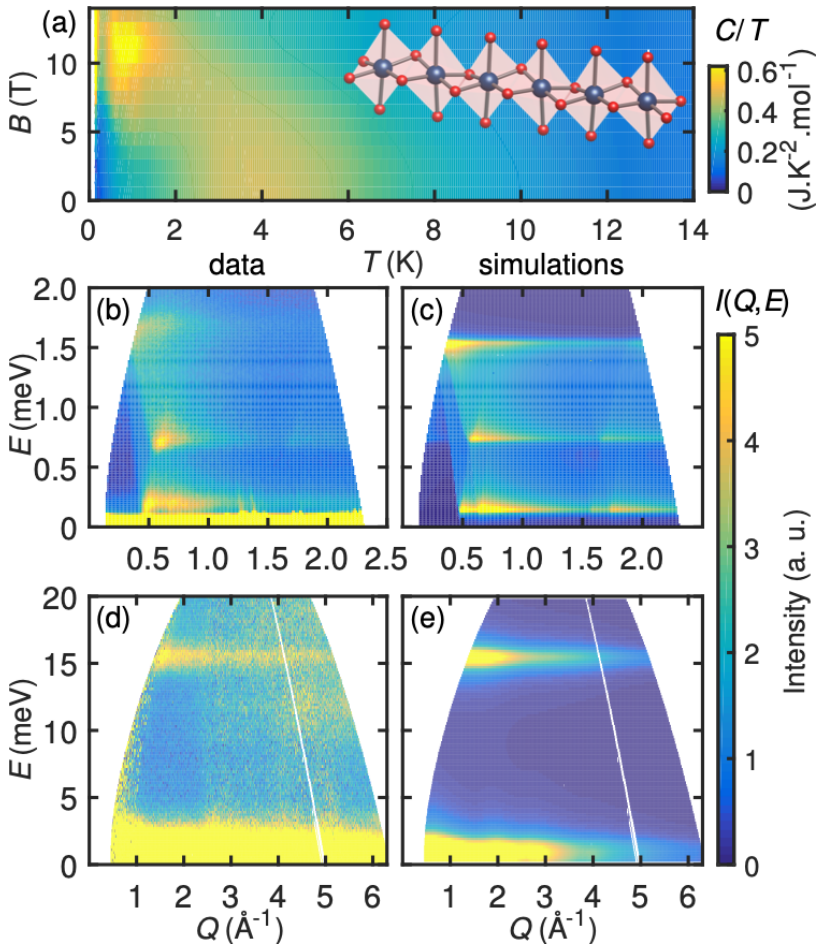

Figure 4.2: (a) The magnetic field dependent map of specific heat along with the visualization of an individual Cu chain illustrating four different Cu-O-Cu bond angles through the polyhedra. (b)-(e) Powder inelastic neutron data at the lowest available temperatures (left) and the fitted spin-wave spectra (right).

More details of the crystal structure can be found in Ref. [61]. The aforementioned

facts are sufficient here and yield the following minimal Hamiltonian

$$\begin{aligned}\mathcal{H} = \sum_n & J_1 \mathbf{S}_{n,1} \cdot \mathbf{S}_{n,2} + J_1' \mathbf{S}_{n,2} \cdot \mathbf{S}_{n+1,1} \\ & + \mathbf{D}_1 \cdot (\mathbf{S}_{n,1} \times \mathbf{S}_{n,2}) + \mathbf{D}_1' \cdot (\mathbf{S}_{n,1} \times \mathbf{S}_{n-1,2}) \\ & + \sum_{i=1,2} J_2 \mathbf{S}_{n,i} \cdot \mathbf{S}_{n+1,i},\end{aligned} \tag{4.2}$$

where J_1 and J_1' are the ferromagnetic NN exchanges, $\mathbf{D}_1$ and $\mathbf{D}_1'$ are the corresponding DM interactions, and J_2 is the antiferromagnetic NNN exchange. The index n is used to label the unit cells each containing two spins labeled by i.

4.2.2 Zero-field inelastic neutron scattering along with linear spin-wave calculation

Inelastic neutron scattering (INS) experiments were carried out on the IN5 disk chopper time-of-flight spectrometer at Institut Laue-Langevin (ILL), the cold neutron chopper spectrometer (CNCS) at Oak Ridge National Laboratory's (ORNL) Spallation Neutron Source (SNS) and the multi-axis crystal spectrometer (MACS) at National Institute of Standard and Technology (NIST). The same polycrystalline sample as in Ref. [61] was used. The zero-field measurement at low temperatures, $T \leq 2$ K, reveals magnetic excitations at two drastically different energy scales. Three modes are observed at the energy transfer $E < 2$ meV (Figure 4.2(b)) and one mode appears at $E \sim 15.5$ meV (Figure 4.2(d)). The lowest excitation is located at $E \sim 0.2$ meV that is possibly gapped (Figure 4.2(b)).

Modes in powder spectra often infer the extrema of single-crystal excitation branches. To better understand the excitation structure at low energy, it is useful to employ a conversion method which is peculiar to 1D systems [62, 63]. This method is based on a powder average scheme which will later be used for the relevant spin-wave calculation. Therefore, it is beneficial to demonstrate the derivation in details here.

To understand how this method works, one should recall the definition of the magnetic

neutron scattering cross-section,

$$\frac{\mathrm{d}^2\sigma}{\mathrm{d}\Omega\,\mathrm{d}\varepsilon} = \frac{k_\mathrm{f}}{k_\mathrm{i}}\left(\frac{\gamma r_0}{2}\right)^2 |\mathcal{F}(\mathbf{k})|^2 \sum_{\alpha\beta}\frac{g_\alpha}{2}\frac{g_\beta}{2}\left(\delta_{\alpha\beta}-\hat{k}_\alpha\hat{k}_\beta\right)\mathcal{S}^{\alpha\beta}(\mathbf{k},\omega). \tag{4.3}$$

For a purely 1D system, it is evident that $\mathcal{S}^{\alpha\beta}$ only depends on $\mathbf{k}\cdot\hat{x}_0$. The powder average of this part only would give

$$\begin{aligned}\tilde{\mathcal{S}}^{\alpha\beta}(k,\omega) =& \frac{1}{4\pi}\int \mathcal{S}^{\alpha\beta}(\mathbf{k},\omega)\,\mathrm{d}\Omega = \frac{1}{2}\int_0^{2\pi}\mathcal{S}^{\alpha\beta}(k\cos\theta,\omega)\sin\theta\,\mathrm{d}\theta \\ =& \frac{1}{2k}\int_{-k}^{k}\mathcal{S}^{\alpha\beta}(\zeta,\omega)\,\mathrm{d}\zeta = \frac{1}{k}\int_0^{k}\mathcal{S}^{\alpha\beta}(\zeta,\omega)\,\mathrm{d}\zeta,\end{aligned} \tag{4.4}$$

where x_0-axis is transformed to the polar $\tilde{z}$-axis for the spherical integration. Meanwhile, the fact that $\mathcal{S}^{\alpha\beta}$ possesses inversion symmetry in momentum space is used. One can see that this provides an efficient route to compute the powder average.

Now by reversing the integration, the above equation will give

$$\mathcal{S}^{\alpha\beta}_{\mathrm{sx}}(Q,\omega) = \left.\frac{\partial\left[\zeta\mathcal{S}^{\alpha\beta}_{\mathrm{pow}}(\zeta,\omega)\right]}{\partial\zeta}\right|_{\zeta=Q}, \tag{4.5}$$

where $\mathcal{S}^{\alpha\beta}_{\mathrm{sx}}$ ($\alpha = x, y, z$) is the single-crystal spin dynamical structure factor and $\mathcal{S}^{\alpha\beta}_{\mathrm{pow}}$ the powder average. Neglecting the polarization factor, the formula recovers the single-crystal neutron scattering cross section.

One must beware that neglect of the polarization factor is not rigorous step. Because the polarization factor $\delta_{\alpha\beta}-\hat{k}_\alpha\hat{k}_\beta$, which comes from the fact that neutrons can only probe the plane perpendicular to the local magnetic moment, makes the scattering cross section generally dependent on $\mathbf{k}$. The method naively assumes that this term is not influential to the qualitative features of the integration, which is often the case.

The numerical differentiation was done with the help of some wavelet transform [64]. The results are presented in Figure 4.3(b), where at least two branches are clearly observed

at $E < 2$ meV. The lowest excitation branch appears to emerge from $Q \sim 0.45$ Å^{-1} indicating an incommensurate wave vector $\mathbf{k}_{\mathrm{m}}$. Meanwhile, the second band minimum is centered around $\pi/a \sim 0.55$ Å^{-1}, which implies some commensurate antiferromagnetic nature inexplicable in a J_1-J_2-type spin chain. Note that this is the case where the spectrum recovery works remarkably well. And the success is largely attributed to the clean and high-quality data from the IN5 spectrometer, which has done an excellent job in low-angle background reduction.

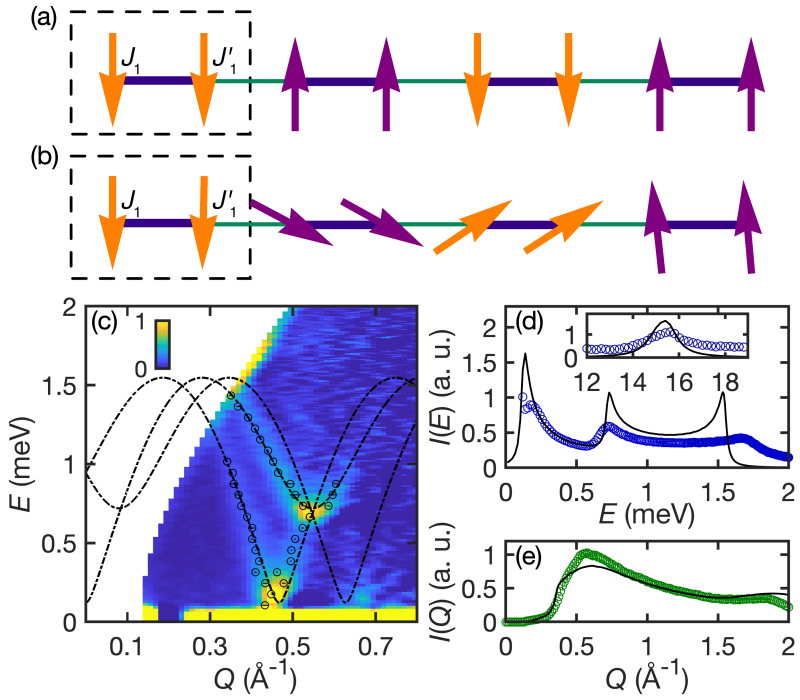

Figure 4.3: (a),(b) Schematic views by arrows of the up-up-down-down state and the modified structure with Dzyaloshinski-Moriya interaction. Dashed rectangles indicate a crystallographic unit cell along the chain direction. The thick dark blue line represents the J_1 bond and the thin green line represents the J'_1 bond. (c) Recovered single-crystal inelastic neutron spectrum (black circles are extracted branches) along with the fitted spin-wave dispersions (black dashed lines). (d),(e) Constant-energy (momentum transfer) cuts from the powder neutron data along with spin-wave calculation.

Although the compound exhibits no long-range magnetic ordering down to $T \sim 30$ mK [65], the distinct excitation branches from the recovered "single-crystal" spectrum signify some quasi-particle excitations which are likely magnon excitations from some quasi-long-

range magnetic ordering. Therefore, a comprehensive spin-wave investigation becomes worthwhile.

It is first necessary to sort out the possible classical ground states. Since the classical ground states for J_1-J_2 model are relatively well-known, it is convenient start from a J_1-J_1'-J_2 model without DM interactions. Apart from the trivial ferromagnetic state, such a system will in general form an incommensurate helical order with the wave vector denoted as $\mathbf{k}_{\mathrm{m}}$. To quantify the spin structure, θ is defined as the pitch angle between spins with same index in adjacent unit cells. And φ represents the angle between spins in the same unit cell. They are both uniquely determined by the specific Hamiltonian. For convenience, $\gamma \equiv \theta - \varphi$ is also defined here. As a result, the ground state energy can be obtained as the following,

$$E = S^2 \left[\frac{1}{2} \left(J_1 \cos\varphi + J_1' \cos\gamma \right) + J_2 \cos\theta \right], \tag{4.6}$$

Fortunately, there exists an analytical solution to minimize it,

$$\cos\theta = \left[\frac{(J_1 J_1')^2 - 4(J_2 J_1)^2 - 4(J_2 J_1')^2}{8 J_2^2 J_1 J_1'} \right], \tag{4.7}$$

$$\cos\varphi = \left[\frac{4(J_2 J_1')^2 - 4(J_2 J_1)^2 - (J_1 J_1')^2}{4 J_1^2 J_2 J_1'} \right]. \tag{4.8}$$

The ground states in terms of those two angles according to the above equations are presented in Figure 4.4. The boundary between different types of phases is quite distinct. As one can see, while the Lifshitz point from an incommensurate (IC) phase to the ferromagnetic state, similar to the J_1-J_2 model, exists at $J_2 = |J_1 + J_1'|/8$, a up-up-down-down (UUDD) state (Figure 4.3(a)) stabilizes with a sufficiently strong J_2 when $J_1 \neq J_1'$. Now it is time to introduce the DM interactions. To stabilize such co-planar ground state spin structures that preserve a $U(1)$ symmetry, DM interactions are set solely in some fictitious z_0 direction, *i.e.*, $\mathbf{D}_1 = D_z \hat{z}_0$ and $\mathbf{D}_1' = D_z' \hat{z}_0$. To respect the crystal symmetry group, z_0 just has to be along any direction within the bc-plane.

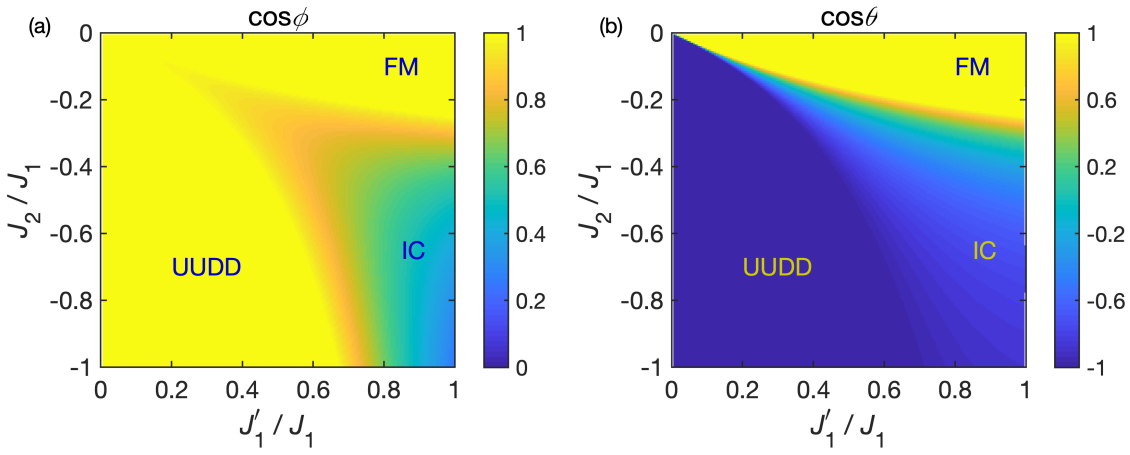

Figure 4.4: Color plots of pitch angle cosines, which indicate the classical ground states, as functions of J_2/J_1 and J_1'/J_1.

It is not difficult to verify the incommensurate ordering wave vector $\mathbf{k}_{\rm m} = k_{\rm m}\hat{x}_0$ is still valid in the presence of those uniaxial DM terms. But it will be easier for now to proceed with the spin-wave calculation and discuss the consequence of those terms along the way. To construct the spin-wave Hamiltonian, spin operators need to be quantized in their local reference frames where the z axes have to be where the spins are aligned. The consequential transformations are

$$\begin{aligned} S^{x_0}_{ni} =& S^{y}_{ni}\sin(\theta_n+\varphi_i) + S^{z}_{ni}\cos(\theta_n+\varphi_i), \\ S^{y_0}_{ni} =& -S^{y}_{ni}\cos(\theta_n+\varphi_i) + S^{z}_{ni}\sin(\theta_n+\varphi_i), \\ S^{z_0}_{ni} =& S^{x}_{ni}, \end{aligned} \tag{4.9}$$

where $\theta_n \equiv \mathbf{k}_{\rm m}\cdot\mathbf{R}_n$, $\theta_{n+1}-\theta_n \equiv \theta$ and φ_i is 0 or φ for $i = 1$ or 2 respectively.

The Hamiltonian can be separated into the odd and even part,

$$\begin{aligned}\mathcal{H}^{\text{even}} =& \sum_n J_1 \left[\left(S^y_{n,1}S^y_{n,2} + S^z_{n,1}S^z_{n,2}\right)\cos\varphi + S^x_{n,1}S^x_{n,2}\right] \\ &+ J_1' \left[\left(S^y_{n,2}S^y_{n+1,1} + S^z_{n,2}S^z_{n+1,1}\right)\cos\gamma + S^x_{n,2}S^x_{n+1,1}\right] \\ &+ D_z\left(S^y_{n,1}S^y_{n,2} + S^z_{n,1}S^z_{n,2}\right)\sin\varphi - D_z'\left(S^y_{n,1}S^y_{n-1,2} + S^z_{n,1}S^z_{n-1,2}\right)\sin\gamma \\ &+ \sum_{i=1,2} J_2\left[\left(S^y_{n,i}S^y_{n+1,i} + S^z_{n,i}S^z_{n+1,i}\right)\cos\theta + S^x_{n,i}S^x_{n+1,i}\right],\end{aligned} \tag{4.10}$$

$$\begin{aligned}\mathcal{H}^{\text{odd}} =& \sum_n J_1\left(S^z_{n,1}S^y_{n,2} - S^y_{n,1}S^z_{n,2}\right)\sin\varphi + J_1'\left(S^z_{n,2}S^y_{n+1,1} - S^y_{n,2}S^z_{n+1,1}\right)\sin\gamma \\ &+ D_z\left(S^y_{n,1}S^z_{n,2} - S^z_{n,1}S^y_{n,2}\right)\cos\varphi + D_z'\left(S^y_{n,1}S^z_{n-1,2} - S^z_{n,1}S^y_{n-1,2}\right)\cos\gamma \\ &+ \sum_{i=1,2} J_2\left(S^z_{n,i}S^y_{n+1,i} - S^y_{n,i}S^z_{n+1,i}\right)\cos\theta.\end{aligned} \tag{4.11}$$

Applying the Holstein-Primakoff transformation and Fourier transformation on the unit cell

$$a_{n,i} = \frac{1}{\sqrt{N}}\sum_{\mathbf{k}} a_{i,\mathbf{k}} e^{i\mathbf{k}\cdot\mathbf{R}_{i,n}}, \tag{4.12}$$

where the summation runs over the first Brillouin zone. For now one only needs to care about $\mathcal{H}^{\text{even}}$, which yields the classical ground state energy and non-interacting quadratic Hamiltonian $\mathcal{H}^{(2)}$. Now with everything, the classical ground state energy is

$$E = S^2\left[\frac{1}{2}\left(J_1\cos\varphi + J_1'\cos\gamma + D_z\sin\varphi - D_z'\sin\gamma\right) + J_2\cos\theta\right]. \tag{4.13}$$

Unlike the case where DM terms are absent, the above equation is only solvable numerically. The solution to this confirms the validity of the $\mathbf{k}_{\text{m}}$-described magnetic structure. It turns out that by introducing the DM interactions, the system will either stay in the IC phase as the J_1-J_1'-J_2 case with a modified magnetic wave vector or it will form a variant of the UUDD phase which has some incommensurateness (Figure 4.3(a)).

The quadratic Hamiltonian $\mathcal{H}^{(2)}$ for calculating the linear spin wave is,

$$\mathcal{H}^{(2)} = S\sum_{\mathbf{k}} a^{\dagger}_{i,\mathbf{k}} A^{ij}_{\mathbf{k}} a_{j,\mathbf{k}} - \frac{1}{2}\left(a^{\dagger}_{i,\mathbf{k}} B^{ij}_{\mathbf{k}} a^{\dagger}_{j,-\mathbf{k}} + \text{h.c.}\right), \tag{4.14}$$

where the implicit summation applies for i, j. $A^{ij}_{\mathbf{k}}$ and $B^{ij}_{\mathbf{k}}$ are elements of the hermitian matrices $\mathbf{A_k}$ and $\mathbf{B_k}$, respectively. The explicit expression of them are

$$A^{11}_{\mathbf{k}} = A^{22}_{\mathbf{k}} = -J_1\cos\varphi - J_1'\cos\gamma - D_z\sin\varphi + D_z'\sin\gamma - 2J_2\cos\theta + J_2(\cos\theta+1)\cos 2\pi k, \tag{4.15}$$

$$A^{12}_{\mathbf{k}} = \left(A^{21}_{\mathbf{k}}\right)^* = \frac{1}{2}\left[\left(J_1\cos\varphi + J_1 + D_z\sin\varphi\right)e^{i\pi k} + \left(J_1'\cos\gamma + J_1' - D_z'\sin\gamma\right)e^{-i\pi k}\right], \tag{4.16}$$

$$B^{11}_{\mathbf{k}} = B^{22}_{\mathbf{k}} = \frac{1}{2}J_2\cos 2\pi k\left(\cos\theta - 1\right), \tag{4.17}$$

$$B^{12}_{\mathbf{k}} = \left(B^{21}_{\mathbf{k}}\right)^* = \frac{1}{2}\left[\left(J_1\cos\varphi - J_1 + D_z\sin\varphi\right)e^{-i\pi k} + \left(J_1'\cos\gamma - J_1' - D_z'\sin\varphi\right)e^{i\pi k}\right]. \tag{4.18}$$

Since the system is purely 1D so far, the scalar k will be used here to represent the x_0 component of $\mathbf{k}$ for simplicity.

Linear spin-wave dispersion branches of the system, $\varepsilon_{i,\mathbf{k}}$, are the square roots of eigenvalues of $S^2(\mathbf{A_k} - \mathbf{B_k})(\mathbf{A_k} + \mathbf{B_k})$. The boson operators in the eigenbasis are obtained by the generalized Bogolyubov transformation,

$$\begin{pmatrix} \mathbf{a_k} \\ \mathbf{a}^{\dagger}_{-\mathbf{k}} \end{pmatrix} = \begin{pmatrix} \mathbf{U_k} & \mathbf{V_k} \\ \mathbf{V_k} & \mathbf{U_k} \end{pmatrix} \begin{pmatrix} \mathbf{b_k} \\ \mathbf{b}^{\dagger}_{-\mathbf{k}} \end{pmatrix}, \tag{4.19}$$

where $\mathbf{a_q}$ and $\mathbf{b_q}$ represent the arrays of boson operators before and after the transformation. $\mathbf{U_q}$ and $\mathbf{V_q}$ are 2 by 2 matrices in this case.

In addition to this isotropic case, a x_0-y_0 easy-plane anisotropy can be easily added to J_1 and J_1' since this shall not change the co-planar spin structure stabilized by the DM interactions. The way to do this is by writing $J_1\mathbf{S}_{n,1}\cdot\mathbf{S}_{n,2}$ into $J_1(S^{x_0}_{n,1}S^{x_0}_{n,2} + S^{y_0}_{n,1}S^{y_0}_{n,2} +$

$\Delta S^{z_0}_{n,1} S^{z_0}_{n,2}$) and the same to J'_1 terms. The modification to the spin-wave Hamiltonian is small, with the matrix elements now become

$$A^{11}_{\mathbf{k}} = A^{22}_{\mathbf{k}} = -J_1 \cos\varphi - J'_1 \cos\gamma - D_z \sin\varphi + D'_z \sin\gamma - 2J_2 \cos\theta + J_2(\cos\theta + 1)\cos 2\pi k, \tag{4.20}$$

$$A^{12}_{\mathbf{k}} = \left(A^{21}_{\mathbf{k}}\right)^* = \frac{1}{2}\left[\left(J_1 \cos\varphi + J_1\Delta + D_z \sin\varphi\right) e^{i\pi k} + \left(J'_1 \cos\gamma + J'_1\Delta - D'_z \sin\gamma\right) e^{-i\pi k}\right], \tag{4.21}$$

$$B^{11}_{\mathbf{k}} = B^{22}_{\mathbf{k}} = J_2 \cos 2\pi k \left(\cos\theta - 1\right), \tag{4.22}$$

$$B^{12}_{\mathbf{k}} = \left(B^{21}_{\mathbf{k}}\right)^* = \frac{1}{2}\left[\left(J_1 \cos\varphi - J_1\Delta + D_z \sin\varphi\right) e^{-i\pi k} + \left(J'_1 \cos\gamma - J'_1\Delta - D'_z \sin\varphi\right) e^{i\pi k}\right]. \tag{4.23}$$

Note that the anisotropy ends up not being considered when simulating the experimental data.

The dynamic structure factor is defined as

$$\begin{aligned} \mathcal{S}^{\alpha\beta}(\mathbf{k},\omega) &= \int_{-\infty}^{\infty} \frac{\mathrm{d}t}{2\pi} e^{i\omega t} \frac{1}{N} \sum_{jk} e^{-i\mathbf{k}\cdot(\mathbf{r}_j - \mathbf{r}_k)} \left\langle S^\alpha_j(t) S^\beta_k \right\rangle \\ &= \sum_i \delta(\omega - \omega_i) \left\langle 0 \right| S^\alpha_{\mathbf{k}} \left| i \right\rangle \left\langle i \right| S^\beta_{\mathbf{k}} \left| 0 \right\rangle, \end{aligned} \tag{4.24}$$

where $\alpha, \beta \in \{x_0, y_0, z_0\}$ and j, k are indices of unit cells (the extended one). $|i\rangle$ denotes the ith excited state and ω_i the corresponding energy. $S^\alpha_{\mathbf{k}} = \frac{1}{\sqrt{N}} \sum_{i,n} S^\alpha_{i,n} e^{-i\mathbf{k}\cdot\mathbf{R}_{i,n}}$ where i labels the six sub-lattices. N is the total number of spins in the system.

When $\alpha = \beta$, it can be simplified as

$$\mathcal{S}^{\alpha\alpha}(\mathbf{k},\omega) = \sum_i \delta(\omega - \omega_i) \left| \left\langle 0 \right| S^\alpha_{\mathbf{k}} \left| i \right\rangle \right|^2. \tag{4.25}$$

We now manipulate Equation (4.9) using the identities that $\cos\theta = (e^{i\theta} + e^{-i\theta})/2$ and

$\sin\theta = -i(e^{i\theta} - e^{-i\theta})/2$ and obtain

$$S^{x_0}_{\mathbf{k}} = \sum_{i=1,2} \frac{i}{2} \left(S^{y}_{i,\mathbf{k}-\mathbf{k}_\mathrm{m}} e^{-i\delta_{i2}(\pi k_\mathrm{m} - \varphi)} - S^{y}_{i,\mathbf{k}+\mathbf{k}_\mathrm{m}} e^{i\delta_{i2}(\pi k_\mathrm{m} - \varphi)} \right) \tag{4.26}$$

$$+ \frac{1}{2} \left(S^{z}_{i,\mathbf{k}-\mathbf{k}_\mathrm{m}} e^{-i\delta_{i2}(\pi k_\mathrm{m} - \varphi)} + S^{z}_{i,\mathbf{k}+\mathbf{k}_\mathrm{m}} e^{-i\delta_{i2}(\pi k_\mathrm{m} - \varphi)} \right),$$

$$S^{y_0}_{\mathbf{k}} = \sum_{i=1,2} -\frac{1}{2} \left(S^{y}_{i,\mathbf{k}-\mathbf{k}_\mathrm{m}} e^{-i\delta_{i2}(\pi k_\mathrm{m} - \varphi)} + S^{y}_{i,\mathbf{k}+\mathbf{k}_\mathrm{m}} e^{i\delta_{i2}(\pi k_\mathrm{m} - \varphi)} \right) \tag{4.27}$$

$$+ \frac{1}{2i} \left(S^{z}_{i,\mathbf{k}-\mathbf{k}_\mathrm{m}} e^{-i\delta_{i2}(\pi k_\mathrm{m} - \varphi)} - S^{z}_{i,\mathbf{k}+\mathbf{k}_\mathrm{m}} e^{-i\delta_{i2}(\pi k_\mathrm{m} - \varphi)} \right),$$

$$S^{z_0}_{\mathbf{k}} = \sqrt{\frac{S}{2}} \sum_{i=1,2} S^{x}_{i,\mathbf{k}}, \tag{4.28}$$

where δ_{ij} is the Kronecker delta.

Within the linear spin-wave approximation, we map the transverse components $S^{x}_{i,\mathbf{k}}$ and $S^{y}_{i,\mathbf{k}}$ into linear combinations of a_i's

$$S^{x}_{i,\mathbf{k}} \approx \sqrt{\frac{S}{2}} (a_{i,\mathbf{k}} + a^{\dagger}_{i,-\mathbf{k}}), \tag{4.29}$$

$$S^{y}_{i,\mathbf{k}} \approx -i\sqrt{\frac{S}{2}} (a_{i,\mathbf{k}} - a^{\dagger}_{i,-\mathbf{k}}), \tag{4.30}$$

and the longitudinal component $S^{z}_{i,\mathbf{k}}$ is

$$S^{z}_{i,\mathbf{k}} = S\delta(\mathbf{k}) - \frac{1}{\sqrt{N}} \sum_{\mathbf{q}} a^{\dagger}_{i,\mathbf{q}} a_{i,\mathbf{q}-\mathbf{k}}, \tag{4.31}$$

which will be related to the magnetic Bragg peak and the longitudinal fluctuations in the dynamical structure factor of order $\mathcal{O}(1/S)$, beyond the level of linear spin wav approximation.

Now it is time to express $S^{\alpha}_{\mathbf{k}}$ in terms of a-bosons. The energy states in Equation (4.24) correspond to the magnon excitations, so we need to replace those a-bosons with b-bosons using Equation (5.91). The intermediate expressions are rather tedious. Therefore, the final

results are directly presented here

$$\mathcal{S}^{x_0x_0}(\mathbf{k},\omega) = \mathcal{S}^{y_0y_0}(\mathbf{k},\omega) = \frac{S}{8}\sum_{j=1,2}\delta(\omega-\omega_{j,\mathbf{k}-\mathbf{k}_\mathrm{m}})\left|\sum_{i=1,2}\left(U^{ij}_{\mathbf{k}-\mathbf{k}_\mathrm{m}}-V^{ij}_{\mathbf{k}-\mathbf{k}_\mathrm{m}}\right)e^{-i\delta_{i2}(\pi k_m-\varphi)}\right|^2 \tag{4.32}$$

$$+\frac{S}{8}\sum_{j=1,2}\delta(\omega-\omega_{j,\mathbf{k}+\mathbf{k}_\mathrm{m}})\left|\sum_{i=1,2}\left(U^{ij}_{\mathbf{k}+\mathbf{k}_\mathrm{m}}-V^{ij}_{\mathbf{k}+\mathbf{k}_\mathrm{m}}\right)e^{i\delta_{i2}(\pi k_m-\varphi)}\right|^2,$$

$$\mathcal{S}^{z_0z_0}(\mathbf{k},\omega) = \frac{S}{2}\sum_{j=1,2}\delta(\omega-\omega_{j,\mathbf{k}})\left|\sum_{i=1,2}U^{ij}_{\mathbf{k}}+V^{ij}_{\mathbf{k}}\right|^2. \tag{4.33}$$

Note that the inelastic scattering part is taken into account here, since there is no magnetic Bragg peaks observed in the real system.

Since spins lie in the x_0-y_0 plane with an incommensurate ordering wave vector, one can define the transverse part of the dynamical structure factor $\mathcal{S}^{\perp}$ as $\left(\mathcal{S}^{x_0x_0}+\mathcal{S}^{y_0y_0}\right)/2+\mathcal{S}^{z_0z_0}=\mathcal{S}^{x_0x_0}+\mathcal{S}^{z_0z_0}$. The method mentioned earlier will be used to efficiently compute the powder averaged spectrum.

Although it will not be useful here since powder spectra are poor at revealing any potential continuum, the longitudinal component $\mathcal{S}^{zz}$ can be straightforwardly calculated here particularly because it is a 1D Hamiltonian. $\mathcal{S}^{zz}$ corresponds to the two-magnon continuum.

As derived previously, the fluctuating part of $S^z_{i,\mathbf{k}}$ is

$$\delta S^z_{i,\mathbf{k}} = \frac{1}{\sqrt{N}}\sum_{\mathbf{q}} a^\dagger_{i,\mathbf{q}}a_{i,\mathbf{q}-\mathbf{k}}. \tag{4.34}$$

Considering the relevant term in the global reference frame, one has

$$\delta S^{x_0}_{i,\mathbf{k}} = \frac{1}{2\sqrt{N}}\sum_{\mathbf{q}}\sum_i a^\dagger_{i,\mathbf{q}}a_{i,\mathbf{q}-\mathbf{k}+\mathbf{k}_\mathrm{m}}e^{-i\delta_{i2}(\pi k_\mathrm{m}-\varphi)} + a^\dagger_{i,\mathbf{q}}a_{i,\mathbf{q}-\mathbf{k}-\mathbf{k}_\mathrm{m}}e^{i\delta_{i2}(\pi k_\mathrm{m}-\varphi)}. \tag{4.35}$$

From the fluctuation-dissipation theorem, there is

$$\mathcal{S}_{\parallel}(\mathbf{k},\omega) = -2\Theta(\omega)\mathrm{Im}\left[\mathcal{G}_{\parallel}(\mathbf{k},\omega)\right], \tag{4.36}$$

where the Heaviside step function $\Theta(\omega)$ indicates the quantity is nonzero only for $\omega > 0$ at zero temperature.

The corresponding Green function for a certain pair of sites $\{i,j\}$ is

$$\mathcal{G}_{\parallel}^{ij}(\mathbf{k},\omega) = -\frac{i}{2\pi}\int_{-\infty}^{\infty}\mathrm{d}t e^{i\omega t}\left\langle 0\right|\mathcal{T}\left[\delta S_{i,\mathbf{k}}^{z}(t)\delta S_{j,-\mathbf{k}}^{z}(0)\right]\left|0\right\rangle, \tag{4.37}$$

and after the coordinate transformation in our case,

$$\mathcal{G}_{\parallel}(\mathbf{k},\omega) = \frac{1}{4}\sum_{ij} e^{-i(\delta_{i2}-\delta_{j2})(\pi k_{\mathrm{m}}-\varphi)}\mathcal{G}_{\parallel}^{ij}(\mathbf{k}-\mathbf{k}_{\mathrm{m}},\omega) + e^{i(\delta_{i2}-\delta_{j2})(\pi k_{\mathrm{m}}-\varphi)}\mathcal{G}_{\parallel}^{ij}(\mathbf{k}+\mathbf{k}_{\mathrm{m}},\omega). \tag{4.38}$$

By computing the above Green function in a decoupled way, it is straightforward to obtain

$$\mathcal{S}_{\parallel}(\mathbf{k},\omega) = \Theta(\omega)\frac{1}{16}\sum_{\mathbf{q}}\sum_{\mu\nu}\left|\sum_{ij}\left[\left(U_{\mathbf{q}}^{i\mu}\right)^{*}V_{\mathbf{q}-\mathbf{k}+\mathbf{k}_{\mathrm{m}}}^{i\nu} + \left(V_{\mathbf{q}}^{i\mu}\right)^{*}U_{\mathbf{q}-\mathbf{k}+\mathbf{k}_{\mathrm{m}}}^{i\nu}\right]e^{-i\delta_{i2}(k_{\mathrm{m}}\pi-\varphi)}\right|^{2} \tag{4.39}$$

$$\begin{aligned}
&\delta(\omega-\omega_{\mathbf{q}}-\omega_{\mathbf{q}-\mathbf{k}+\mathbf{k}_{\mathrm{m}}}) \\
&+\left|\sum_{ij}\left[\left(U_{\mathbf{q}}^{i\mu}\right)^{*}V_{\mathbf{q}-\mathbf{k}-\mathbf{k}_{\mathrm{m}}}^{i\nu} + \left(V_{\mathbf{q}}^{i\mu}\right)^{*}U_{\mathbf{q}-\mathbf{k}-\mathbf{k}_{\mathrm{m}}}^{i\nu}\right]e^{i\delta_{i2}(k_{\mathrm{m}}\pi-\varphi)}\right|^{2} \\
&\delta(\omega-\omega_{\mathbf{q}}-\omega_{\mathbf{q}-\mathbf{k}-\mathbf{k}_{\mathrm{m}}}).
\end{aligned}$$

Now that all the derivation has been properly performed, the spin dynamical structure factor from the linear spin-wave theory is subsequently calculated based on the incipient classical ground states, to simulate the INS data. Since the excitations appear in two largely separate energy scales, it is intuitive to seek for suitable parameters where J_1 and J_1' are

fairly different. It turns out that only the UUDD phase is able to generate the one-magnon excitation branch with minimum at $Q = \pi/a$; and the incommensurate wave vector is subsequently induced by the DM terms.

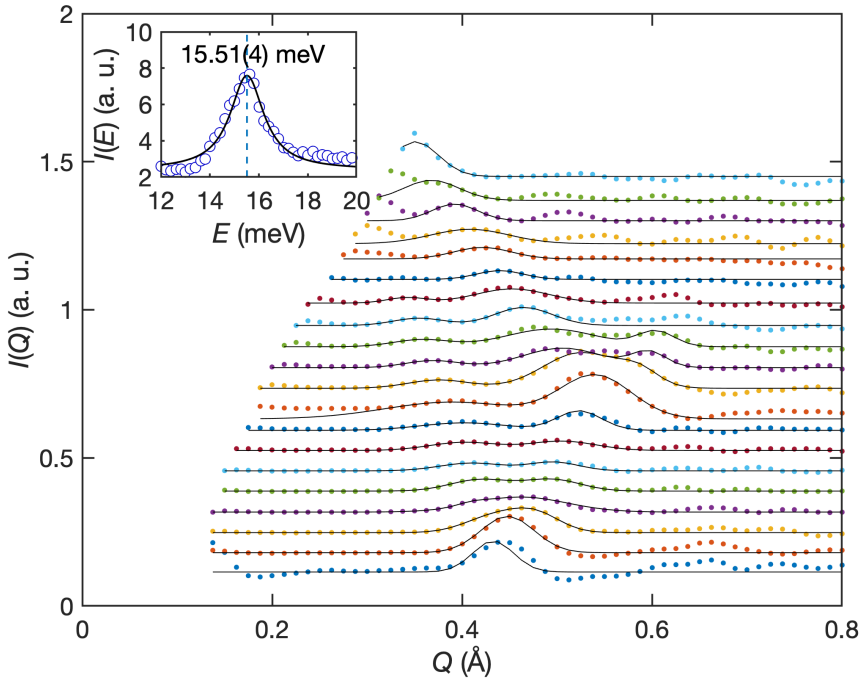

Figure 4.5: Constant-energy cuts on IN5 data and the corresponding fits for the dispersion branch extraction. Inset: The constant-Q cut and fit on CNCS data for the high-energy bandwidth.

From a simultaneous fit of the low energy branches extracted from the single-crystal spectra [Figure 4.5(c)] and the high-energy mode, the best parameters are found to be $J_1 = -13.9(5)$ meV, $J_1' = -1.61(3)$ meV, $J_2 = 2.2(1)$ meV, $D_1 = 1.6(1)$ meV and $D_1' = 1.36(2)$ meV. Error estimates of these parameters solely come from the fit. The details on how the single-crystal branch and high-energy mode are extracted are shown in [Figure 4.5]. Note that since the Hamiltonian is gapless due to its $U(1)$ symmetry, an artificial diagonal term $\Delta = 0.01$ meV is included in the quadratic spin-wave Hamiltonian to open a gap without disturbing the incipient ground state. This is to effectively account for the sub-leading terms such as interchain couplings which have been omitted in the current Hamiltonian.

Figure 4.2(b)-(e) and Figure 4.3(b)-(d) show excellent agreement between the powder neutron spectra and spin-wave simulation for both energy scales. Given that it is a drastically different spin Hamiltonian from those reported ones [61, 66], the success achieved from this spin-wave model is quite profound.

4.2.3 Thermodynamic properties and matrix-product state methods

Since the interpretation of inelastic neutron scattering data results in a drastically different microscopic model than the previously reported ones, it is crucial to seek evidence beyond the low-temperature spin dynamics. Thermodynamic properties such as specific heat and magnetic susceptibility serve such a purpose. Especially, within the 1D limit, such bulk properties can be simulated by the density-matrix purification method within the matrix product states (MPS) framework implemented in the iTensor library [67].

MPS is a way to represent the many-body quantum states. It is utilized in many numerical techniques, including the well-known DMRG. Given a system with N p-level particles, any state that describes its physical properties can be written as

$$|\Psi\rangle = \sum_{\sigma_1\sigma_2...\sigma_N} C_{\sigma_1\sigma_2...\sigma_N} |\sigma_1\rangle \otimes |\sigma_2\rangle \otimes \cdots \otimes |\sigma_N\rangle \,, \tag{4.40}$$

where $\sigma_r = 1, ..., p$ for an arbitrary particle with label r. Therefore, p^N parameters are needed for such a description which is computationally impractical.

If one considers the open indices to correspond to the local states from Equation (4.40), and uses the following notation

$$|\sigma\rangle \equiv |\sigma_1\rangle \otimes |\sigma_2\rangle \otimes \cdots \otimes |\sigma_N\rangle \,, \tag{4.41}$$

a matrix product state with open boundary condition is then given by

$$|\psi\rangle = \sum_{\{\sigma\}} \left(\langle \phi_{\mathrm{L}} | \prod_{r=1}^{N} \hat{A}\left[\sigma_r\right] | \phi_{\mathrm{R}} \rangle \right) |\sigma\rangle \,, \tag{4.42}$$

where $\hat{A}\left[\sigma_r\right]$ is a linear operator depending locally on the rth site and maps from some D-dimensional auxiliary state space spanned by an orthonormal basis $\{|\beta\rangle\}$ to another D-dimensional auxiliary state space spanned by an orthonormal basis $\{|\alpha\rangle\}$:

$$\hat{A}\left[\sigma_r\right] = \sum_{\alpha\beta} \left(A\left[\sigma_r\right]\right)_{\alpha\beta} |\alpha\rangle\langle\beta| \,, \tag{4.43}$$

and $\left|\phi_{\mathrm{L(R)}}\right\rangle$ are the left (right) boundary states in the auxiliary space. For periodic boundary conditions, those two boundary states are replaced by trace operation:

$$|\psi\rangle = \sum_{\{\sigma\}} \left(\mathrm{Tr} \prod_{r=1}^{N} \hat{A}\left[\sigma_r\right] \right) |\sigma\rangle \,. \tag{4.44}$$

When identical sites are considered, it demands that

$$\sum_{\sigma_r} \hat{A}\left[\sigma_r\right] \hat{A}^{\dagger}\left[\sigma_r\right] = \hat{\mathbb{I}}. \tag{4.45}$$

There are various neat properties, such as the area law and finite correlations that make MPS a very good representation for 1D systems. In principle, MPS possess completeness and can describe any state as long as the dimension D grows sufficiently and exponentially as needed. In practice, however, D will be set to some adequate value such that simulation can be done in polynomial time. This is essentially where the truncation or compression happens.

From statistical mechanics, one knows that the thermal properties of a many-body quan-

tum system in equilibrium can be retrieved from the thermal density matrix,

$$\hat{\rho} = \frac{1}{Z} e^{-\beta \hat{H}}, \tag{4.46}$$

where Z is the thermal partition function and $\beta \equiv 1/T$ is the inverse temperature. The purification method starts from constructing maximally entangled states between the system and the artificial environment at infinite temperature and evolving the Hamiltonian towards low temperatures by employing the MPS techniques for imaginary time evolution. Until it becomes extremely costly and fails at very low temperature, the method is shown to describe the bulk properties of 1D quantum system very well [68]. Potentially thanks to the classical nature of the UUDD state, the method worked quite efficiently here down to $T \sim 2$ K.

Figure 4.7 presents the comparison between the experimental data and the simulated results using the model Hamiltonian. The simulation used a 36-unit-cell chain which was verified to be sufficient, as illustrated in Figure 4.6. To obtain the best match with both specific heat and magnetic susceptibility, all exchange parameters are scaled down by a factor of 0.75, which may be attributed to the higher-order quantum fluctuations neglected in LSWT. The grey area in the specific heat plot is from a fit with two Debye models. With this degree of freedom, specific heat is actually rather tolerant with a certain range of scaling of the energy.

Apart from the anticipated failure at extremely low temperatures, the simulation captures the transition around $T \sim 6$ K [Figure 4.7(a)]. Meanwhile, a broad peak in specific heat around $T \sim 50$ K [Figure 4.6(a)], which would be overwhelmed by the phonon contribution in the actual compound, is predicted. This is consistent with the high-energy magnetic excitation being much more persistent than the low-energy ones [Figure 4.7(d),(e)]. Using the same parameters and scale factor, we also calculated isothermal magnetization curve $M(B)$ at zero temperature using density matrix renormalization group (DMRG) tech-

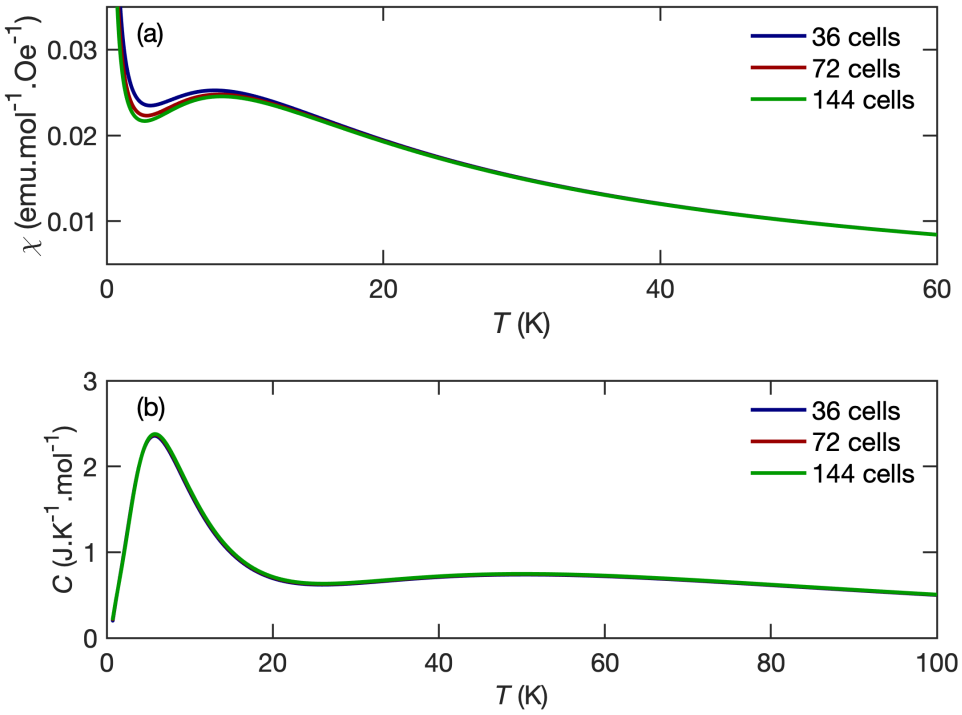

Figure 4.6: The purification simulation of (a) magnetic susceptibility and (b) specific heat with different numbers of unit cells used.

nique. An isotropic g-factor 2.2 provided by the typical Cu^{2+} behavior is assumed lacking further information. The powder nature of the actual measurement hinders a direct comparison. However, it is very reasonable to believe the system is not fully saturated below $B = 20$ T [Figure 4.7(c)].

The arbitrariness of the scale factor that is applied here does somewhat hurt the consistency between the simulation here and the linear spin-wave calculation, even though a renormalization of the bandwidth from higher-order quantum effects may account for this. However, the absolute quantitative robustness is not what is intended here. First, the simulated heat capacity manages to justify the two energy scales observed in the inelastic neutron data which have different temperature dependence [Figure4.8]. Second, it asserts that it is feasible to describe the thermodynamic properties based on a very different model than what have been previously reported [61, 66].

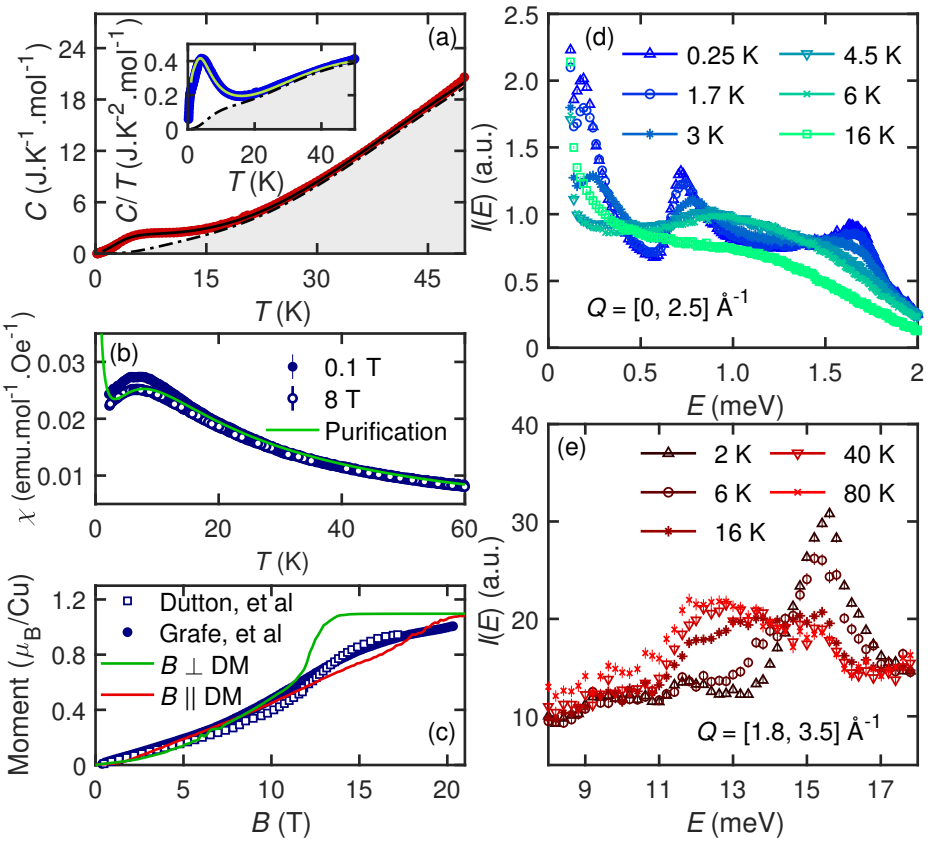

Figure 4.7: (a) Zero-magnetic-field specific heat results. (b) Zero-field-cooled magnetic susceptibility compared with simulation from purification method. (c) Magnetization curves reproduced from previous literatures compared with zero-temperature magnetization calculated by DMRG with different field directions. (d),(e) Representative Q-integrated cuts as functions of energy transfer at various temperatures.

4.2.4 The effective spin-one picture and in-field study

This resulting Hamiltonian indicates a strong ferromagnetic pairing in which the two spin-halves bonded by J_1 form effective spin-one triplets. Within this picture, the high-energy excitation loosely corresponds to the triplet-singlet transition. Meanwhile, neglecting the slight distortion caused by D_1, one may describe the low energy spin dynamics by mapping the system into a spin-one Hamiltonian,

$$\tilde{\mathcal{H}} = \sum_n \tilde{J}\tilde{\mathbf{S}}_n \cdot \tilde{\mathbf{S}}_{n+1} + \tilde{\mathbf{D}} \cdot \left(\tilde{\mathbf{S}}_n \times \tilde{\mathbf{S}}_{n+1}\right), \tag{4.47}$$

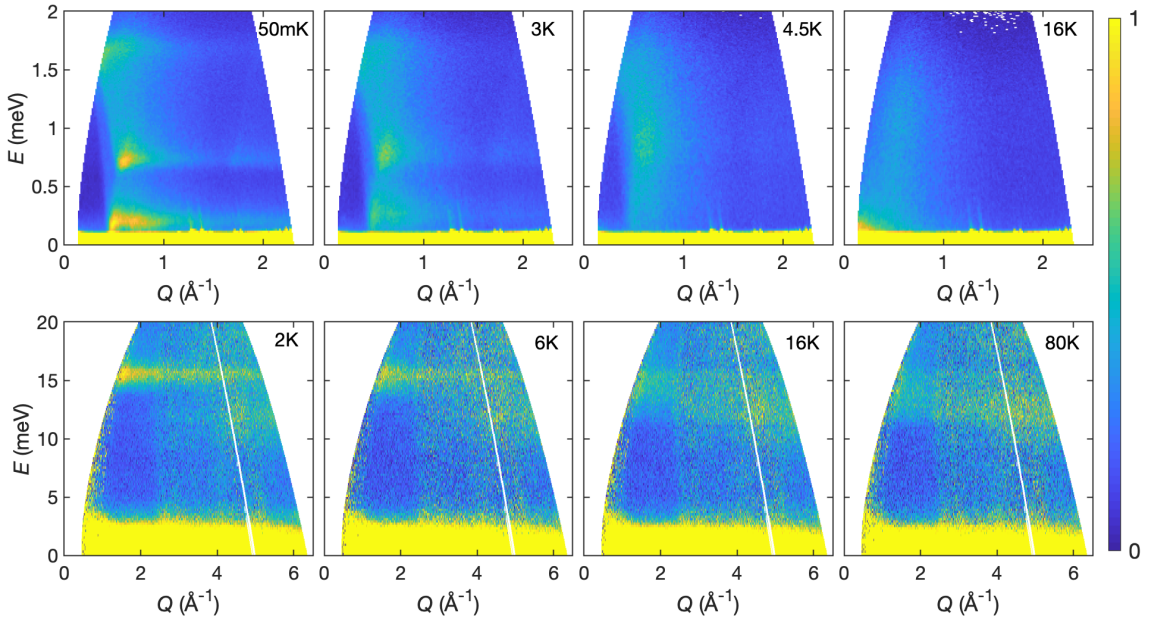

Figure 4.8: Upper panels: The inelastic neutron data with different temperatures collected at IN5, ILL with the incident neutron wavelength $\lambda_{\mathrm{i}} = 5$ Å. Lower panels: The inelastic neutron data with different temperatures collected at CNCS, SNS with the incident neutron energy $E_{\mathrm{i}} = 25$ meV.

where $\tilde{J} \equiv (J_1' + 2J_2)/4$, $\tilde{\mathbf{D}} \equiv \mathbf{D}_1'/4$, and $\tilde{S}^{\alpha}$ is the spin-one operator. In our case, $\tilde{J} \sim 0.7$ meV leads to an antiferromagnetic spin-one chain. The neglect of D_1 can be well justified from its minimal impact on the classical ground states, which are illustrated in terms of pitch angles in Figure 4.9.

The pitch angle between adjacent spin-one's is the angle θ defined previously. Under this simplified model, it can be obtained analytically by solving

$$\tilde{J}\sin\theta - \tilde{D}\cos\theta = 0; \tag{4.48}$$

$$\tilde{J}\cos\theta + \tilde{D}\sin\theta < 0. \tag{4.49}$$

Now one can perform LSWT on this spin-one model. Like before, there is the quadratic Hamiltonian

$$\tilde{\mathcal{H}}^{(2)} = \tilde{S}\sum_{\mathbf{k}} a_{\mathbf{k}}^{\dagger}\tilde{A}_{\mathbf{k}}a_{\mathbf{k}} - \frac{1}{2}\left(a_{\mathbf{k}}^{\dagger}\tilde{B}_{\mathbf{k}}a_{-\mathbf{k}}^{\dagger} + \mathrm{h.c.}\right), \tag{4.50}$$

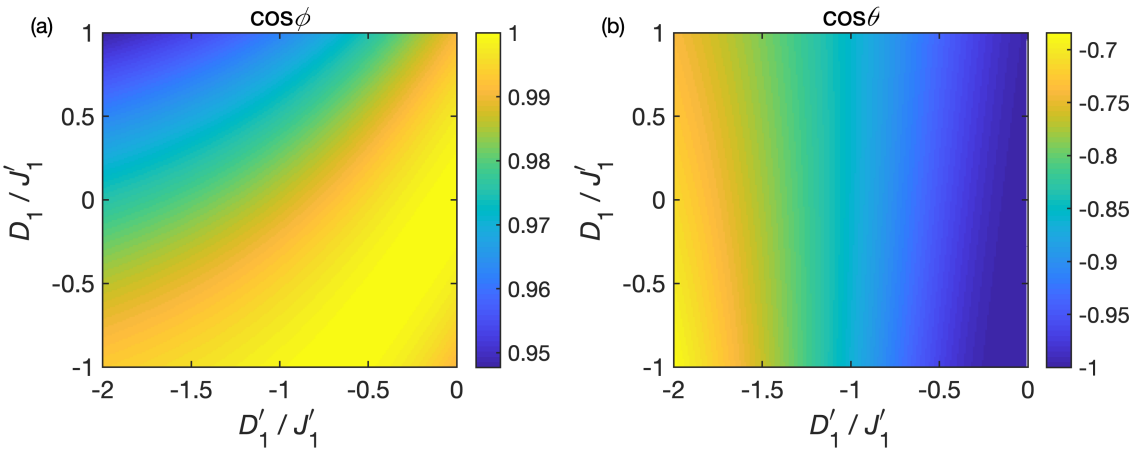

Figure 4.9: Color plots of pitch angle cosines as functions of D_1/J_1' and D_1'/J_1'. The absolute values of J_1, J_1' and J_2 are fixed to what give the best match between the experiment and LSWT calculation.

where

$$\tilde{A}_{\mathbf{k}} = \left[\tilde{J}\left(\cos\theta + \Delta\right) + \tilde{D}\sin\theta\right]\cos 2\pi k - 2\tilde{J}\cos\theta - 2\tilde{D}\sin\theta, \tag{4.51}$$

$$\tilde{B}_{\mathbf{k}} = \left[\tilde{J}\left(\cos\theta - \Delta\right) + \tilde{D}\sin\theta\right]\cos 2\pi k. \tag{4.52}$$

The fact $\tilde{A}_{\mathbf{k}}$ and $\tilde{B}_{\mathbf{k}}$ are scalars means there is only one excitation branch in the chosen magnetic cell. As a result, starting from the spin-one chain model simplifies the calculation and leads to a concise expression for the low-energy excitation

$$\tilde{\varepsilon}_{\mathbf{k}} = 2\tilde{S}\sqrt{\Lambda\left(\tilde{J}\cos 2\pi k + \Lambda\right)\left(1 - \cos 2\pi k\right)}, \tag{4.53}$$

where $\Lambda \equiv -\tilde{J}\cos\theta - \tilde{D}\sin\theta$ and $\theta = 2\pi k_{\mathrm{m}}$ is the pitch angle between adjacent unit cells. As shown in Figure 4.10(a), the low-energy spin-wave excitations calculated from the original spin-half and the effective spin-one Hamiltonian have an excellent match. This validates the truncation that has been performed.

The spin dynamical structure factors of the spin-one model are

$$\tilde{\mathcal{S}}^{x_0x_0}(\mathbf{k},\omega) = \tilde{\mathcal{S}}^{y_0y_0}(\mathbf{k},\omega) = \frac{S}{8}\left[\delta(\omega-\omega_{\mathbf{k}-\mathbf{k}_\mathrm{m}})\left(u_{\mathbf{k}-\mathbf{k}_\mathrm{m}}-v_{\mathbf{k}-\mathbf{k}_\mathrm{m}}\right)^2+\delta(\omega-\omega_{\mathbf{k}+\mathbf{k}_\mathrm{m}})\left(u_{\mathbf{k}+\mathbf{k}_\mathrm{m}}-v_{\mathbf{k}+\mathbf{k}_\mathrm{m}}\right)^2\right], \tag{4.54}$$

$$\tilde{\mathcal{S}}^{z_0z_0}(\mathbf{k},\omega) = \frac{S}{2}\delta(\omega-\omega_{\mathbf{k}})\left(u_{\mathbf{k}}+v_{\mathbf{k}}\right)^2. \tag{4.55}$$

With the above knowledge, it becomes easy to simulate the 3D system by speculatively incorporating the interchain coupling with the spin-one chain. Because the coupling strength is not expected to influence the high-energy branch. At the long-wavelength limit where the momentum is approaching zero or $\mathbf{k}_\mathrm{m}$, the dispersion becomes

$$\tilde{\varepsilon}_{\mathbf{k}} = \sqrt{8}\pi\tilde{S}\Lambda k + \mathcal{O}\left(k^2\right) \approx \sqrt{8}\pi\tilde{S}\Lambda k, \tag{4.56}$$

where k refers to $k(\pm k_\mathrm{m})$. In the vicinity of this, the following phenomenological equation

$$\tilde{\varepsilon}^{\mathrm{3D}}_{\mathbf{k}} \approx \tilde{S}\sqrt{2\left(\Lambda 2\pi k_x\right)^2+\tilde{J}_\mathrm{ic}\gamma(k_y,k_z)}, \tag{4.57}$$

may be applied to approximate the dispersion of weakly-coupled chains, as in the actual compound. $\tilde{J}_\mathrm{ic} > 0$ is the effective interchain coupling strength and,

$$\gamma(k_y,k_z) = 3 - 2\cos^2\pi k_y - \cos^2\frac{\pi k_y}{2}\cos^2\pi k_z, \tag{4.58}$$

is a structure factor loosely respecting the geometrical configuration. The fact that $\gamma(0,0) = 0$ is to ensure wave vector in the 3D case remains $(k_\mathrm{m},0,0)$. Meanwhile, the Bogolyubov

coefficients $u_{\mathbf{k}}$ and $v_{\mathbf{k}}$ for the 1D case are just numbers, the solution to them are simply

$$u_{\mathbf{k}} = \sqrt{\left| \frac{\tilde{S}\tilde{A}_{\mathbf{k}}}{2\tilde{\varepsilon}_{\mathbf{k}}} + 1 \right|}, \tag{4.59}$$

$$v_{\mathbf{k}} = \mathrm{sign}(\tilde{B}_{\mathbf{k}}) \sqrt{\left| \frac{\tilde{S}\tilde{A}_{\mathbf{k}}}{2\tilde{\varepsilon}_{\mathbf{k}}} - 1 \right|}, \tag{4.60}$$

which are linear with $\sqrt{1/k}$ in the same limit.

Since the spin dynamical structure factor $\mathcal{S}(\mathbf{k}, \omega)$ consists of quadratic terms of $u_{\mathbf{k}}$ and $v_{\mathbf{k}}$, it can be approximated as

$$\mathcal{S}(\mathbf{k}, \omega)|_{k_x(\pm k_{\mathrm{m}}) \to 0} \propto \frac{\delta(\omega - \tilde{\varepsilon}^{\mathrm{3D}}_{\mathbf{k}})}{k_x(\pm k_{\mathrm{m}})}. \tag{4.61}$$

The concise expression above allows one to conveniently simulate the effect of interchain coupling. Figure 4.10(b) and (c) present the experimental data compared with the calculated result which is essentially the powder average based on the above equation. An effective $J_{\mathrm{ic}} = 0.12$ meV gives a decent agreement. Note that while a proper bandwidth is simulated, this method does not introduce any excitation gap.

While the above phenomenological treatment yields a satisfactory outcome, it is necessary to point out that the actual compound has multiple chains with different Cu-O bond orientations in one crystallographic unit cell [Figure 4.1]. A single cell cannot be described by a single magnetic wave vector even if chains have absolutely zero coupling. Needless to say that the directions of the DM terms are also non-uniform across chains. Therefore, single crystal samples would be crucial if one intended to conduct a more thorough investigation on the interchain coupling, which is beyond the scope here since there is only powder averaged data available.

The spin-one picture also makes it simpler to study the low-energy spin excitations under the applied magnetic field, because it would be less straightforward with two spins

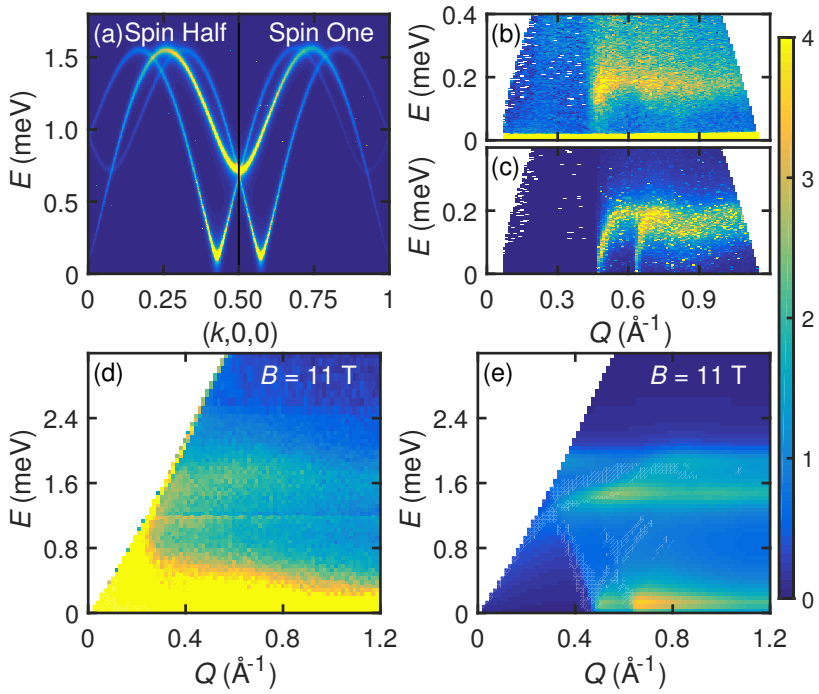

Figure 4.10: (a) Comparison of low-energy spin-wave excitations calculated by the original spin-half model and the effective spin-one model. (b),(c) INS data of extremely-low-energy excitations compared with the spin-wave calculation on the effective spin-one model incorporated with effective interchain coupling $J_{\rm ic} = 0.12$ meV. (d),(e) Powder INS data measured in applied magnetic field compared with the corresponding spin-wave calculation on the spin-one model.

in a cell in the original spin-half case. Moreover, it would also be somewhat redundant since it is only the low energy that is meaningful to study here. That is because for a pair of spin-1/2 with Landé factor $g = 2.1$, a 11-Tesla magnetic field yields a Zeeman energy of ~ 1.34 meV, which is smaller than 10% of J_1. This means the high-energy mode is virtually unchangeable by any realistic magnetic field.

In practice of the spin-wave calculation, the field is applied perpendicular to the spin plane established by the DM interaction and induce a canted incommensurate phase. The reason for that is to apply the field along other directions, such as within the spin plane, would be complicated and unfeasible. Meanwhile, the collected powdered INS data in field does not have a well-defined field orientation and already prohibits any quantitative benchmark at the first place.

The transformation of spin operators from the global coordinates to the local ones can be achieved by two steps of rotation,

$$\mathbf{S}_i^0 = \mathbf{R}_{\mathbf{k}_\mathrm{m}} \mathbf{R}_\eta \mathbf{S}_i, \tag{4.62}$$

where the matrix $\mathbf{R}_{\mathbf{k}_\mathrm{m}}$ does the in-plane rotation,

$$\mathbf{R}_{\mathbf{k}_\mathrm{m}} = \begin{pmatrix} \cos\theta_i & -\sin\theta_i & 0 \\ \sin\theta_i & \cos\theta_i & 0 \\ 0 & 0 & 1 \end{pmatrix}, \tag{4.63}$$

where $\varphi_i \equiv \mathbf{k}_\mathrm{m} \cdot \mathbf{r}_i$. The matrix $\mathbf{R}_\eta$ is related to the canting angle η,

$$\mathbf{R}_\eta = \begin{pmatrix} \sin\eta & 0 & \cos\eta \\ 0 & 1 & 0 \\ -\cos\eta & 0 & \sin\eta \end{pmatrix}. \tag{4.64}$$

Overall, the transformation is as the following,

$$S_i^{x_0} = S_i^x \sin\eta\cos\theta_i - S_i^y \sin\theta_i + S_i^z \cos\eta\cos\theta_i, \tag{4.65}$$

$$S_i^{y_0} = S_i^x \sin\eta\sin\theta_i + S_i^y \cos\theta_i + S_i^z \cos\eta\sin\theta_i, \tag{4.66}$$

$$S_i^{z_0} = -S_i^x \cos\eta + S_i^z \sin\eta. \tag{4.67}$$

The two angles are obtained again by minimizing the classical ground state energy,

$$E = \tilde{S}^2 \left[\tilde{J} \left(\sin^2\eta + \cos^2\eta\cos\theta \right) + \tilde{D}\cos^2\eta\sin\theta - \left(g\mu_\mathrm{B} H \sin\eta \right) / \tilde{S} \right]. \tag{4.68}$$

Likewise, the quadratic Hamiltonian is derived as the following,

$$\tilde{\mathcal{H}}^{(2)} = \tilde{S}\sum_{\mathbf{k}}\left(\tilde{A}_{\mathbf{k}} + \tilde{C}_{\mathbf{k}}\right)a^{\dagger}_{\mathbf{k}}a_{\mathbf{k}} - \frac{1}{2}\left(a^{\dagger}_{\mathbf{k}}\tilde{B}_{\mathbf{k}}a^{\dagger}_{-\mathbf{k}} + \text{h.c.}\right), \tag{4.69}$$

where

$$\begin{aligned}
\tilde{A}_{\mathbf{k}} =& \left[\tilde{J}\left(\cos\theta + \sin^2\eta\cos\theta + \cos^2\eta\right) + \tilde{D}\left(\sin\theta + \sin^2\eta\sin\theta\right)\right]\cos 2\pi k \qquad (4.70)\\
&- 2\tilde{J}\left(\cos^2\eta\cos\theta + \sin^2\eta\right) - 2\tilde{D}\cos^2\eta\sin\theta + \left(g\mu_{\text{B}}H\sin\eta\right)/\tilde{S},\\
\tilde{B}_{\mathbf{k}} =& \left[\tilde{J}\left(\cos\theta - \sin^2\eta\cos\theta - \cos^2\eta\right) + \tilde{D}\left(\sin\theta - \sin^2\eta\sin\theta\right)\right]\cos 2\pi k, \qquad (4.71)\\
\tilde{C}_{\mathbf{k}} =& 2\tilde{J}\sin\theta\sin\eta\sin 2\pi k. \qquad (4.72)
\end{aligned}$$

Because $\tilde{C}_{-\mathbf{k}} = -\tilde{C}_{\mathbf{k}}$, the term is insensitive to the Bogolyubov transformation. As a result, the spin-wave dispersion is

$$\tilde{\varepsilon}_{\mathbf{k}} = \sqrt{\tilde{A}^2_{\mathbf{k}} - \tilde{B}^2_{\mathbf{k}}} + \tilde{C}_{\mathbf{k}}. \tag{4.73}$$

Following the same recipe with slightly more complicated arithmetics, the dynamical structure factors are derived,

$$\begin{aligned}
\mathcal{S}^{x_0x_0}(\mathbf{k},\omega) =& \frac{1}{4}\\
&\left[\mathcal{S}^{yy}_{\mathbf{k}_+} + \mathcal{S}^{yy}_{\mathbf{k}_-} - 2i\sin\eta\left(\mathcal{S}^{xy}_{\mathbf{k}_+} - \mathcal{S}^{xy}_{\mathbf{k}_-}\right) + \sin^2\eta\left(\mathcal{S}^{xx}_{\mathbf{k}_+} + \mathcal{S}^{xx}_{\mathbf{k}_-}\right) + \cos^2\eta\left(\mathcal{S}^{zz}_{\mathbf{k}_+} + \mathcal{S}^{zz}_{\mathbf{k}_-}\right)\right],\\
\mathcal{S}^{y_0y_0}(\mathbf{k},\omega) =& \mathcal{S}^{x_0x_0}(\mathbf{k},\omega), \qquad (4.74)\\
\mathcal{S}^{z_0z_0}(\mathbf{k},\omega) =& \cos^2\eta\mathcal{S}^{xx}_{\mathbf{k}} + \sin^2\eta\mathcal{S}^{zz}_{\mathbf{k}},
\end{aligned}$$

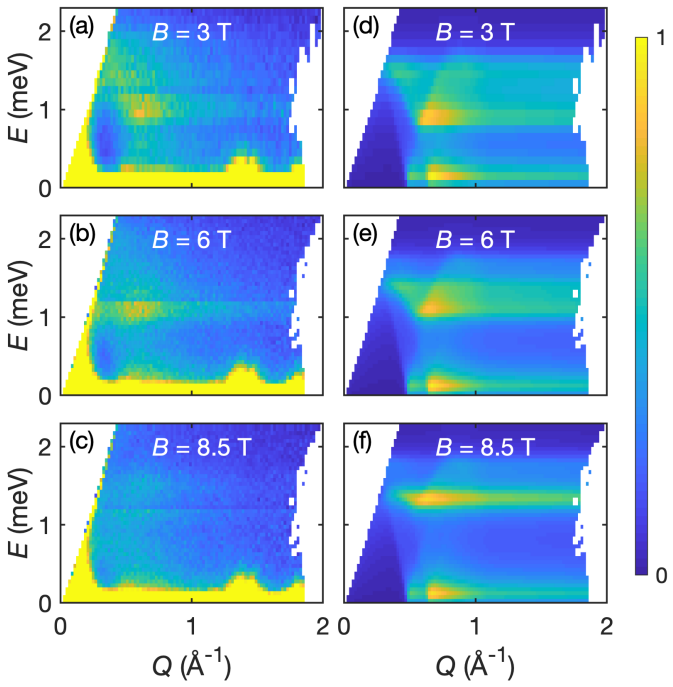

Figure 4.11: (a)-(c) INS spectra from MACS at $T \sim 0.1$ K with various applied magnetic fields and (d)-(f) the corresponding linear spin-wave results based on the effective spin-one model.

where $\mathbf{k}_{\pm} \equiv \mathbf{k} \pm \mathbf{k}_{\mathrm{m}}$ and

$$\begin{aligned}
\mathcal{S}^{xx}(\mathbf{k},\omega) &= \frac{S}{2}\left(u_{\mathbf{k}} + v_{\mathbf{k}}\right)^2 \delta(\omega - \omega_{\mathbf{k}}), \\
\mathcal{S}^{yy}(\mathbf{k},\omega) &= \frac{S}{2}\left(u_{\mathbf{k}} - v_{\mathbf{k}}\right)^2 \delta(\omega - \omega_{\mathbf{k}}), \\
\mathcal{S}^{xy}(\mathbf{k},\omega) &= i\frac{S}{2}(u_{\mathbf{k}} + v_{\mathbf{k}})\left(u_{\mathbf{k}} - v_{\mathbf{k}}\right)\delta(\omega - \omega_{\mathbf{k}}) = i\frac{S}{2}\delta(\omega - \omega_{\mathbf{k}}),
\end{aligned} \tag{4.75}$$

where the last equation above uses the fact that $u_{\mathbf{k}}^2 - v_{\mathbf{k}}^2 = 1$. Again, $\mathcal{S}^{zz}$ which at this level only yields the magnetic Bragg peaks is omitted.

The powder average spectra are thus calculated from the derivation. As shown by Figure 4.10(d) and (e), the spin-wave excitations in 11-Tesla field have the correct bandwidth and produce the major features observed from the data collected on MACS at $T \sim 0.1$ K. Moreover, the consistency extends to other fields, which are presented in Figure 4.11. One can also see from there how the spectra start to resemble the zero-field case as the field

decreases.

4.3 Conclusions

Through a comprehensive study on $LiCuSbO_4$ using various experimental and theoretical techniques, it is believed that the microscopic picture behind the system has been unambiguously revealed. What is remarkable is that in spite of a 1D system that does not exhibit any long-range magnetic ordering down to the lowest achievable temperature, the spin-wave theory works surprisingly well to capture most of the features of the spin dynamics. This is possibly due to the classical nature of the UUDD state in the absence of the DM terms. Meanwhile, one should also recall that even for the simple spin-half chain, a renormalized spin-wave band can also mimic the lower-bound of the spinon states.

Moreover, this best description by far of the system is achieved based on a drastically different model from what have previously been reported [61, 66, 69]. Such a solid understanding of the actual compound is absolutely crucial in the path of exploring and realizing novel phases. Especially since many of those novel phases still lack smoking-gun signatures to be validated, any misconception of the actual material may lead to a different conclusion.

The fact that nearest neighbor couplings have significant dimerization suggests that even a slight distortion in the structure can lead to strong influence in low-temperature behaviors and ought not to be simply neglected. As was the focus of numerous previous studies, the question whether the system could host any spin nematic phase in the presence of a nearly saturating magnetic field may still be worth asking, since the $U(1)$ symmetry is still preserved in the spin Hamiltonian. And no finite magnetic moment has ever been detected experimentally from the system at any temperature or magnetic field implying phases with some unbroken symmetry.

The resulting model seems to host emergent spin-one physics due to the strong ferromagnetic J_1 bond. Since numerical simulation is relatively cost efficient for 1D systems, it

is perhaps worthwhile to speculate about this via exploring a broader parameter space for a more comprehensive quantum phase diagram.

CHAPTER 5

NORMAL AND ANOMALOUS SPIN DYNAMICS IN THE QUASI-2D SPIN-$\frac{1}{2}$ TRIANGULAR LATTICE ANTIFERROMAGNET

5.1 Triangular lattice antiferromagnet - a paradigm for geometrical frustration

The triangular lattice antiferromagnet (TLAF) is the simplest model which exemplifies geometrical frustration. Frustration yields degeneracy. For instance, in the Ising limit, competing bonds on the smallest triangle have led physicists to believing the system has non-unique ground states. In fact, the residual entropy for the triangular Ising antiferromagnet at absolute zero temperature, a strong indication of degeneracy, has been calculated by Wannier [70] using the method developed by Kaufman and Onsager [71].

The Heisenberg case is more complicated. Although a magnetically ordered ground state is relatively trivial in the large-S limit, the quantum limit where spin is $1/2$ historically had a long debate on whether it could stabilize an ordered ground state. Meanwhile, Anderson proposed the resonant valence bond (RVB) state [72] which became the very first strongly entangled quantum state and has sparked significant interests since then. Nowadays, the concept and relevant studies have been extended onto many other systems with different kinds of geometries and bondings.

Eventually, the stable long-range Néel ordering is widely agreed upon with the advent of convincing numerical results from techniques such as Green function's Monte Carlo [73] and DMRG [74]. Based on such a non-collinear 120° magnetic structure, theorists have done quite thorough studies using spin-wave theory on the system discussing the magnetic moment reduction, magnon instability and excitation spectra [7, 8, 75].

However, an ideal experimental realization still lacks. Among all the reported candidate compounds, $Ba_8CoNb_6O_{24}$ [76, 77] has the most promising results. The absence

of its single-crystal sample, however, prevents further conclusive discussion. As such, $Ba_3CoSb_2O_9$ has been standing out. The availability of its single crystal has enabled numerous experimental investigations. While many of its magnetic properties are found to be consistent with the theoretical prediction, there remain unresolved mysteries, particularly the spin dynamics. The work here attempts to introduce and discuss the spin dynamics of this material in a detailed manner with the spin-wave theory still serving as the primary theoretical tool.

The sample used for the research in this chapter was grown by Haidong Zhou at University of Tennessee, Knoxville.

5.2 $Ba_3CoSb_2O_9$ - the imperfect yet best experimental realization

5.2.1 Crystal structure and the spin-half nature

$Ba_3CoSb_2O_9$ crystallizes in a highly symmetric hexagonal structure, $P6_3/mmc$. The magnetic ions Co^{2+} inside the CoO_6 octahedra form equilateral triangular-lattice layers in the ab plane [Figure 5.1(a)]. The origin of its magnetic moment differs from the typical picture mentioned in the first chapter for a $3d$ transition metal oxide. Under a uniaxial crystal field from spin-orbital coupling, Co^{2+} goes through a high-spin ($\frac{3}{2}$) to low-spin ($\frac{1}{2}$) transition as temperature decreases. At low temperatures that are relevant to the study here, the ground state is a Kramers doublet which can be described effectively by a spin-half [78].

5.2.2 The 120° magnetic structure and magnetization plateau

It has been confirmed by neutron diffraction experiments that the system forms a 120° non-collinear long-range magnetic order below $T_{\rm N} \approx 3.8$K in zero magnetic field and adjacent triangular layers are coupled with antiferromagnetic exchange interactions. Moreover, magnetic moments reside within ab-plane, indicating the existence of a small easy-plane anisotropy in the nearest-neighbor exchange coupling. This leads to the following generic

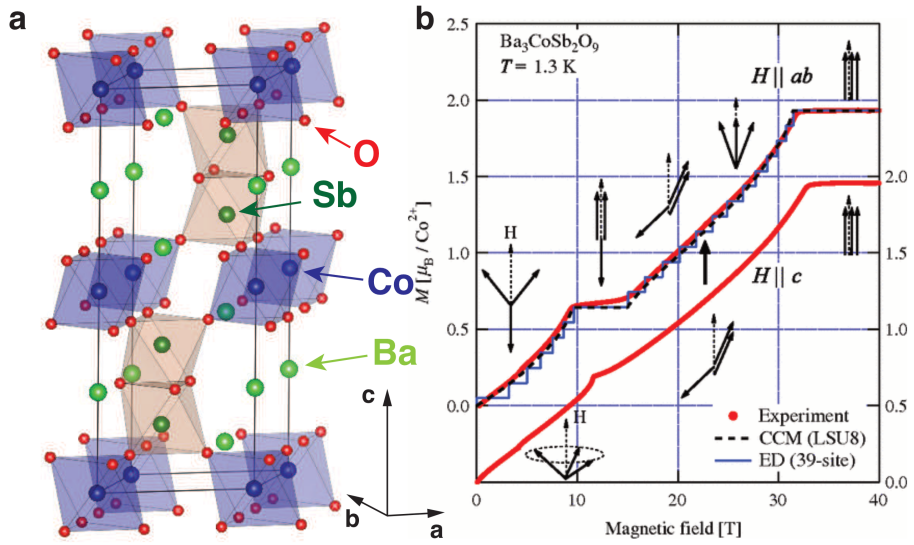

Figure 5.1: This figure is made based on Ref. [79] and Ref. [80]. (a) The crystal structure of $Ba_3CoSb_2O_9$. (b) The magnetization curves with the magnetic field applied in the ab-plane or along c-axis.

yet minimal Hamiltonian that respects all of the constraints,

$$\begin{aligned}\mathcal{H} =& J \sum_{\langle \mathbf{r}\mathbf{r}' \rangle} \left(S^x_{\mathbf{r}} S^x_{\mathbf{r}'} + S^y_{\mathbf{r}} S^y_{\mathbf{r}'} + \Delta S^z_{\mathbf{r}} S^z_{\mathbf{r}'} \right) \\ &+ J_c \sum_{\mathbf{r}} \left(S^x_{\mathbf{r}} S^x_{\mathbf{r}+\frac{\mathbf{c}}{2}} + S^y_{\mathbf{r}} S^y_{\mathbf{r}+\frac{\mathbf{c}}{2}} + \Delta S^z_{\mathbf{r}} S^z_{\mathbf{r}+\frac{\mathbf{c}}{2}} \right) - \mu_{\mathbf{B}} \sum_{\mathbf{r}} \mathbf{H} \bar{\bar{g}} \mathbf{S}_{\mathbf{r}},\end{aligned} \tag{5.1}$$

where the Zeeman term from the external magnetic field is included for the generality purpose.

Among all the static properties, the most remarkable one is the magnetization process. Despite being quasi-2D, the material sustains a $1/3$ magnetization plateau [Figure 5.1(b)] within a considerable range of applied in-plane magnetic field [80]. In strongly correlated electronic systems, there exist two types of magnetization plateaux. The first type covers examples like quantum spin ladders [81, 82] and the Shastry-Sutherland model [83], where the plateau states have no classical analogs. The plateau from $Ba_3CoSb_2O_9$ belongs to the second type, which is often referred to as "semi-classical" because the plateau state can be pictured with classical spins. In this case, two spins in each triangle are aligned along

the field with the third one being anti-parallel to them. This state will thus be referred as the up-up-down (UUD) state hereafter. Despite being regarded as "semi-classical", such a state shall not exist in the classical limit at zero temperature. And the interlayer coupling further destroys the picture. As is investigated on the 2D case, it has to be either stabilized by thermal and/or quantum fluctuations [84, 85, 86, 87, 88].

5.2.3 Spin dynamics in the zero-field case

Everything is by far consistent with the theoretical interpretations. A spin-wave picture seemed reasonable and intuitive here and the non-collinear magnetic structure is prone to magnon instability. As mentioned before, numerous studies have discussed about the moment reduction and spontaneous magnon decays. In the Heisenberg case, the system is proposed to have a significantly reduced moment, which is $\langle S\rangle \approx 0.205(15)$ from DMRG simulation [74] or $\langle S\rangle \approx 0.24974$ from $1/S^2$ spin-wave calculation [8]. This indicates quite strong quantum fluctuations.

However, within the same spin-wave framework, the easy-plane anisotropy Δ and the inter-layer coupling J_c contribute to bringing back the classical picture. In particular, it was carefully examined that the kinematic condition for magnon decay is broken for $\Delta \lesssim 0.92$ [7, 8]. Therefore, the spin dynamics of $Ba_3CoSb_2O_9$ was expected to be well described by this semi-classical approach.

The actual result turns out to be surprising. Figure 5.2(a),(b) presents the zero-field inelastic neutron scattering data at $T \sim 1.5$ K measured on CNCS, SNS, accompanied with the $1/S$ spin-wave calculation that was supposed to roughly match the bandwidth of the "acoustic" mode. The parameters in the Hamiltonian (Equation 5.1) used in different reports are not exactly the same. Approximately, J is around 1.7 meV with 10% inter-layer coupling ($J_c \sim 0.1J$) and 10% easy-plane anisotropy ($\Delta \sim 0.9$). The details of the spin-wave calculation will be covered in later sections with applied field to provide more generality. With the instrumental resolution and sample mosaic taken into account, the

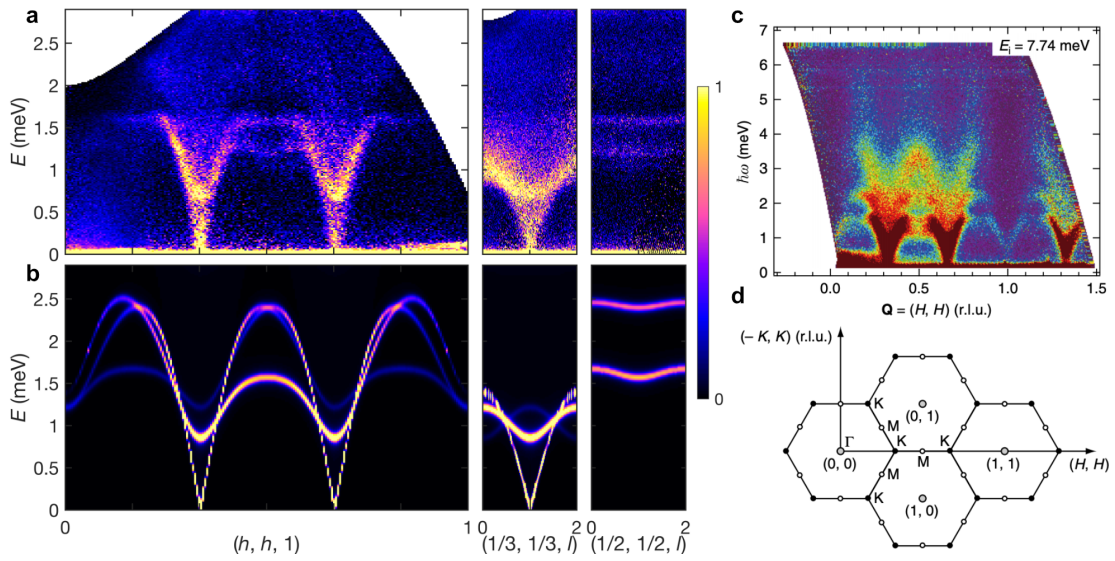

Figure 5.2: (a) Inelastic neutron scattering spectra based on the measured data in Ref. [89]. (c) The spin dynamical structure factor calculated from spin-wave theory with $1/S$ expansion using the parameters in Ref. [79]. (c) Inelastic neutron scattering result and (d) the reciprocal lattice mapping presented in Ref. [90].

measured dispersions are considered to be very sharp such that a quasi-particle picture is undoubted. The $1/S$ spin-wave calculation in Figure 5.2(b) indicates a strong bandwidth renormalization compared with the linear spin-wave approximation [89]. However, the broadening of the excitations above $E \sim 1.6$ meV is unpredicted and the local minima behavior at M point escapes the spin-wave description (see Figure 5.2(d) for reciprocal lattice mapping). Moreover, more recent results [90], as partially presented in Figure 5.2(c), indicates that there is an excitation mode around M points at $E \sim 3.5$ meV which is completely missed from the theory.

Although this will not deny the striking fact above, it is worth pointing out that the spectrum in Figure 5.2(c) is integrated over c^* axis. This introduces considerable artificial broadening due to the non-negligible dispersion along that direction so that it may somewhat be misleading.

5.2.4 Spin dynamics in the up-up-down (UUD) plateau phase

The zero-field magnetic excitations certainly bring up some unresolved puzzles. More fundamentally, it casts doubt on whether the effective spin Hamiltonian which has been taken for granted is able to represent the system without loss of any important information. To gain more insights, in-field inelastic neutron study becomes necessary. The best approach in theory to verifying a spin Hamiltonian is to conduct inelastic neutron scattering in the system's fully polarized phase. Because there exist no more quantum fluctuations in that ferromagnetic state and S_z becomes a good quantum number. Unfortunately, this is not feasible since the magnetic field ($H \approx 30$ T) to saturate the sample cannot be sustained.

Under this circumstance, the spin dynamics in the $1/3$ magnetization plateau becomes the most ideal properties one can probe. The spins are actually collinear in this UUD state, which is favored by quantum fluctuations. Meanwhile, the magnetic excitation spectra in the plateau phase are much less known in general mainly due to the difficulties in obtaining good single crystals and reaching the required experimental environments. Therefore, a careful investigation into this is rather pioneering and inspiring.

To achieve this experimentally, two advanced neutron spectrometers, MACS and FLEXX were utilized. Around one gram of sample was mounted on an aluminum holder and cooled down well below the Néel temperature for the measurement. On MACS, the experiment was conducted with 10.5 T magnetic field to cover a wide energy and momentum space [Figure 5.5(a)-(c)]. While on FLEXX, a more conventional triple-axis instrument, energy scans with constant momentum transfer were done to explore the field dependence [Figure 5.6(a)].

As for the theory part, a modified nonlinear spin-wave theory (NLSW) is performed. To explain why it is "modified", it is worth elaborating more on the challenge encountered in the theoretical approach. It comes from the fact that plateau states are not valid classical ground states at zero temperature. For instance, the UUD state in the 2D case is unstable unless the magnetic field H is fine-tuned to a single value $H = H_{\mathrm{sat}}/3$ where H_{sat} refers

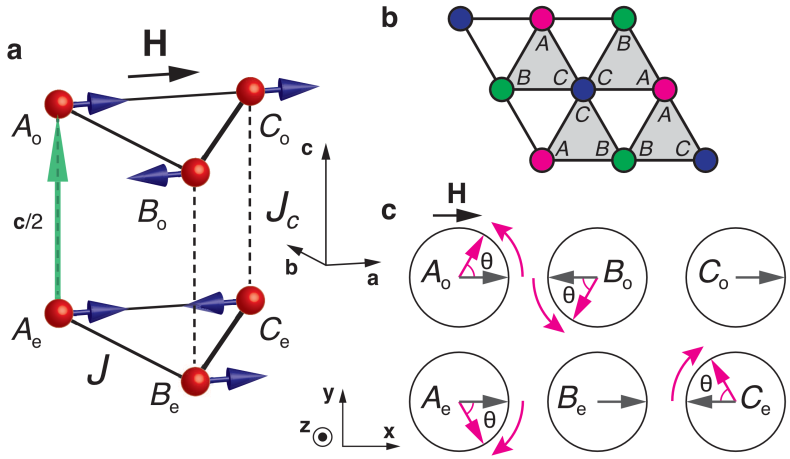

Figure 5.3: (a) Spin structure in the $1/3$ magnetization plateau (UUD) state. (b) Three-sublattice structure for each individual layer. (c) Illustration of how spins deform from UUD state.

to the saturation field. With the interlayer coupling introduced, such a state [Figure 5.3(a)] is further doomed to instability. Now one must recall that the spin-wave treatment builds on the assumption of a classically ordered moment and expands the Hamiltonian around a valid local minimum. In the case where $\mathcal{H}^{(1)}$ in Equation (1.6) does not vanish, the resulting $\mathcal{H}^{(2)}$ will not be positive definite to yield valid magnon dispersions. As a result, some special care is needed in addition to a naive spin-wave calculation.

Essentially, the trick which was originally applied to a distorted triangular lattice [91] is adapted here. The basic strategy is to make a "detour" in the parameter space with the additional $1/S$-axis quantifying the quantum effect [Figure 5.4(a)]. Instead of expanding the Hamiltonian from $S \to \infty$ for the actual model parameters (which ends up with instability), we start from the special point, $J_c = 0$, $H_{\text{red}} = 3JS$, and a given value of $0 \leq \Delta \leq 1$, that includes the UUD state in its classical ground state manifold.

Now that the field is applied within the ab plane, the Hamiltonian becomes

$$\begin{aligned}\mathcal{H} =& J \sum_{\langle \mathbf{r}\mathbf{r}' \rangle} \left(S^x_{\mathbf{r}} S^x_{\mathbf{r}'} + S^y_{\mathbf{r}} S^y_{\mathbf{r}'} + \Delta S^z_{\mathbf{r}} S^z_{\mathbf{r}'} \right) \\ &+ J_c \sum_{\mathbf{r}} \left(S^x_{\mathbf{r}} S^x_{\mathbf{r}+\frac{\mathbf{c}}{2}} + S^y_{\mathbf{r}} S^y_{\mathbf{r}+\frac{\mathbf{c}}{2}} + \Delta S^z_{\mathbf{r}} S^z_{\mathbf{r}+\frac{\mathbf{c}}{2}} \right) - g_{\perp} \mu_{\mathbf{B}} H \sum_{\mathbf{r}} S^x_{\mathbf{r}}.\end{aligned} \tag{5.2}$$

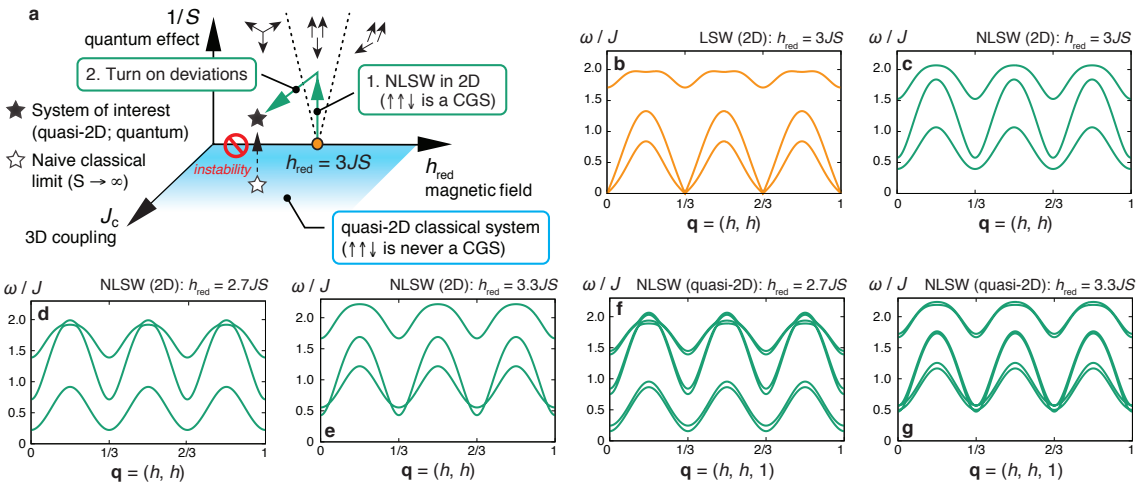

Figure 5.4: Scheme of nonlinear spin-wave theory (NLSW) for the $1/3$ plateau. (a) Illustration of the procedure. The filled and open star symbols represent the target quasi-2D quantum system and its naive classical limit ($S = \infty$), respectively. The spin configurations favored by quantum fluctuation in 2D are shown on the $J_c = 0$ plane. (b) LSW spectrum along the high-symmetry direction of the Brillouin zone evaluated for $S = 1/2$, $J_c = 0$, $\Delta = 0.85$ and $g_\perp \mu_{\mathbf{B}} H = 3JS$, where the UUD state is a classical ground state. (c)-(e) NLSW spectra for $J_c = 0$ and $\Delta = 0.85$ with various applied fields. (f)-(g) NLSW spectra for $J_c/J = 0.07$ and $\Delta = 0.85$ with various applied fields.

Assuming the spin structure in Figure 5.3, the transformation of the spin operators are

$$S^x_{\mathbf{r}} = \tilde{S}^z_{\mathbf{r}}, \quad S^y_{\mathbf{r}} = \tilde{S}^y_{\mathbf{r}}, \quad S^z_{\mathbf{r}} = -\tilde{S}^x_{\mathbf{r}}, \tag{5.3}$$

for $\mathbf{r} \in A_{\mathrm{e}}$, B_{e}, A_{o}, and C_{o} and

$$S^x_{\mathbf{r}} = -\tilde{S}^z_{\mathbf{r}}, \quad S^y_{\mathbf{r}} = \tilde{S}^y_{\mathbf{r}}, \quad S^z_{\mathbf{r}} = \tilde{S}^x_{\mathbf{r}}, \tag{5.4}$$

for $\mathbf{r} \in C_{\mathrm{e}}, B_{\mathrm{o}}$. Represented with the Holstein-Primakoff bosons, $a^{(\dagger)}_{\mu,\mathbf{r}}$, with $1 \le \mu \le 6$ the sublattice index for A_{e}, B_{e}, C_{e}, A_{o}, B_{o}, and C_{o} in this order, the spin operators become

$$\begin{aligned} \tilde{S}^z_{\mathbf{r}} &= S - a^\dagger_{\mu,\mathbf{r}} a_{\mu,\mathbf{r}}, \\ \tilde{S}^+_{\mathbf{r}} &= \tilde{S}^x_{\mathbf{r}} + i\tilde{S}^y_{\mathbf{r}} \approx \sqrt{2S}\left(1 - \frac{a^\dagger_{\mu,\mathbf{r}} a_{\mu,\mathbf{r}}}{4S}\right) a_{\mu,\mathbf{r}}, \end{aligned} \tag{5.5}$$

and $\tilde{S}^{-}_{\mathbf{r}} = \left(\tilde{S}^{+}_{\mathbf{r}}\right)^{\dagger}$ for $\mathbf{r} \in \mu$, truncating higher order terms irrelevant for the quartic interaction.

The Hartree-Fock averages of the quartic Hamiltonian $\left\langle \mathcal{H}^{(4)}_{\mathrm{2D}} \right\rangle_{\mathrm{HF}}$ are evaluated. This manages to open a gap of the magnon poles [Figure 5.4(c)]. As shown in Figure 5.4(d)-(e), the gap remains finite with the field shifted up and down by 10%. The gap persists even with the interlayer coupling introduced [Figure 5.4(f)-(g)], where the three dispersion branches are split into six.

Meanwhile, the reduced ordered moment also serves as a good indicator on the stability of the system. It can be confirmed from calculation that $\left|\delta \left\langle S^{x}_{\mu} \right\rangle\right| / S \lesssim 30\%$ throughout the local stability range of the plateau. Meanwhile, the staggered magnetization,

$$M_{\mathrm{UUD}} = \frac{1}{6}\left(\langle S^{x}_{A_{\mathrm{e}}}\rangle + \langle S^{x}_{B_{\mathrm{e}}}\rangle - \langle S^{x}_{C_{\mathrm{e}}}\rangle + \langle S^{x}_{A_{\mathrm{o}}}\rangle - \langle S^{x}_{B_{\mathrm{o}}}\rangle + \langle S^{x}_{C_{\mathrm{o}}}\rangle\right), \tag{5.6}$$

is almost field-independent [79].

Since the UUD state is a collinear state, the cubic term $\mathcal{H}^{(3)}$ of the spin-wave Hamiltonian vanishes, which eliminates the consideration of magnon decay processes within $1/S$-order correction. This makes it rather straightforward to calculate the transverse part of the dynamical structure factor $\mathcal{S}_{\perp}(\mathbf{q},\omega) \equiv \mathcal{S}_{\tilde{x}\tilde{x}} + \mathcal{S}_{\tilde{y}\tilde{y}}$ from the renormalized quadratic Hamiltonian. The longitudinal component $\mathcal{S}_{\parallel}(\mathbf{q},\omega)$ is intrinsically one order higher and usually neglected in linear spin-wave approximation. It is calculated at K and M points only because the involved numerical integration in such a non-Bravais lattice is prohibitively complex.

Figure 5.5(a)-(c) shows the excitation spectra of $Ba_3CoSb_2O_9$ in the UUD phase measured on MACS. To avoid any possible confusion, it is necessary to stress that the spectrum in Figure 5.5(a) is at $l = 2$ which is always gapped even without the quantum effect argument. The reason for showing this instead of that at $l = 1$ is because those data suffer from direct neutron beam due to the limit from the instrumental geometry. In contrast to the zero-field result, the excitation branch at M point becomes a saddle point now which is

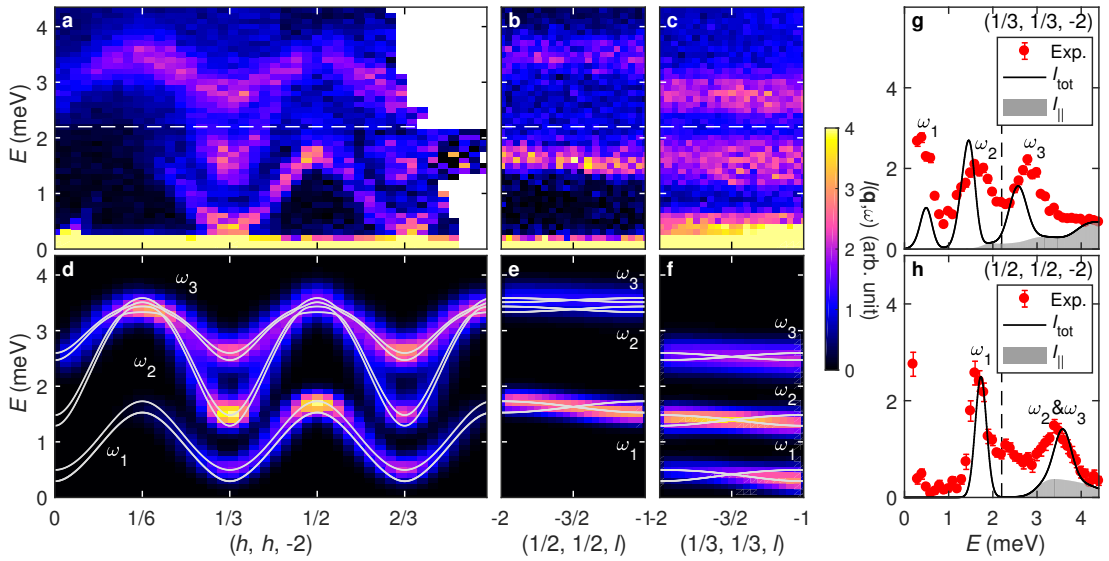

Figure 5.5: Excitation spectra in the UUD phase of $Ba_3CoSb_2O_9$. (a)-(c) Experimental scattering intensity at $\mu_0 H = 10.5$ T and $T = 0.5$ K. (d)-(f) Calculated transverse part of the scattering intensity, $I_\perp(\mathbf{q}, \omega)$, obtained by spin-wave theory for $J = 1.74$ meV, $\Delta = 0.85$, $J_c/J = 0.09$, and $g_\perp = 3.95$. The solid lines are magnon dispersions. (g)-(h) $\mathbf{Q}$-integrated energy dependence of the scattering intensity, compared with the experiment. The longitudinal contribution is plotted as a shared area. The dashed lines in (a)-(c) and (g)-(h) indicate the change of outgoing neutron energy $E_\mathrm{f} = 5$ meV (3 meV) above (below).

more consistent with a traditional spin-wave picture. It is also verified that the high-energy ($E \sim 3.5$ meV) excitation mode at M point does not appear in the plateau case. In addition to MACS data, energy scans with $\mathbf{q} = (1/3, 1/3, 1)$ were performed on FLEXX under various magnetic fields [Figure 5.6(a)].

Now comes the direct comparison between the experimental data and the numerical result. It turns out that the NLSW calculation agrees very well with the observed magnetic excitations. In order to get the best match, the following parameters of the Hamiltonian are selected: $J = 1.74$ meV, $\Delta = 0.85$, $J_c/J = 0.09$ and $g_\perp = 3.95$. Although some level of deviation exists, all the qualitative features are correctly captured [Figure 5.5]. Moreover, the resulted agreement on field dependence [Figure 5.6] further confirms the reliability of the theoretical model. The only issue that remains inconclusive is the gapped feature at $\mathbf{q} = (1/3, 1/3, 1)$ and $H = 10.5$ T. In other words, whether the lowest mode has an opened gap in this field is uncertain due to the limitation from the instrumental resolution.

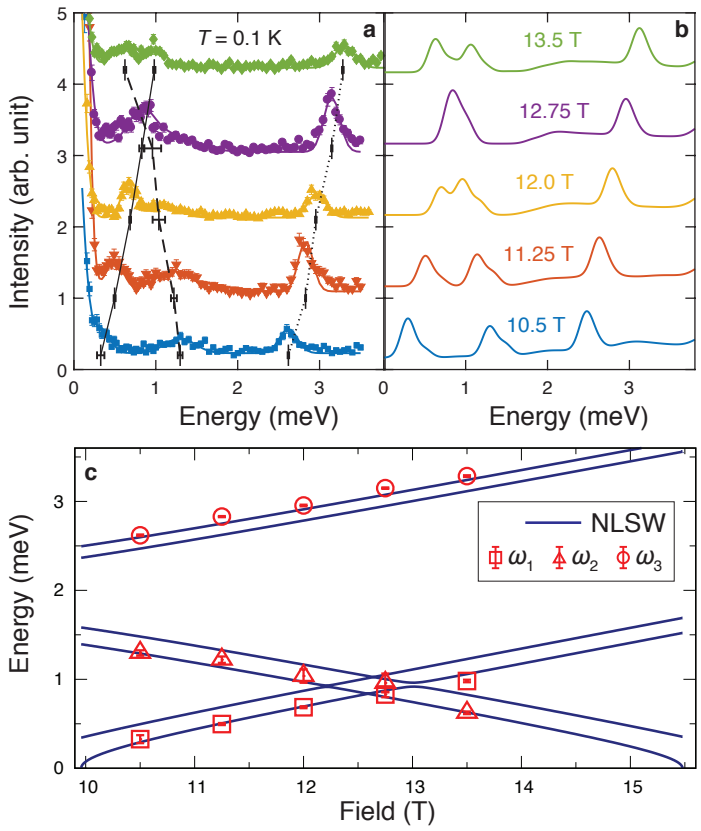

Figure 5.6: Field dependence of magnon poles ω_1-ω_3 at $\mathbf{q} = (1/3, 1/3, 1)$ in the UUD phase. (a) Constant-$\mathbf{q}$ scans for various magnetic field at $T = 0.1$ K. The solid-lines show the fits with Gaussian functions. The locations of the magnon peaks are indicated. (b) Simulation of the line-shape by NLSW theory of the same Hamiltonian parameters in Figure 5.5 convoluted with the assumed resolution 0.2 meV. (c) Comparison of the fitted magnon frequencies against the NLSW poles.

However, examining the energy scans with other fields [Figure 5.6], it is reasonable to believe in the existence of a small gap.

Overall, the work provides an excellent semiclassical model for the excitation spectrum of $Ba_3CoSb_2O_9$ in the $1/3$ magnetization plateau. The semiclassical nature of magnon excitations in this plateau phase is unequivocally confirmed despite that the fluctuation-induced nature of the static magnetic structure. Based on this, it is reasonable to believe the same treatment will be applicable to other 2D and quasi-2D realizations of fluctuation-induced plateaus, such as the $1/3$ plateau in the spin-$5/2$ material $RbFe(MoO_4)_2$ [92]. Meanwhile, it will also be worthwhile to examine the validity of this approach in quasi-

1D materials such as Cs_2CuBr_4 [93], where quantum fluctuations are expected to be more profound.

Back to the system itself, the question raised from the system's zero-field spin dynamics gets partially answered here. Rather than having extra terms in the spin Hamiltonian, the system certainly fits into the current model in the plateau phase. This in turn implies that the zero-field behavior is dominated by intrinsic quantum mechanical effects that escape a semiclassical spin-wave description. One may find the M-point excitation in zero-field particularly analogous to the $(\pi, 0)$ wave-vector anomaly observed in those aforementioned spin-1/2 square-lattice Heisenberg antiferromagnets [10, 11, 12, 13, 14].

5.2.5 Spin dynamics in the canted "umbrella" phase

Now that a reliable spin Hamiltonian is obtained from the UUD state investigation, it is worthwhile to know whether it can work elsewhere in the phase diagram, ideally within the spin-wave picture. In particular, it would be very beneficial to see whether any signatures of magnon decays could be detected.

It has been mentioned that in such a system with the easy-plane anisotropy parameter $\Delta = 0.85$, the kinematic conditions for one-magnon to two-magnon decay are not met and no decay processes will be allowed up to the $\mathcal{O}(1/S)$ order expansion. However, the magnetic field may change the situation. Taking the square-lattice antiferromagnet as an example, although the system's zero-field Néel order is collinear and eliminates the three-magnon diagrams, the out-of-plane magnetic field is able to introduce an overlap between the one-magnon and two-magnon density of states at $H \sim 0.75 H_{\mathrm{sat}}$ which leads to finite magnon decay rate [9, 94]. Moreover, the recent research on the spin-half triangular lattice antiferromagnet in the 2D limit also proposes a field induced decay scenario [95]. The interlayer coupling J_c was not considered in that study. Albeit J_c is not expected to compeltely alter the picture from intuition, it definitely requires some calculation to be able to make a rigorous claim from the theoretical point of view. Meanwhile, a careful examination

on $Ba_3CoSb_2O_9$ with neutron scattering experiments also becomes more meaningful.

Figure 5.7 shows the visualization of the "umbrella" state as well as where it resides in the magnetization phase diagram. The canting angle is denoted as θ here. Because such a state is continuously transformed from the zero-field magnetic structure, the spin-wave calculation that will be presented here is directly applicable to the zero-field case by turning off the magnetic field. For exactly this reason, the calculation is intended to be gone through here in a very detailed fashion.

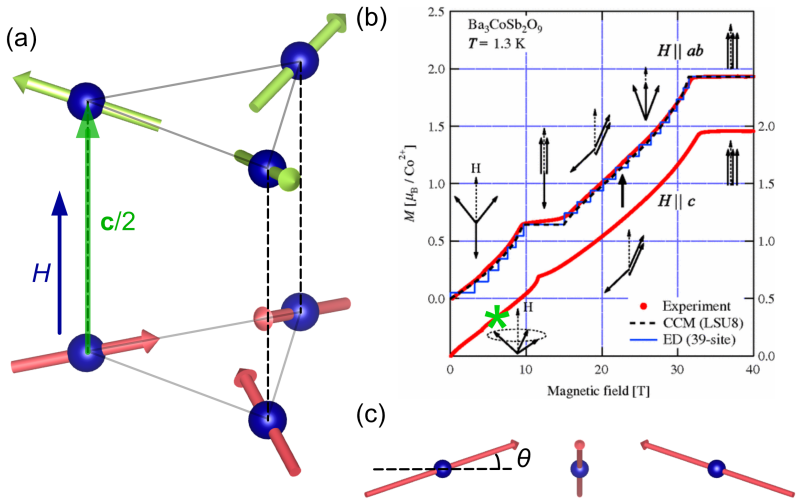

Figure 5.7: (a) A crystallographic view of the canted "umbrella" state. (b) The magnetization curves with the green asterisk indicating where the state it. (c) Illustration of the canting angle.

With the magnetic field applied along c-axis, the Hamiltonian now writes

$$\begin{aligned}\mathcal{H} =& J\sum_{\langle \mathbf{r}\mathbf{r}'\rangle}\left(S^x_{\mathbf{r}}S^x_{\mathbf{r}'}+S^y_{\mathbf{r}}S^y_{\mathbf{r}'}+\Delta S^z_{\mathbf{r}}S^z_{\mathbf{r}'}\right) \\ &+J_c\sum_{\mathbf{r}}\left(S^x_{\mathbf{r}}S^x_{\mathbf{r}+\frac{\mathbf{c}}{2}}+S^y_{\mathbf{r}}S^y_{\mathbf{r}+\frac{\mathbf{c}}{2}}+\Delta S^z_{\mathbf{r}}S^z_{\mathbf{r}+\frac{\mathbf{c}}{2}}\right)-g_{\parallel}\mu_{\mathbf{B}}H\sum_{\mathbf{r}}S^z_{\mathbf{r}}.\end{aligned} \tag{5.7}$$

The spin Hamiltonian remains the same as that of previous sections. Since the out-of-plane magnetic field acts along the c-axis, perpendicular to the easy-plane, the system preserves the 120° type symmetry but all spins now are canted toward the field direction. Therefore, the ground state spin structures can still be described by a single magnetic wave

vector $\mathbf{Q} = (1/3, 1/3, 1/2)$ (in hkl, and $(2/3, 0, 1/2)$ in the cartesian coordinates used in this document).

The classical energy per spin is

$$E_{\rm cl}/N = 3JS^2\left(\Delta\sin^2\theta - \frac{1}{2}\cos^2\theta\right) + J_cS^2\left(\Delta\sin^2\theta - \cos^2\theta\right) - g\mu_{\rm B}HS\sin\theta. \quad (5.8)$$

It is straightforward to get the canting angle by minimizing the above equation, which gives

$$\sin\theta = \frac{H}{H_{\rm sat}}, \quad (5.9)$$

where $H_{\rm sat}$ is the saturation field satisfying

$$H_{\rm sat}/g\mu_{\rm B} = 6JS\left(\Delta + \frac{1}{2}\right) + 2J_cS\left(\Delta + 1\right). \quad (5.10)$$

Rewriting the applied field H using above two equations is able to eliminate the field terms in the Hamiltonian. This will end up significantly simplifying the expressions, as shall be seen later.

The transformation of spin operators from the global coordinates to the local ones can be achieved by two steps of rotation,

$$\mathbf{S}_i^0 = \mathbf{R}_\mathbf{Q}\mathbf{R}_\theta\mathbf{S}_i, \quad (5.11)$$

where the matrix $\mathbf{R}_\mathbf{Q}$ does the in-plane rotation,

$$\mathbf{R}_\mathbf{Q} = \begin{pmatrix} \cos\varphi_i & -\sin\varphi_i & 0 \\ \sin\varphi_i & \cos\varphi_i & 0 \\ 0 & 0 & 1 \end{pmatrix}, \quad (5.12)$$

where $\varphi_i \equiv \mathbf{Q} \cdot \mathbf{r}_i$. The matrix $\mathbf{R}_\theta$ is related to the canting angle,

$$\mathbf{R}_\theta = \begin{pmatrix} \sin\theta & 0 & \cos\theta \\ 0 & 1 & 0 \\ -\cos\theta & 0 & \sin\theta \end{pmatrix}. \tag{5.13}$$

Overall, the transformation is as the following,

$$S_i^{x_0} = S_i^x \sin\theta\cos\varphi_i - S_i^y \sin\varphi_i + S_i^z \cos\theta\cos\varphi_i, \tag{5.14}$$

$$S_i^{y_0} = S_i^x \sin\theta\sin\varphi_i + S_i^y \cos\varphi_i + S_i^z \cos\theta\sin\varphi_i, \tag{5.15}$$

$$S_i^{z_0} = -S_i^x \cos\theta + S_i^z \sin\theta. \tag{5.16}$$

It is important to be aware that the above transformation assumes one of the two possible chiralities which used to identical in zero-field but are now distinct. The chirality here, to be better understood, describes in which direction the "umbrella" rotates when the structure propagates in real space. Essentially, this breaks the inversion symmetry in the reciprocal space and splits the K point into two kinds. However, as one shall see later, those two chiralities should be equally present in actual experiments.

The general Hamiltonian, after the Holstein-Primakoff transformation, can again be expanded as Equation (1.6). Before then, it is as always beneficial to separate it into the

odd and even parts,

$$\begin{aligned}\mathcal{H}_{\text{even}} =& J\sum_{\langle ij\rangle} S_i^x S_j^x \left(\sin^2\theta\cos\varphi_{ij} + \Delta\cos^2\theta\right) + S_i^y S_j^y \cos\varphi_{ij} \\ &+ S_i^z S_j^z \left(\cos^2\theta\cos\varphi_{ij} + \Delta\sin^2\theta\right) \\ &+ \left(S_i^x S_j^y - S_i^y S_j^x\right)\sin\varphi_{ij}\sin\theta \\ &+ J_c\sum_{\langle ii'\rangle} S_i^x S_{i'}^x \left(\sin^2\theta\cos\pi + \Delta\cos^2\theta\right) + S_i^y S_{i'}^y \cos\pi \\ &+ S_i^z S_{i'}^z \left(\cos^2\theta\cos\pi + \Delta\sin^2\theta\right) \\ &- g\mu_{\text{B}} H\sum_i S_i^z \sin\theta, \end{aligned} \tag{5.17}$$

$$\begin{aligned}\mathcal{H}_{\text{odd}} =& J\sum_{\langle ij\rangle} \left(S_i^x S_j^z + S_i^z S_j^x\right)\sin\theta\cos\theta\left(-\Delta + \cos\varphi_{ij}\right) + \left(S_i^z S_j^y - S_i^y S_j^z\right)\cos\theta\sin\varphi_{ij} \\ &+ J_c\sum_{\langle ii'\rangle} \left(S_i^x S_{i'}^z + S_i^z S_{i'}^x\right)\sin\theta\cos\theta\left(-\Delta + \cos\pi\right) \\ &+ g\mu_{\text{B}} H\sum_i S_i^x \cos\theta, \end{aligned} \tag{5.18}$$

where $\varphi_{ij} \equiv \varphi_i - \varphi_j = \pm 120^\circ$.

This gives the harmonic Hamiltonian

$$\mathcal{H}^{(2)} = 3JS\sum_{\mathbf{k}} \left(A_{\mathbf{k}} + C_{\mathbf{k}}\right) a_{\mathbf{k}}^\dagger a_{\mathbf{k}} - \frac{B_{\mathbf{k}}}{2}(a_{\mathbf{k}}^\dagger a_{-\mathbf{k}}^\dagger + \text{h.c.}), \tag{5.19}$$

with the parameters

$$A_{\mathbf{k}} = 1 + \frac{2\alpha}{3} + \gamma_{\mathbf{k}}\left[\left(\Delta + \frac{1}{2}\right)\cos^2\theta - 1\right] + \frac{\alpha}{3}\beta_{\mathbf{k}}\left[(\Delta+1)\cos^2\theta - 2\right], \tag{5.20}$$

$$B_{\mathbf{k}} = -\gamma_{\mathbf{k}}\left(\Delta + \frac{1}{2}\right)\cos^2\theta - \frac{\alpha}{3}\beta_{\mathbf{k}}\left(\Delta+1\right)\cos^2\theta, \tag{5.21}$$

$$C_{\mathbf{k}} = \sqrt{3}\bar{\gamma}_{\mathbf{k}}\sin\theta. \tag{5.22}$$

$\gamma_{\mathbf{k}}$ and $\beta_{\mathbf{k}}$ have already been introduced before, and $\bar{\gamma}_{\mathbf{k}}$, an odd function of $\mathbf{k}$, reads

$$\bar{\gamma}_{\mathbf{k}} = \frac{1}{3}\left(\sin 2\pi k_x - 2\sin \pi k_x \cos \sqrt{3}\pi k_y\right). \tag{5.23}$$

This indicates $C_{-\mathbf{k}} = -C_{\mathbf{k}}$, which makes the term insensitive to the Bogolyubov transformation. As a result, the spin-wave dispersion is

$$\varepsilon_{\mathbf{k}} = 3JS\omega_{\mathbf{k}}, \tag{5.24}$$

where

$$\omega_{\mathbf{k}} = \sqrt{A_{\mathbf{k}}^2 - B_{\mathbf{k}}^2} + C_{\mathbf{k}}, \tag{5.25}$$

and the Bogolyubov coefficients are simply obtained from

$$\begin{aligned} 2u_{\mathbf{k}}v_{\mathbf{k}} &= \frac{B_{\mathbf{k}}}{\sqrt{A_{\mathbf{k}}^2 - B_{\mathbf{k}}^2}}, \\ u_{\mathbf{k}}^2 + v_{\mathbf{k}}^2 &= \frac{A_{\mathbf{k}}}{\sqrt{A_{\mathbf{k}}^2 - B_{\mathbf{k}}^2}}. \end{aligned} \tag{5.26}$$

Note that now the inversion symmetry is broken by the field-induced chirality, the spin-wave dispersion is asymmetric, $\varepsilon_{\mathbf{k}} \neq \varepsilon_{-\mathbf{k}}$.

The dynamical structure factors at the order of linear spin-wave approximation are,

$$\begin{aligned} \mathcal{S}^{x_0x_0}(\mathbf{q},\omega) &= \frac{1}{4} \\ &\left[\mathcal{S}^{yy}_{\mathbf{q}_+} + \mathcal{S}^{yy}_{\mathbf{q}_-} - 2i\sin\theta\left(\mathcal{S}^{xy}_{\mathbf{q}_+} - \mathcal{S}^{xy}_{\mathbf{q}_-}\right) + \sin^2\theta\left(\mathcal{S}^{xx}_{\mathbf{q}_+} + \mathcal{S}^{xx}_{\mathbf{q}_-}\right) + \cos^2\theta\left(\mathcal{S}^{zz}_{\mathbf{q}_+} + \mathcal{S}^{zz}_{\mathbf{q}_-}\right)\right], \\ \mathcal{S}^{y_0y_0}(\mathbf{q},\omega) &= \mathcal{S}^{x_0x_0}(\mathbf{q},\omega), \\ \mathcal{S}^{z_0z_0}(\mathbf{q},\omega) &= \cos^2\theta\mathcal{S}^{xx}_{\mathbf{q}} + \sin^2\theta\mathcal{S}^{zz}_{\mathbf{q}}, \end{aligned} \tag{5.27}$$

where $\mathbf{q}_\pm \equiv \mathbf{q} \pm \mathbf{Q}$ and

$$\begin{aligned}
\mathcal{S}^{xx}(\mathbf{q},\omega) &= \frac{S}{2}\left(u_{\mathbf{q}}+v_{\mathbf{q}}\right)^2\delta(\omega-\omega_{\mathbf{q}}),\\
\mathcal{S}^{yy}(\mathbf{q},\omega) &= \frac{S}{2}\left(u_{\mathbf{q}}-v_{\mathbf{q}}\right)^2\delta(\omega-\omega_{\mathbf{q}}),\\
\mathcal{S}^{xy}(\mathbf{q},\omega) &= i\frac{S}{2}(u_{\mathbf{q}}+v_{\mathbf{q}})\left(u_{\mathbf{q}}-v_{\mathbf{q}}\right)\delta(\omega-\omega_{\mathbf{q}}) = i\frac{S}{2}\delta(\omega-\omega_{\mathbf{q}}),
\end{aligned} \tag{5.28}$$

where the last equation above uses the fact that $u_{\mathbf{q}}^2 - v_{\mathbf{q}}^2 = 1$, and $\mathcal{S}^{zz}$ which at this level only yields the magnetic Bragg peaks is omitted.

The first step to go beyond the non-interacting magnons is calculating the Hartree-Fock corrections. This is a mean-field treatment of magnon interactions by decoupling those higher order terms (cubic, quartic, etc.) and integrating over the reciprocal space to get the averages. These averages are denoted as the following,

$$\rho = \left\langle a_i^\dagger a_i \right\rangle = \sum_{\mathbf{k}} v_{\mathbf{k}}^2, \tag{5.29}$$

$$\xi_1 = \left\langle a_i^\dagger a_j \right\rangle = \sum_{\mathbf{k}} v_{\mathbf{k}}^2\gamma_{\mathbf{k}}, \tag{5.30}$$

$$\xi_2 = \left\langle a_i^\dagger a_{i'} \right\rangle = \sum_{\mathbf{k}} v_{\mathbf{k}}^2\beta_{\mathbf{k}}, \tag{5.31}$$

$$\delta = \langle a_i a_i \rangle = \sum_{\mathbf{k}} u_{\mathbf{k}} v_{\mathbf{k}}, \tag{5.32}$$

$$\zeta_1 = \langle a_i a_j \rangle = \sum_{\mathbf{k}} u_{\mathbf{k}} v_{\mathbf{k}}\gamma_{\mathbf{k}}, \tag{5.33}$$

$$\zeta_2 = \langle a_i a_{i'} \rangle = \sum_{\mathbf{k}} u_{\mathbf{k}} v_{\mathbf{k}}\beta_{\mathbf{k}}, \tag{5.34}$$

where $\{i,j\}$ and $\{i,i'\}$ implicitly refer to the nearest-neighbor and inter-layer sites, respectively. $\mathbf{k}$ is summed over the first Brillouin zone.

The decoupled cubic terms $\mathcal{H}_{\mathrm{HF}}^{(3)}$ in general make a correction to the ground state. In this context, it leads to the so-called angle renormalization. In the zero-field case, however, it has been verified there is no Hartree-Fock correction from the cubic terms.

Specifically, $\mathcal{H}^{(3)}_{\rm HF}$ will give a correction to the linear term $\mathcal{H}^{(1)}$ which vanishes in the classical ground state with the canting angle $\theta = \arcsin(H/H_{\rm sat})$. This new equilibrium at the order of $\mathcal{O}(1/S)$ requires

$$\mathcal{H}^{(1)} + \mathcal{H}^{(3)}_{\rm HF} = (V_1 + \delta V_1) \sum_i \left(a_i + a_i^\dagger \right), \tag{5.35}$$

where

$$V_1 = \sqrt{\frac{S}{2}} \cos\theta \left[g\mu_{\rm B} H - 6JS \left(\Delta + \frac{1}{2} \right) - 2J_c S \left(\Delta + 1 \right) \right], \tag{5.36}$$

$$\delta V_1 = \sqrt{\frac{S}{2}} \cos\theta \left[g\mu_{\rm B} H - 6J \left(\Delta + \frac{1}{2} \right) \left(\xi_1 + \zeta_1 + \rho \right) - 2J_c \left(\Delta + 1 \right) \left(\xi_2 + \zeta_2 + \rho \right) \right]. \tag{5.37}$$

Solving $V_1 + \delta V_1$ gives a new canting angle

$$\sin\theta = \frac{g\mu_{\rm B} H}{H'_{\rm sat}}, \tag{5.38}$$

$$H'_{\rm sat}/g\mu_{\rm B} = 6JS \left(\Delta + \frac{1}{2} \right) \left(1 - \frac{\xi_1 + \zeta_1 + \rho}{S} \right) - 2J_c S \left(\Delta + 1 \right) \left(1 - \frac{\xi_2 + \zeta_2 + \rho}{S} \right), \tag{5.39}$$

where $H'_{\rm sat}$ is a virtual saturation field considering the $1/S$ correction. To distinguish two different angles we denote the original one by θ_0 hereafter, and $\delta\theta \equiv \theta - \theta_0$ corrects the quadratic term $\mathcal{H}^{(2)}$ by

$$\delta\mathcal{H}^{(3)}_2 = \frac{\partial \mathcal{H}^{(2)}}{\partial \theta} \delta\theta, \tag{5.40}$$

which can be written as

$$\delta\mathcal{H}^{(3)}_2 = 3JS \sum_{\mathbf{k}} \left(\delta A^{(3)}_{\mathbf{k}} + \delta C^{(3)}_{\mathbf{k}} \right) a^\dagger_{\mathbf{k}} a_{\mathbf{k}} - \frac{\delta B^{(3)}_{\mathbf{k}}}{2} \left(a^\dagger_{\mathbf{k}} a^\dagger_{-\mathbf{k}} + \text{h.c.} \right), \tag{5.41}$$

where

$$\delta A_{\mathbf{k}}^{(3)} = -\left[\gamma_{\mathbf{k}}\left(\Delta+\frac{1}{2}\right)+\frac{\alpha}{3}\beta_{\mathbf{k}}\left(\Delta+1\right)\right]\sin 2\theta\cdot\delta\theta, \tag{5.42}$$

$$\delta B_{\mathbf{k}}^{(3)} = -\delta A_{\mathbf{k}}^{(3)}, \tag{5.43}$$

$$\delta C_{\mathbf{k}}^{(3)} = \sqrt{3}\bar{\gamma}_{\mathbf{k}}\cos\theta\cdot\delta\theta. \tag{5.44}$$

Likewise, this gives the correction to the one-magnon dispersion

$$\varepsilon_{\mathbf{k}}^{(3)} = 3JS\left(\frac{A_{\mathbf{k}}\delta A_{\mathbf{k}}^{(3)}-B_{\mathbf{k}}\delta B_{\mathbf{k}}^{(3)}}{A_{\mathbf{k}}^2-B_{\mathbf{k}}^2}+\delta C_{\mathbf{k}}^{(3)}\right). \tag{5.45}$$

The quartic terms will correct the quadratic terms,

$$\delta\mathcal{H}_{\mathrm{HF}}^{(4)} = 3J\sum_{\mathbf{k}}\left(\delta A_{\mathbf{k}}^{(4)}+\delta C_{\mathbf{k}}^{(4)}\right)a_{\mathbf{k}}^{\dagger}a_{\mathbf{k}}-\frac{\delta B_{\mathbf{k}}^{(4)}}{2}\left(a_{\mathbf{k}}^{\dagger}a_{-\mathbf{k}}^{\dagger}+\mathrm{h.c.}\right), \tag{5.46}$$

where

$$\begin{aligned}\delta A_{\mathbf{k}}^{(4)} =& -\left[\zeta_1\left(\Delta+\frac{1}{2}\right)+\xi_1\left(\Delta-\frac{1}{2}\right)+\rho\right]+\sin^2\theta\left(\Delta+\frac{1}{2}\right)\left(2\rho+\zeta_1+\xi_1\right) \\ &-\gamma_{\mathbf{k}}\left[\xi_1+\rho\left(\Delta-\frac{1}{2}\right)+\frac{\delta}{2}\left(\Delta+\frac{1}{2}\right)-\sin^2\theta\left(\Delta+\frac{1}{2}\right)\left(2\xi_1+\frac{\delta}{2}+\rho\right)\right] \\ &-\frac{\alpha}{3}\left[\zeta_2\left(\Delta+1\right)+\xi_2\left(\Delta-1\right)+2\rho-\sin^2\theta\left(\Delta+1\right)\left(2\rho+\zeta_2+\xi_2\right)\right] \\ &-\frac{\alpha}{3}\beta_{\mathbf{k}}\left[2\xi_2+\rho\left(\Delta-1\right)+\frac{\delta}{2}\left(\Delta+1\right)-\sin^2\theta\left(\Delta+1\right)\left(2\xi_2+\frac{\delta}{2}+\rho\right)\right],\end{aligned} \tag{5.47}$$

$$\begin{aligned}\delta B_{\mathbf{k}}^{(4)} =& \frac{1}{2}\left[\xi_1\left(\Delta+\frac{1}{2}\right)+\zeta_1\left(\Delta-\frac{1}{2}\right)\right]-\frac{\sin^2\theta}{2}\left(\Delta+\frac{1}{2}\right)\left(\zeta_1+\xi_1\right) \\ &+\gamma_{\mathbf{k}}\left[\zeta_1+\rho\left(\Delta+\frac{1}{2}\right)+\frac{\delta}{2}\left(\Delta-\frac{1}{2}\right)-\sin^2\theta\left(\Delta+\frac{1}{2}\right)\left(\rho+2\zeta_1+\frac{\delta}{2}\right)\right], \\ &+\frac{\alpha}{6}\left[\xi_2\left(\Delta+1\right)+\zeta_2\left(\Delta-1\right)-\sin^2\theta\left(\Delta+1\right)\left(\zeta_2+\xi_2\right)\right] \\ &+\frac{\alpha}{3}\beta_{\mathbf{k}}\left[2\zeta_2+\rho\left(\Delta+1\right)+\frac{\delta}{2}\left(\Delta-1\right)-\sin^2\theta\left(\Delta+1\right)\left(\rho+2\zeta_2+\frac{\delta}{2}\right)\right],\end{aligned} \tag{5.48}$$

$$\delta C_{\mathbf{k}}^{(4)} = -\sqrt{3}\rho\bar{\gamma}_{\mathbf{k}}\sin\theta, \tag{5.49}$$

and this leads to the correction to the one-magnon energy spectrum

$$\varepsilon_{\mathbf{k}}^{(4)} = 3J\left(\frac{A_{\mathbf{k}}\delta A_{\mathbf{k}}^{(4)} - B_{\mathbf{k}}\delta B_{\mathbf{k}}^{(4)}}{A_{\mathbf{k}}^2 - B_{\mathbf{k}}^2} + \delta C_{\mathbf{k}}^{(4)}\right). \tag{5.50}$$

The anti-symmetric term $C_{\mathbf{k}}$ in $\mathcal{H}^{(2)}$ is peculiar to the in-field case and vanishes in zero field.

Overall the Hartree-Fock correction to the one-magnon spectrum is just $\Sigma_{\mathrm{HF}}(\mathbf{k}) = \varepsilon_{\mathbf{k}}^{(4)} + \varepsilon_{\mathbf{k}}^{(3)}$.

Explicitly writing down the cubic Hamiltonian, one obtains

$$\begin{aligned}\mathcal{H}^{(3)} &= J\sqrt{\frac{S}{2}}\sum_{\langle ij\rangle}\sin 2\theta\left(\Delta+\frac{1}{2}\right)\left(a_i^\dagger + a_i\right)a_j^\dagger a_j - 2i\sin\varphi_{ij}a_i^\dagger a_i\left(a_j^\dagger - a_j\right), \\ &= J_c\sqrt{\frac{S}{2}}\sum_{\langle ii'\rangle}\sin 2\theta\left(\Delta+1\right)\left(a_i^\dagger + a_i\right)a_{i'}^\dagger a_{i'}.\end{aligned} \tag{5.51}$$

Note that the interlayer coupling does not contribute here due to the collinear spin configuration along c-axis. After the Fourier and Bogolubov transformation, the cubic Hamiltonian becomes

$$\begin{aligned}\mathcal{H}^{(3)} = &\frac{3J}{2!}\sqrt{\frac{S}{2}}\sum_{\mathbf{k},\mathbf{q}}\left(\Gamma_1(\mathbf{q},\mathbf{k}-\mathbf{q};\mathbf{k})b_{\mathbf{q}}^\dagger b_{\mathbf{k}-\mathbf{q}}^\dagger b_{\mathbf{k}} + \mathrm{h.c.}\right) \\ &+ \frac{3J}{3!}\sqrt{\frac{S}{2}}\sum_{\mathbf{k},\mathbf{q}}\left(\Gamma_2(\mathbf{q},-\mathbf{k}-\mathbf{q};\mathbf{k})b_{\mathbf{q}}^\dagger b_{-\mathbf{k}-\mathbf{q}}^\dagger b_{\mathbf{k}}^\dagger + \mathrm{h.c.}\right),\end{aligned} \tag{5.52}$$

where $\Gamma_{1(2)}$ are the decay (source) vertices which are introduced earlier in Figure 1.2. The

explicit expressions for them are

$$\begin{aligned}\Gamma_1(\mathbf{q},\mathbf{k}-\mathbf{q};\mathbf{k}) =& F_{\mathbf{q}}(u_{\mathbf{q}}+v_{\mathbf{q}})(u_{\mathbf{k}-\mathbf{q}}u_{\mathbf{k}}+v_{\mathbf{k}-\mathbf{q}}v_{\mathbf{k}}) \\ &+ F_{\mathbf{k}-\mathbf{q}}(u_{\mathbf{k}-\mathbf{q}}+v_{\mathbf{k}-\mathbf{q}})(u_{\mathbf{q}}u_{\mathbf{k}}+v_{\mathbf{q}}v_{\mathbf{k}}) \\ &+ F_{\mathbf{k}}(u_{\mathbf{k}}+v_{\mathbf{k}})(u_{\mathbf{q}}v_{\mathbf{k}-\mathbf{q}}+v_{\mathbf{q}}u_{\mathbf{k}-\mathbf{q}}) \\ &+ \bar{F}_{\mathbf{q}}(u_{\mathbf{q}}-v_{\mathbf{q}})(u_{\mathbf{k}-\mathbf{q}}u_{\mathbf{k}}+v_{\mathbf{k}-\mathbf{q}}v_{\mathbf{k}}) \\ &+ \bar{F}_{\mathbf{k}-\mathbf{q}}(u_{\mathbf{k}-\mathbf{q}}-v_{\mathbf{k}-\mathbf{q}})(u_{\mathbf{q}}u_{\mathbf{k}}+v_{\mathbf{q}}v_{\mathbf{k}}) \\ &+ \bar{F}_{\mathbf{k}}(u_{\mathbf{k}}-v_{\mathbf{k}})(u_{\mathbf{q}}v_{\mathbf{k}-\mathbf{q}}+v_{\mathbf{q}}u_{\mathbf{k}-\mathbf{q}}),\end{aligned} \tag{5.53}$$

$$\begin{aligned}\Gamma_2(\mathbf{q},-\mathbf{k}-\mathbf{q},\mathbf{k}) =& \bar{F}_{\mathbf{q}}(u_{\mathbf{q}}-v_{\mathbf{q}})(u_{-\mathbf{k}-\mathbf{q}}v_{\mathbf{k}}+v_{-\mathbf{k}-\mathbf{q}}u_{\mathbf{k}}) \\ &+ \bar{F}_{-\mathbf{k}-\mathbf{q}}(u_{-\mathbf{k}-\mathbf{q}}-v_{-\mathbf{k}-\mathbf{q}})(u_{\mathbf{q}}v_{\mathbf{k}}+v_{\mathbf{q}}u_{\mathbf{k}}) \\ &+ \bar{F}_{\mathbf{k}}(u_{\mathbf{k}}-v_{\mathbf{k}})(u_{\mathbf{q}}v_{-\mathbf{k}-\mathbf{q}}+v_{\mathbf{q}}u_{-\mathbf{k}-\mathbf{q}}) \\ &+ \bar{F}_{\mathbf{q}}(u_{\mathbf{q}}-v_{\mathbf{q}})(u_{-\mathbf{k}-\mathbf{q}}v_{\mathbf{k}}+v_{-\mathbf{k}-\mathbf{q}}u_{\mathbf{k}}) \\ &+ \bar{F}_{-\mathbf{k}-\mathbf{q}}(u_{-\mathbf{k}-\mathbf{q}}-v_{-\mathbf{k}-\mathbf{q}})(u_{\mathbf{q}}v_{\mathbf{k}}+v_{\mathbf{q}}u_{\mathbf{k}}) \\ &+ \bar{F}_{\mathbf{k}}(u_{\mathbf{k}}-v_{\mathbf{k}})(u_{\mathbf{q}}v_{-\mathbf{k}-\mathbf{q}}+v_{\mathbf{q}}u_{-\mathbf{k}-\mathbf{q}}),\end{aligned} \tag{5.55}$$

where

$$F_{\mathbf{k}} = \left[\gamma_{\mathbf{k}}\left(\Delta+\frac{1}{2}\right)+\frac{\alpha}{3}\beta_{\mathbf{k}}\left(\Delta+1\right)\right]\sin 2\theta, \tag{5.56}$$

$$\bar{F}_{\mathbf{k}} = -\sqrt{3}\bar{\gamma}_{\mathbf{k}}\cos\theta. \tag{5.57}$$

Through standard diagrammatic techniques, the leading $1/S$ magnon self-energies are found to be

$$\Sigma_{11}^{(a)}(\mathbf{k},\varepsilon) = \frac{9J^2S}{4}\sum_{\mathbf{q}}\frac{\left|\Gamma_1(\mathbf{q},\mathbf{k}-\mathbf{q};\mathbf{k})\right|^2}{\varepsilon-\varepsilon_{\mathbf{q}}-\varepsilon_{\mathbf{k}-\mathbf{q}}+i0_+}, \tag{5.58}$$

$$\Sigma_{11}^{(b)}(\mathbf{k},\varepsilon) = -\frac{9J^2S}{4}\sum_{\mathbf{q}}\frac{\left|\Gamma_2(\mathbf{q},-\mathbf{k}-\mathbf{q},\mathbf{k})\right|^2}{\varepsilon+\varepsilon_{\mathbf{q}}+\varepsilon_{-\mathbf{k}-\mathbf{q}}-i0_+}, \tag{5.59}$$

which correspond to the one-loop decay and source diagrams respectively [Figure 1.2].

The imaginary part of the decay-related self-energy, $\mathrm{Im}\Sigma_{11}^{(a)}(\mathbf{k}, \varepsilon_{\mathbf{k}})$, yields the on-shell two-magnon decay rate. For the zero-field case with the easy-plane anisotropy $\Delta < 0.92$, the magnon decay is suppressed due to the unsatisfied kinematic condition. This is to change when the external magnetic field is applied, which competes with the anisotropy and opens the decay channel at an experimentally accessible magnitude.

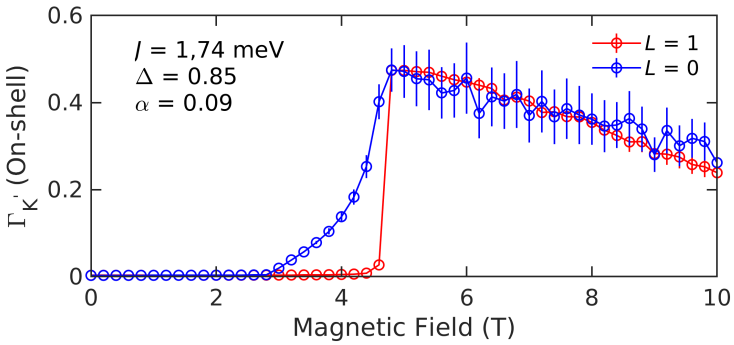

Figure 5.8: The field dependence of the on-shell magnon decay rate $\mathrm{Im}\Sigma_{11}^{(a)}(\mathbf{k}, \varepsilon_{\mathbf{k}})$ calculated at $(2/3, 2/3, 0)$ and $(2/3, 2/3, 1)$, i. e., K′ points with different L.

Specifically, it starts to allow magnon decay at some threshold field around one of the zone center K′ point, which is clearly shown by the calculation presented in Figure 5.8.

Now it is time to consider the dynamical structure factor. The key to obtaining it with $1/S$ correction is to get the corrected one-magnon Green's function $\mathcal{G}(\mathbf{k}, \varepsilon)$. In linear spin-wave theory, where magnons are free quasi-particles, the Green's function is simply

$$\mathcal{G}_0(\mathbf{k}, \varepsilon) = \frac{1}{\varepsilon - \varepsilon_{\mathbf{k}} + i0_+}, \tag{5.60}$$

which explains the origin of the delta spectral functions in the dynamical structure factors there.

The perturbed Green's function is calculated following the Dyson's equation

$$\mathcal{G}(\mathbf{k}, \varepsilon) = \left[\mathcal{G}_0(\mathbf{k}, \varepsilon)^{-1} - \Sigma(\mathbf{k}, \varepsilon) + i0_+\right]^{-1} = \left[\varepsilon - \varepsilon_{\mathbf{k}} - \Sigma(\mathbf{k}, \varepsilon) + i0_+\right]^{-1}, \tag{5.61}$$

where

$$\Sigma(\mathbf{k},\varepsilon) = \Sigma_{\mathrm{HF}}(\mathbf{k}) + \Sigma_{11}^{(a)}(\mathbf{k},\varepsilon) + \Sigma_{11}^{(b)}(\mathbf{k},\varepsilon). \tag{5.62}$$

The spectral function $A(\mathbf{k},\varepsilon)$ is

$$A(\mathbf{k},\varepsilon) = -\frac{1}{\pi}\mathrm{Im}\left[\mathcal{G}(\mathbf{k},\varepsilon)\right]. \tag{5.63}$$

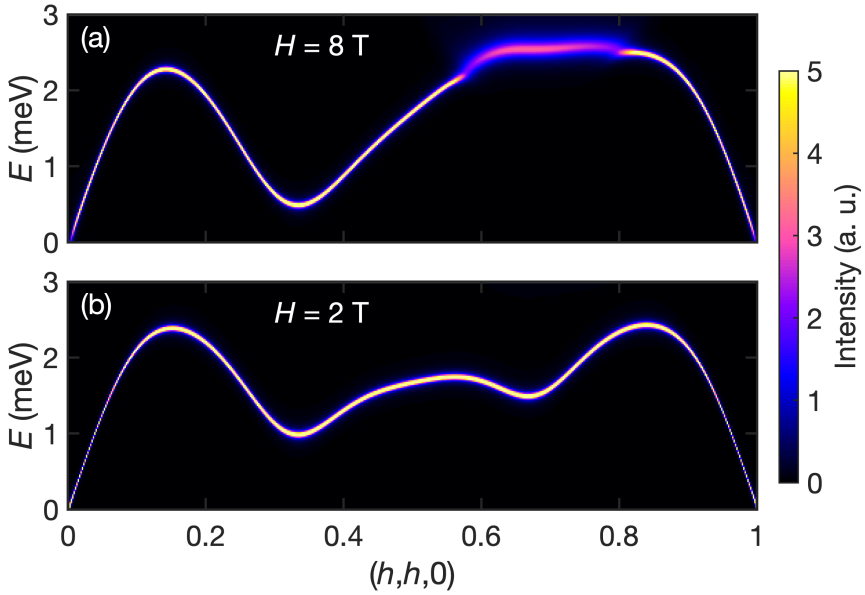

Figure 5.9: The spectral function $A(\mathbf{k},\varepsilon)$ at (a) $H = 8$ T and (b) $H = 2$ T.

As illustrated in Figure 5.9, the field-dependence of the spectral function is already sufficient to indicate the dampening of the one-magnon band around K′ point $(2/3, 2/3, 0)$.

Equation 5.28 remains valid for the $1/S$ dynamical structure factor with slight modifications

$$\mathcal{S}^{xx(yy)}(\mathbf{q},\varepsilon) = \frac{S}{2}\Lambda_{\pm}^2(u_{\mathbf{q}} \pm v_{\mathbf{q}})^2 A(\mathbf{q},\varepsilon), \tag{5.64}$$

$$\mathcal{S}^{xy}(\mathbf{q},\varepsilon) = i\frac{S}{2}\Lambda_{+}\Lambda_{-} A(\mathbf{q},\varepsilon), \tag{5.65}$$

$$\mathcal{S}^{zz}(\mathbf{q},\varepsilon) = \frac{1}{2}\sum_{\mathbf{k}}(u_{\mathbf{k}}v_{\mathbf{k}-\mathbf{q}} + v_{\mathbf{k}}u_{\mathbf{k}-\mathbf{q}})^2\delta(\varepsilon - \varepsilon_{\mathbf{k}} - \varepsilon_{\mathbf{k}-\mathbf{q}}), \tag{5.66}$$

where $\Lambda_{\pm} = 1 - (2n \pm \delta)/(4S)$. There is no additional treatment required for the longitu-

dinal part $\mathcal{S}^{zz}$ because that term is related to the two-magnon continuum and is already at the order of $\mathcal{O}(1/S)$.

The spin-wave calculation now awaits the comparison with the inelastic neutron scattering data to generate some insights. The neutron scattering experiment was performed on CNCS, SNS with the same sample used in Ref. [89]. Unlike the zero-field case where the (h, h, l) plane was aligned horizontally to cover the magnetic Bragg peak at $(1/3, 1/3, 1)$, it was the $(h, k, 0)$ plane being horizontal for the vertical magnetic field to be applied along c-axis. The trade-off is the instrument was unable to measure any magnetic Bragg peak with its best and commonly used incident neutron energy $E_\mathrm{i} = 3.315$ meV since the vertical the coverage along $(0, 0, l)$ opening is significantly limited by detector banks as well as the opening of the magnet.

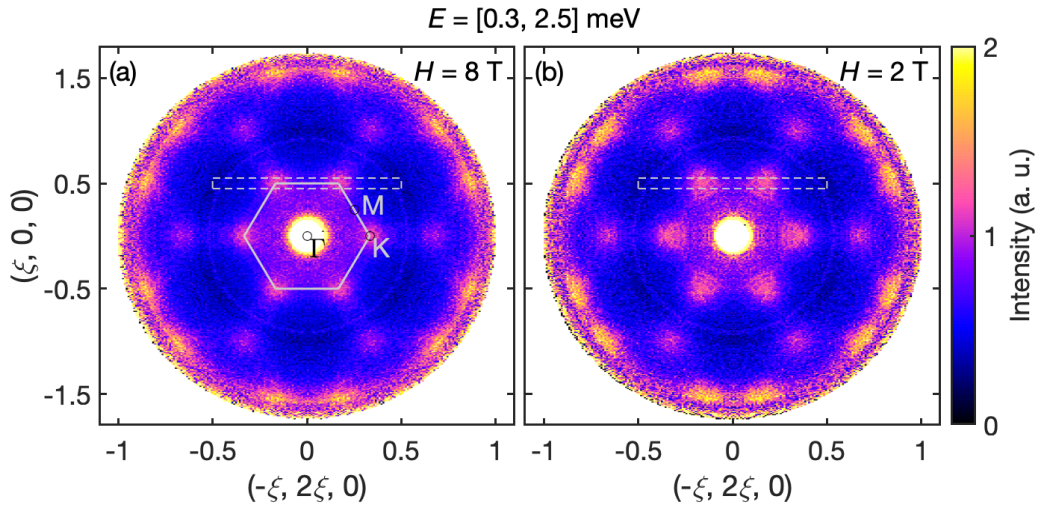

Figure 5.10: The energy-integrated inelastic neutron scattering spectra collected on CNCS, SNS at (a) $H = 8$ T and (b) $H = 2$ T. Both are measured at $T \sim 0.1$ K with the incident neutron energy $E_\mathrm{i} = 3.315$ meV. The grey hexagon represents the first Brillouin zone for the magnetic unit cell. The dashed boxes indicate where the slices in Figure 5.11(a),(d) are produced from.

The normal way to present the single-crystal neutron spectra with momentum and energy dependence is to configure a path in the Brillouin zone with various high-symmetry points. As one can see in Figure 5.10, the observed signal for magnetic excitations is highly concentrated around K points and their paths to M points. Therefore, a simple and straight

path is picked, as illustrated with the dashed boxes in Figure 5.10.

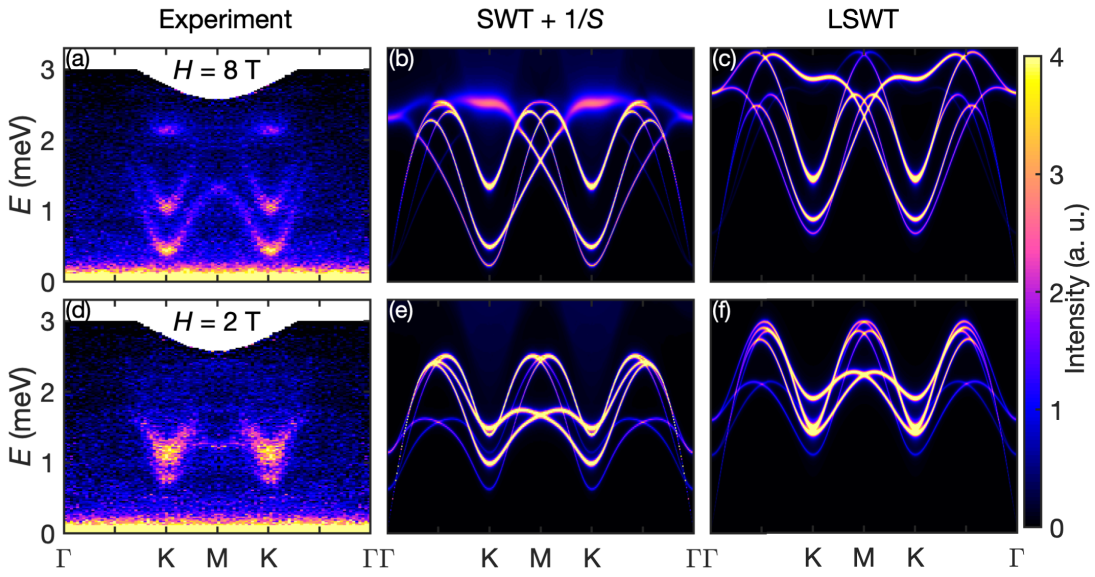

Figure 5.11: (a) Inelastic neutron scattering data collected on CNCS, SNS at $H = 8$ T and at $T \sim 0.1$ K and the incident neutron energy $E_{\rm i} = 3.315$ meV. (b) The $1/S$ spin-wave calculation at $H = 8$ T. (c) The linear spin-wave calculation at $H = 8$ T. (d) Inelastic neutron scattering data collected on CNCS, SNS at $H = 2$ T and at $T \sim 0.1$ K. (e) The $1/S$ spin-wave calculation at $H = 2$ T. (f) The linear spin-wave calculation at $H = 2$ T. All spin-wave calculations use the parameters extracted from the UUD case and $g_\perp = 4$.

Figure 5.11 shows a detailed comparison between the experimental data with the spin-wave calculations with or without $1/S$ correction. The parameters used for the spin-wave calculations are given by the UUD phase study and $g_\perp$ is set to 4.

An obvious difference between the neutron data and the spin-wave results is the distribution of the spectral weight across the momentum space. While there exhibits little intensity left besides M and K points in the experimental data, the spin-wave simulation has fairly strong excitation branches along the entire path. Although the magnetic form factor may account for the decrease of the intensity as Q gets larger, it does not seem sufficient to explain why the spectral weight is so concentrated here.

Meanwhile, the bandwidth of the excitations does not give a good match here. This is understandable since even the UUD case did not achieve a perfect match at both K and M points. Although the $1/S$ correction, like in the zero-field case, already causes a strong

renormalization of the bandwidth, the calculated modes around K point are still at higher energies.

By comparing 2-T and 8-T data, one can find that $1/S$ spin-wave theory works comparatively better in the high-field case. Despite that most excitations start to vanish above $E = 1.5$ meV in the experimental data, the highest mode around $E = 2.2$ meV resembles the calculated dampened magnon mode at $E \sim 2.5$ meV. Whereas the signal completely vanishes above $E \sim 1.6$ meV in 2-T data which very much resembles the zero-field scenario. It is also likely that the $E \sim 3.5$ meV mode around M point persists in the 2-T data, but this could not be unambiguously verified for instrumental reasons.

Overall, a quantitative understanding of the experimental data using spin-wave theory seems unrealistic since there are many unexplainable features. In particular, the M point behavior, which turns from a local minimum to a saddle point as the fields increases, escapes again the spin-wave picture.

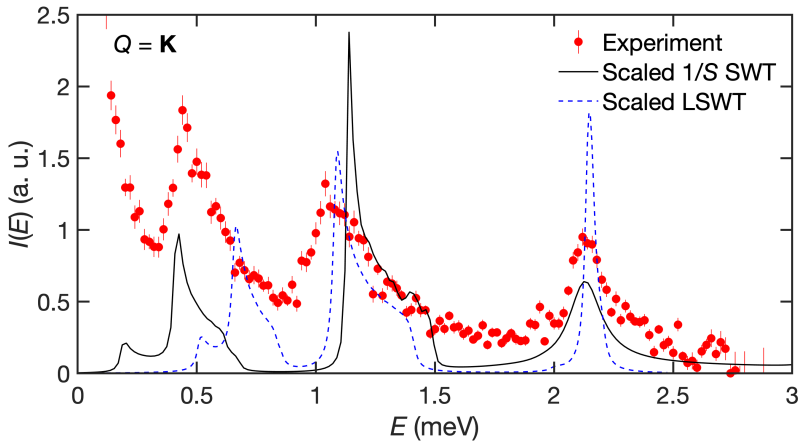

Figure 5.12: Red circles show the Q-integrated cut from the experimental data around K point. The solid line is the same cut from the $1/S$ SWT calculation with the energy scaled by a factor of 0.85. The solid line is the same cut from the LSWT calculation with the energy scaled by a factor of 0.75.

One question that remains worthwhile to ask is whether or not the high-energy mode around $E = 2.2$ meV in the 8-T data has any indication of the field-induced magnon decay. Therefore, a cut around K point is performed and shown in Figure 5.12. As benchmarking

the bandwidth is less important now, the SWT calculations are scaled by some factors such that the excitation modes roughly match. As one can see, while those two modes at lower energies have their widths similar to the calculated peaks, the high-energy mode seems to be broader than the free-magnon peak given by LSWT. Although this is not a rigorous proof mathematically, it does support the picture of field-induced magnon decay.

5.2.6 Spin dynamics in the low-field co-planar phase

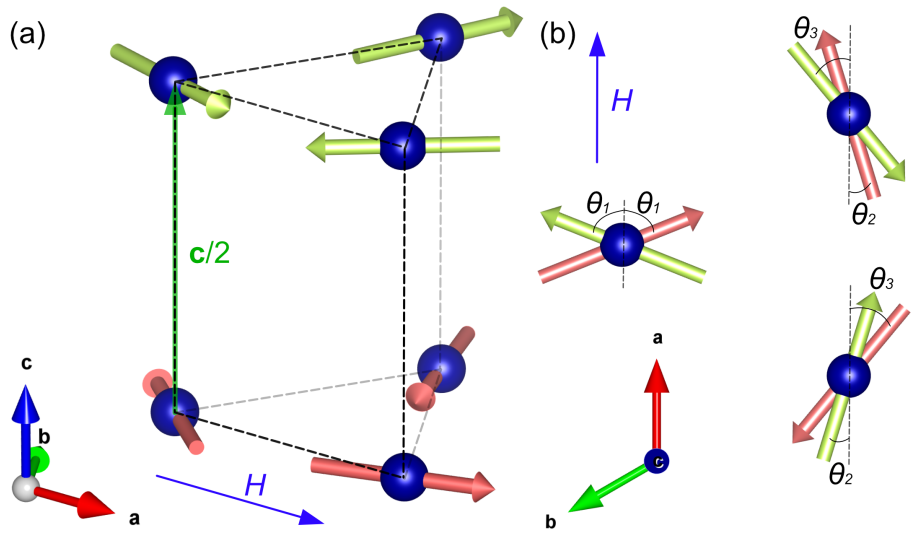

Figure 5.13: (a) A crystallographic view of the low-field co-planar state. (b) Illustration of the angles between the applied field and the spins.

As introduced earlier, the system goes through an intermediate phase with the applied in-plane magnetic field before stabilizing itself at the plateau. However, the illustration included in the magnetization curves [Figure 5.1(b)] incorrectly describes the magnetic structure of such a state for the neglect of the interlayer coupling J_c. In fact, as was discussed in Ref. [88], the spin structure can still fit within the magnetic unit cell containing six spins [Figure 5.13]. What it makes it complicated is none of the spins now is parallel or anti-parallel with the field, nor does it possess the nice three-fold symmetry like the zero-field or "umbrella" case. As shown in Figure 5.13(b), one now needs three angles $\theta_{1,2,3}$ which are only numerically solvable. Note that the structure does continuously transform

into the zero-field case, where θ_1 is $\pi/2$ and $\theta_{2,3}$ turn zero.

As a matter of fact, this intermediate phase has drawn little attention from the theory side for mainly two reasons. First, it is a complicated spin structure that prevents most simple and elegant approaches. Second, it is regarded as a state that bridges the zero-field and plateau phase and not supposed to exhibit anything fundamentally different. From the experiment-driven point of view, however, it will be quite helpful to investigate on this phase. Because this can offer direct information on how the "mysterious" zero-field excitations transform into the comparatively well-defined UUD ones. Particularly, it will provide valuable insights on the 3.5 meV mode from its dependence on the magnetic field.

That being said, it is an undeniable fact that a careful theoretical treatment, namely the spin-wave calculation with $1/S$ correction, is prohibitively complex here. Therefore, this section will start with the discussion about the experimental results, followed by linear spin-wave calculations. The derivations related to the $1/S$ correction ought to be shown in the end, however with the absence of actual numerical simulations which are computationally unfeasible.

The neutron scattering experiment as detailed as the UUD one was conducted at $H = 7$ T and $T = 0.5$ K. Figure 5.14 displays the processed results. Two excitation modes emerging from K points are observed around $E = 0$ meV and $E = 2$ meV [Figure 5.14(a)]. The spectral weight is largely concentrated around K points, which is similar to the "umbrella" case. The higher mode disperses to around $E = 3.5$ meV at M points. However, it does not resemble the intensive mode observed in zero-field case [Figure 5.2(b)]. Unlike the UUD case, the modes are quite dispersive along $(0, 0, l)$ at K points [Figure 5.14(c)]. The low-energy mode, as shown in the cut [Figure 5.14(d)], appears to be gapped although the instrumental resolution is insufficient to well separate it from the elastic line. Meanwhile, one can observe evidently stronger continuum-like signal around the M point above $E = 2$ meV [Figure 5.14(e)]. The signal is indeed from the sample through the comparison with the UUD cuts which were measured and processed in identical settings.

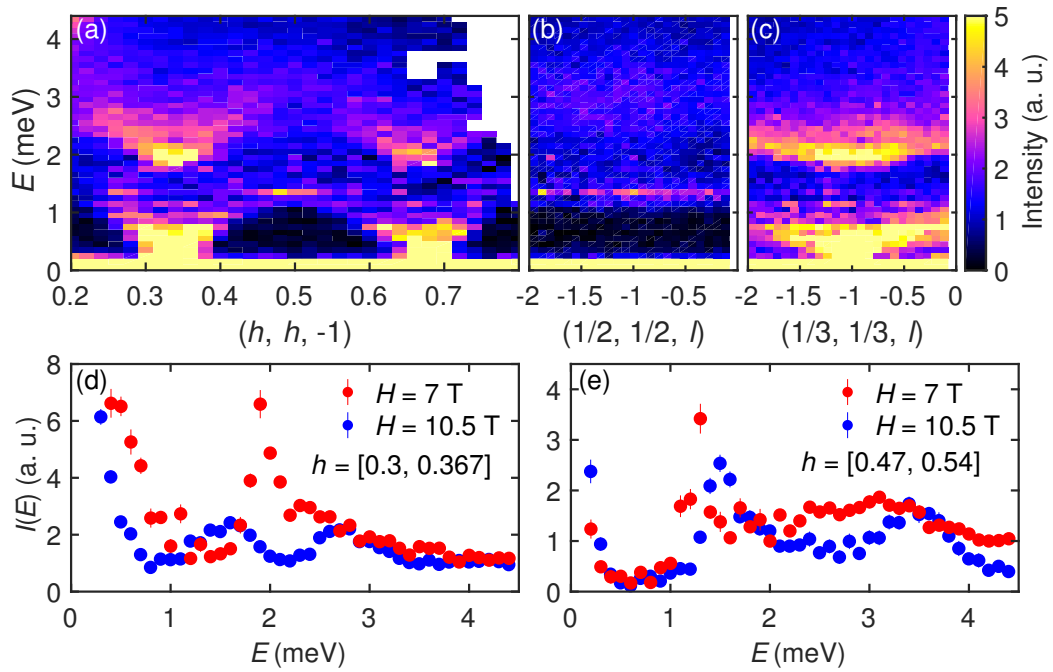

Figure 5.14: Excitation spectra in the low-field co-planar phase of $Ba_3CoSb_2O_9$ at $H = 7$ T and $T = 0.5$ K. (a)-(c) Slices of the data as functions of energy and momentum transfers along different directions. (d) The Q-integrated cuts around K point. (e) The Q-integrated cuts around M point. The corresponding cuts in UUD phase are included for comparison. Intensity is arbitrary but consistent across all panels.

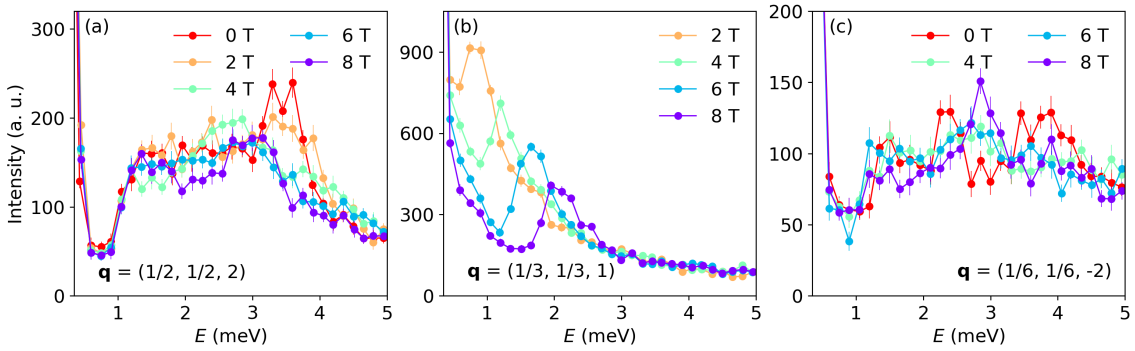

Figure 5.15: Energy-dependent scans at selected Q's to demonstrate the magnetic field dependence. Intensity is arbitrary but consistent across all panels.

In addition to the 7-T data which is already interesting, more energy scans were performed at selected Q's with various applied fields [Figure 5.15]. The measurement utilized the triple-axis mode of MACS in that only a single detector count was recorded. This is certainly not the most ideal way of using MACS but it is able to provide the most consis-

tency and accuracy in the targeted Q's. The result at K point is somewhat trivial as it simply shows how the excitation minimum gets shifted by the applied field [Figure 5.15(b)]. In contrast, the results at M point $(1/2, 1/2, 2)$ and Y_1 point $(1/6, 1/6, -2)$ exhibit very interesting behavior [Figure 5.15(a),(c)]. In particular, the 3.5 meV mode at M point that is clearly observed at zero field gets dampened as the field increases and disappears at $H = 4$ T. The signal around $E = 1.5$ meV, which is supposed to be some band top, is weakened first and strengthened again with $H = 4$ T being the turning point. At $H = 6$ T, both scans at M and Y_1 points become a very broad continuum before distinguishable modes show up again at $H = 8$ T. Overall, the observation strongly implies the existence of some threshold field between 4 T and 6 T during which the system drastically changes its behavior.

Now it is time to carry out the linear spin-wave calculations. It is almost certain linear spin-wave theory cannot provide a good description of the data, but it is again useful to see where its limit lies. Lacking the nice three-fold symmetry in the plane, the work has to be done in the extended magnetic cell which is three times bigger than the simplest hexagon. As a result, the first Brillouin zone also shrinks by three times. To avoid confusion, it is worth writing those lattice vectors and their relations down first.

The convention adapted here for the original lattice vectors are

$$\mathbf{a}_1 = a\hat{x}, \tag{5.67}$$

$$\mathbf{a}_2 = \frac{a}{2}\hat{x} + \frac{\sqrt{3}a}{2}\hat{y}, \tag{5.68}$$

$$\mathbf{a}_3 = c\hat{z}. \tag{5.69}$$

and the reciprocal space lattice vectors are

$$\mathbf{b}_1 = \frac{2\pi}{a}\hat{k}_x - \frac{2\pi}{\sqrt{3}a}\hat{k}_y, \tag{5.70}$$

$$\mathbf{b}_2 = \frac{4\pi}{\sqrt{3}a}\hat{k}_y, \tag{5.71}$$

$$\mathbf{b}_3 = \frac{2\pi}{c}\hat{k}_z. \tag{5.72}$$

With the extended cell, the real space lattice vectors become

$$\mathbf{a}_1' = \mathbf{a}_1 + \mathbf{a}_2, \tag{5.73}$$

$$\mathbf{a}_2' = -\mathbf{a}_1 + 2\mathbf{a}_2, \tag{5.74}$$

$$\mathbf{a}_3' = \mathbf{a}_3. \tag{5.75}$$

Therefore, the corresponding reciprocal lattice vectors become

$$\mathbf{b}_1' = \frac{2}{3}\mathbf{b}_1 + \frac{1}{3}\mathbf{b}_2 = \frac{4\pi}{\sqrt{3}a}\hat{k}_x, \tag{5.76}$$

$$\mathbf{b}_2' = -\frac{1}{3}\mathbf{b}_1 + \frac{1}{3}\mathbf{b}_2 = -\frac{2\pi}{3a}\hat{k}_x + \frac{2\pi}{\sqrt{3}a}\hat{k}_y, \tag{5.77}$$

$$\mathbf{b}_3' = \mathbf{b}_3 = \frac{2\pi}{c}\hat{k}_z. \tag{5.78}$$

The summation is done over the first Brillouin zone of the extended cell, while all the notation, such as the high symmetry points, are kept consistent with the original cell for easy comparison.

The magnetic field is assumed to be along x_0-axis. Furthermore, θ_i will be the angle of each spin in one extended cell in the x_0-y_0 plane. And it will be convenient to define define θ_{ij} to be the angle between $\mathbf{S}_i$ and $\mathbf{S}_j$ in the extended unit cell, *i.e.*, $\theta_{ij} \equiv \theta_i - \theta_j$, and θ_{ih} the angle between the magnetic field $\mathbf{H}$ and $\mathbf{S}_i$. Under this condition, the transformation of spin operators, which is slightly different from previous section, writes

$$S_i^{x_0} = -S_i^y \sin\theta_i + S_i^z \cos\theta_i, \tag{5.79}$$

$$S_i^{y_0} = S_i^y \cos\theta_i + S_i^z \sin\theta_i, \tag{5.80}$$

$$S_i^{z_0} = -S_i^x. \tag{5.81}$$

The spin Hamiltonian is

$$\begin{aligned}\mathcal{H} =& J \sum_{\langle nm,ij\rangle} S_{ni}^x S_{mj}^x \Delta + \left(S_{ni}^y S_{mj}^y + S_{ni}^z S_{mj}^z\right)\cos\theta_{ij} - \left(S_{ni}^y S_{mj}^z - S_{ni}^z S_{mj}^y\right)\sin\theta_{ij} \\ &+ J' \sum_{\langle nn',ii'\rangle} S_{ni}^x S_{n'i'}^x \Delta + \left(S_{ni}^y S_{n'i'}^y + S_{ni}^z S_{n'i'}^z\right)\cos\theta_{ii'} - \left(S_{ni}^y S_{n'i'}^z - S_{ni}^z S_{n'i'}^y\right)\sin\theta_{ii'} \\ &- \sum_{n,i} g\mu_{\mathrm{B}} H \left(S_{n,i}^z \cos\theta_{i\mathrm{h}} - S_{n,i}^y \sin\theta_{i\mathrm{h}}\right),\end{aligned} \tag{5.82}$$

where subscripts i, i' and j are summed over the six sub-lattices and n, n' and m are the indices for the extended unit cells.

The linear term $\mathcal{H}^{(1)}$ is

$$\begin{aligned}\mathcal{H}^{(1)} =& JS\frac{i\sqrt{2S}}{2} \sum_{\langle nm,ij\rangle} \left(a_{i,n} - a_{i,n}^\dagger - a_{j,m} + a_{j,m}^\dagger\right)\sin\theta_{ij} \\ &+ J_c S\frac{i\sqrt{2S}}{2} \sum_{\langle nn',ii'\rangle} \left(a_{i,n} - a_{i,n}^\dagger - a_{i',m} + a_{i',m}^\dagger\right)\sin\theta_{ii'} \\ &+ g\mu_{\mathrm{B}} H \frac{i\sqrt{2S}}{2} \sum_{n,i} \left(a_{i,n} - a_{i,n}^\dagger\right)\sin\theta_{i\mathrm{h}},\end{aligned} \tag{5.83}$$

which should in principle give the classical ground state condition.

The harmonic Hamiltonian is

$$\mathcal{H}^{(2)} = 3JS \sum_{\mathbf{k}} a_{i,\mathbf{k}}^\dagger A_{\mathbf{k}}^{ij} a_{j,\mathbf{k}} - \frac{1}{2}(a_{i,\mathbf{k}}^\dagger B_{\mathbf{k}}^{ij} a_{j,-\mathbf{k}}^\dagger + \mathrm{h.c.}), \tag{5.84}$$

where $A^{ij}_{\mathbf{k}}$ and $B^{ij}_{\mathbf{k}}$ are elements of the 6×6 Hermitian matices $\mathbf{A_k}$ and $\mathbf{B_k}$. From now on the subscript $\mathbf{k}$ will be often omitted for simplicity.

For the diagonal terms,

$$A^{ii} = \frac{g\mu_{\mathrm{B}}H}{3JS}\cos\theta_{i\mathrm{h}} - \frac{2\alpha}{3}\cos\theta_{ii+3} - \sum_j \cos\theta_{ij}, \tag{5.85}$$

where j is summed over the nearest-neighbor indices.

For the elements corresponding to the nearest-neighbor coupling in layers, *i.e.*, $i, j \in \{1,2,3\}$ or $\{4,5,6\}$ and $i \neq j$,

$$A^{ij} = \frac{\Delta + \cos\theta_{ij}}{2}\gamma_{ij}, \tag{5.86}$$

$$B^{ij} = -\frac{\Delta - \cos\theta_{ij}}{2}\gamma_{ij}, \tag{5.87}$$

where

$$\gamma_{ij} = \gamma^*_{ji} = \frac{1}{3}\left[e^{i2\pi k_x} + 2e^{-i\pi k_x}\cos\sqrt{3}\pi k_y\right]. \tag{5.88}$$

where $(i,j) \in \{(1,2),(2,3),(3,1),(4,5),(5,6),(6,4)\}$.

Likewise, the elements corresponding to the interlayer coupling, *e.g.*, $(i,j) = (1,4)$, are,

$$A^{ij} = \frac{2\alpha}{3}\frac{\Delta + \cos\theta_{ij}}{2}\cos\pi k_z, \tag{5.89}$$

$$B^{ij} = -\frac{2\alpha}{3}\frac{\Delta - \cos\theta_{ij}}{2}\cos\pi k_z. \tag{5.90}$$

All the other elements are zero.

The square roots of the eigenvalues of $(\mathbf{A_q}+\mathbf{B_q})(\mathbf{A_q}-\mathbf{B_q})$ multiplied by $3JS$ are the single-magnon excitation states. And the corresponding eigenbasis is obtained by the generalized Bogolubov transformation,

$$\begin{pmatrix} \mathbf{a_q} \\ \mathbf{a}^\dagger_{\mathbf{-q}} \end{pmatrix} = \begin{pmatrix} \mathbf{U_q} & \mathbf{V_q} \\ \mathbf{V_q} & \mathbf{U_q} \end{pmatrix} \begin{pmatrix} \mathbf{b_q} \\ \mathbf{b}^\dagger_{\mathbf{-q}} \end{pmatrix}, \tag{5.91}$$

where $\mathbf{U_q}$ and $\mathbf{V_q}$ are now 6 by 6 matrices.

Applying the coordinate and Fourier transformation to the spin operators, one now has

$$\begin{aligned} S^{x_0}_{\mathbf{q}} =& \frac{1}{N}\sum_{i,n}\left(-S^y_{i,n}\sin\theta_i + S^z_{i,n}\cos\theta_i\right)e^{-i\mathbf{q}\cdot\mathbf{r}_{i,n}} \\ =& \sum_i\left[i\sqrt{\frac{S}{12}}\left(a_{i,\mathbf{q}}-a^\dagger_{i,\mathbf{-q}}\right)\sin\theta_i + \left(\frac{\sqrt{N}}{6}S\delta_{\mathbf{q},0} - \frac{1}{\sqrt{N}}\sum_{\mathbf{k}}a^\dagger_{i,\mathbf{k-q}}a_{\mathbf{q}}\right)\cos\theta_i\right], \end{aligned} \tag{5.92}$$

$$\begin{aligned} S^{y_0}_{\mathbf{q}} =& \frac{1}{N}\sum_{i,n}\left(S^y_{i,n}\cos\theta_i + S^z_{i,n}\sin\theta_i\right)e^{-i\mathbf{q}\cdot\mathbf{r}_{i,n}} \\ =& \sum_i\left[-i\sqrt{\frac{S}{12}}\left(a_{i,\mathbf{q}}-a^\dagger_{i,\mathbf{-q}}\right)\cos\theta_i - \left(\frac{\sqrt{N}}{6}S\delta_{\mathbf{q},0} - \frac{1}{\sqrt{N}}\sum_{\mathbf{k}}a^\dagger_{i,\mathbf{k-q}}a_{\mathbf{q}}\right)\sin\theta_i\right], \end{aligned} \tag{5.93}$$

and

$$\begin{aligned} S^{z_0}_{\mathbf{q}} =& -\frac{1}{\sqrt{N}}\sum_{i,n}S^x_{i,n}e^{-i\mathbf{q}\cdot\mathbf{r}_{i,n}} \\ =& -\sum_i\sqrt{\frac{S}{12}}\left(a_{i,\mathbf{q}}+a^\dagger_{i,\mathbf{q}}\right). \end{aligned} \tag{5.94}$$

As before, the above terms are used to calculate the dynamical structure factors

$$\mathcal{S}^{x_0x_0}(\mathbf{q},\omega) = \frac{NS^2}{36}\sum_{i,j}\delta(\omega)\delta_{\mathbf{q},0}\cos\theta_i\cos\theta_j + \frac{S}{12}\sum_j\delta(\omega-\omega_j)\left|\sum_i\sin\theta_i\left(U^{ij}_{\mathbf{q}}-V^{ij}_{\mathbf{q}}\right)\right|^2, \tag{5.95}$$

$$\mathcal{S}^{y_0y_0}(\mathbf{q},\omega) = \frac{NS^2}{36}\sum_{i,j}\delta(\omega)\delta_{\mathbf{q},0}\sin\theta_i\sin\theta_j + \frac{S}{12}\sum_j\delta(\omega-\omega_j)\left|\sum_i\cos\theta_i\left(U^{ij}_{\mathbf{q}}-V^{ij}_{\mathbf{q}}\right)\right|^2, \tag{5.96}$$

$$\mathcal{S}^{x_0y_0}(\mathbf{q},\omega) = \left(\mathcal{S}^{y_0x_0}_{\mathbf{q}}\right)^* = \frac{S}{12}\sum_{i,j,k}\delta(\omega-\omega_k)\sin\theta_i\cos\theta_j\left(U^{ik}_{\mathbf{q}}-V^{ik}_{\mathbf{q}}\right)\left(U^{jk}_{\mathbf{q}}-V^{jk}_{\mathbf{q}}\right), \tag{5.97}$$

$$\mathcal{S}^{x_0z_0}(\mathbf{q},\omega) = \left(\mathcal{S}^{z_0x_0}(\mathbf{q},\omega)\right)^* = -i\frac{S}{12}\sum_{i,j,k}\delta(\omega-\omega_k)\sin\theta_i\left(U^{ik}_{\mathbf{q}}-V^{ik}_{\mathbf{q}}\right)\left(U^{jk}_{\mathbf{q}}+V^{jk}_{\mathbf{q}}\right), \tag{5.98}$$

$$\mathcal{S}^{y_0z_0}(\mathbf{q},\omega) = \left(\mathcal{S}^{z_0y_0}(\mathbf{q},\omega)\right)^* = -i\frac{S}{12}\sum_{i,j,k}\delta(\omega-\omega_k)\cos\theta_i\left(U^{ik}_{\mathbf{q}}-V^{ik}_{\mathbf{q}}\right)\left(U^{jk}_{\mathbf{q}}+V^{jk}_{\mathbf{q}}\right), \tag{5.99}$$

and

$$\mathcal{S}^{z_0z_0}(\mathbf{q},\omega) = \frac{S}{12}\sum_j\delta(\omega-\omega_j)\left|\sum_i\left(U^{ij}_{\mathbf{q}}+V^{ij}_{\mathbf{q}}\right)\right|^2. \tag{5.100}$$

With the parameters from the UUD study, the spin dynamical structure factor is calculated and presented in Figure 5.16. Unlike the experimental data where two strong modes are observed, one can clearly see three excitation modes, which are actually composed of six magnon poles, emerging from K points. Although the continuum-like broad signal is not presented in the simulation, the highest and lowest modes do somewhat resemble the experimental observation. However, the middle branch is completely absent in the data. Meanwhile, although there is no continuous symmetry left in the Hamiltonian once the in-plane field is applied, one of the magnon poles will remain gapless in the linear spin-wave

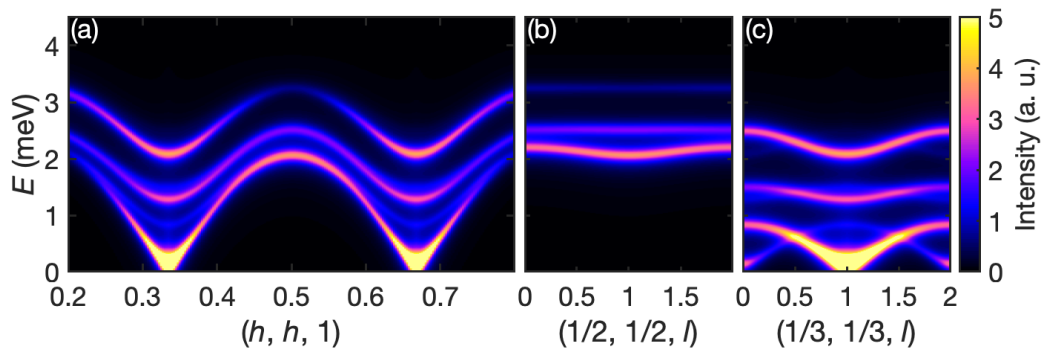

Figure 5.16: Magnon excitation spectra calculated from LSWT using the parameters from the UUD study. The slices are made in a comparable way to Figure 5.14(a)-(c).

result. This is opposite to what was seen in the data, where the all the excitations are gapped out.

Considering the accuracy obtained in the UUD data, it is unlikely that the invisibility of the middle branch is caused by the instrumental resolution. Meanwhile, 7 T is beyond the potential turning point observed in the energy scans such that it is reasonable to believe spin-wave theory starts to work better than lower field cases here. Therefore, it would be beneficial to consider the $1/S$ correction and verify whether the renormalized spectrum could resolve the middle branch issue. Unfortunately, the calculation in such a non-Bravais lattice case has been asserted to be computationally unfeasible [97]. Nevertheless, the derivations shall be presented below and await future benchmarks.

In the order of $\mathcal{O}(1/S)$ where the contribution from the cubic term $\mathcal{H}^{(3)}$ gets taken into account, all the angles between different sub-lattice spins will change. The correction from decoupled quartic terms is also important. Besides, the self-energies from those three-magnon vertices are crucial as well.

All of those require the explicit forms of $\mathcal{H}^{(3)}$ and $\mathcal{H}^{(4)}$, which are

$$\begin{aligned}
\mathcal{H}^{(3)} = J\frac{i\sqrt{2S}}{2}\sum_{\langle nm,ij\rangle}\Big[\Big(&a^\dagger_{i,n}a_{i,n}a_{j,m} - a^\dagger_{i,n}a_{i,n}a^\dagger_{j,m} - a_{i,n}a^\dagger_{j,m}a_{j,m} + a^\dagger_{i,n}a^\dagger_{j,m}a_{j,m}\Big)\\
&+\frac{1}{4}\Big(a^\dagger_{i,n}a^\dagger_{i,n}a_{i,n} - a^\dagger_{i,n}a_{i,n}a_{i,n} + a^\dagger_{j,m}a_{j,m}a_{j,m} - a^\dagger_{j,m}a^\dagger_{j,m}a_{j,m}\Big)\Big]\sin\theta_{ij}\\
+J_c\frac{i\sqrt{2S}}{2}\sum_{\langle nn',ii'\rangle}\Big[\Big(&a^\dagger_{i,n}a_{i,n}a_{i',n'} - a^\dagger_{i,n}a_{i,n}a^\dagger_{i',n'} - a_{i,n}a^\dagger_{i',n'}a_{i',n'} + a^\dagger_{i,n}a^\dagger_{i',n'}a_{i',n'}\Big)\\
&+\frac{1}{4}\Big(a^\dagger_{i,n}a^\dagger_{i,n}a_{i,n} - a^\dagger_{i,n}a_{i,n}a_{i,n} + a^\dagger_{i',n'}a_{i',n'}a_{i',n'} - a^\dagger_{i',n'}a^\dagger_{i',n'}a_{i',n'}\Big)\Big]\sin\theta_{ii'}\\
+g\mu_{\mathrm{B}}H\frac{i\sqrt{2S}}{2}\frac{1}{4S}\sum_{n,i}&(a^\dagger_{i,n}a_{i,n}a_{i,n} - a^\dagger_{i,n}a^\dagger_{i,n}a_{i,n})\sin\theta_{i\mathrm{h}}
\end{aligned}\tag{5.101}$$

$$\begin{aligned}
\mathcal{H}^{(4)} = \frac{J}{8}\sum_{\langle nm,ij\rangle}\Big[\Big(&a_{i,n}a^\dagger_{j,m}a_{j,m}a_{j,m} + a^\dagger_{i,n}a^\dagger_{j,m}a^\dagger_{j,m}a_{j,m} + a^\dagger_{i,n}a_{i,n}a_{i,n}a_{j,m} + a^\dagger_{i,n}a^\dagger_{i,n}a_{i,n}a^\dagger_{j,m}\Big)\\
&(\cos\theta_{ij} - \Delta)\\
-\Big(&a_{i,n}a^\dagger_{j,m}a^\dagger_{j,m}a_{j,m} + a^\dagger_{i,n}a^\dagger_{j,m}a_{j,m}a_{j,m} + a^\dagger_{i,n}a_{i,n}a_{i,n}a^\dagger_{j,m} + a^\dagger_{i,n}a^\dagger_{i,n}a_{i,n}a_{j,m}\Big)\\
&(\cos\theta_{ij} + \Delta)\\
+&\,a^\dagger_{i,n}a_{i,n}a^\dagger_{j,m}a_{j,m}\cos\theta_{ij}\Big]\\
+\frac{J_c}{8}\sum_{\langle nn',ii'\rangle}\Big[\Big(&a_{i,n}a^\dagger_{i',n'}a_{i',n'}a_{i',n'} + a^\dagger_{i,n}a^\dagger_{i',n'}a^\dagger_{i',n'}a_{i',n'} + a^\dagger_{i,n}a_{i,n}a_{i,n}a_{i',n'} + a^\dagger_{i,n}a^\dagger_{i,n}a_{i,n}a^\dagger_{i',n'}\Big)\\
&(\cos\theta_{ii'} - \Delta)\\
-\Big(&a_{i,n}a^\dagger_{i',n'}a^\dagger_{i',n'}a_{i',n'} + a^\dagger_{i,n}a^\dagger_{i',n'}a_{i',n'}a_{i',n'} + a^\dagger_{i,n}a_{i,n}a_{i,n}a^\dagger_{i',n'} + a^\dagger_{i,n}a^\dagger_{i,n}a_{i,n}a_{i',n'}\Big)\\
&(\cos\theta_{ii'} + \Delta)\\
+&\,a^\dagger_{i,n}a_{i,n}a^\dagger_{i',n'}a_{i',n'}\cos\theta_{ii'}\Big]
\end{aligned}\tag{5.102}$$

To proceed, the Hartree-Fock averages in this case are defined as

$$\rho_{ij} \equiv \frac{1}{N_{\text{cell}}} \left\langle a_{i,n}^{\dagger} a_{j,n} \right\rangle = \frac{1}{N_{\text{cell}}} \sum_{\mathbf{k}} \gamma_{ij}(\mathbf{k}) \sum_{\alpha=1}^{6} \left(V_{\mathbf{k}}^{i\alpha}\right)^{*} V_{\mathbf{k}}^{j\alpha} \tag{5.103}$$

$$\xi_{ij} \equiv \frac{1}{N_{\text{cell}}} \left\langle a_{i,n} a_{j,n} \right\rangle = \frac{1}{N_{\text{cell}}} \sum_{\mathbf{k}} \gamma_{ij}(\mathbf{k}) \sum_{\alpha=1}^{6} U_{\mathbf{k}}^{i\alpha} \left(V_{\mathbf{k}}^{j\alpha}\right)^{*} \tag{5.104}$$

where N_{cell} is the number of the extended unit cells and obviously $\gamma_{ii}(\mathbf{k}) = 1$. Due to the fact that $\gamma_{ij}(\mathbf{k}) = \gamma_{ij}^{*}(-\mathbf{k})$, $U_{\mathbf{k}}^{ij} = \left(U_{-\mathbf{k}}^{ij}\right)^{*}$, $V_{\mathbf{k}}^{ij} = \left(V_{-\mathbf{k}}^{ij}\right)^{*}$ and the inversion symmetry of the first Brillouin Zone, all the Hartree-Fock averages have real values. Therefore, $\rho_{ij} = \rho_{ji}$ and $\xi_{ij} = \xi_{ji}$. For simplicity, terms like ρ_{ii} will be denoted as ρ_i.

The obtained linear Hamiltonian by performing Hartree-Fock decoupling is,

$$\begin{aligned}
\mathcal{H}_{\text{HF}}^{(3)} = J\frac{i\sqrt{2S}}{2} \sum_{\langle nm,ij\rangle} \Bigg[& \left(\rho_{ij} - \xi_{ij} - \rho_j + \frac{1}{4}\xi_i - \frac{1}{2}\rho_i\right)\left(a_{i,n} - a_{i,n}^{\dagger}\right) \\
& - \left(\rho_{ji} - \xi_{ji} - \rho_i + \frac{1}{4}\xi_j - \frac{1}{2}\rho_j\right)\left(a_{j,m} - a_{j,m}^{\dagger}\right)\Bigg] \sin\theta_{ij} \\
+ J_c\frac{i\sqrt{2S}}{2} \sum_{\langle nn',ii'\rangle} \Bigg[& \left(\rho_{ii'} - \xi_{ii'} - \rho_{i'} + \frac{1}{4}\xi_i - \frac{1}{2}\rho_i\right)\left(a_{i,n} - a_{i,n}^{\dagger}\right) \\
& - \left(\rho_{i'i} - \xi_{i'i} - \rho_i + \frac{1}{4}\xi_{i'} - \frac{1}{2}\rho_{i'}\right)\left(a_{i',n'} - a_{i',n'}^{\dagger}\right)\Bigg] \sin\theta_{ii'} \\
- g\mu_{\text{B}}H\frac{i\sqrt{2S}}{2}\frac{1}{4S} \sum_{n,i} & (\xi_i - 2\rho_i)(a_{i,n} - a_{i,n}^{\dagger}) \sin\theta_{\text{ih}},
\end{aligned} \tag{5.105}$$

This acts as a correction to $\mathcal{H}^{(1)}$. Thus the new ground state will require $\mathcal{H}_{\text{HF}}^{(3)} + \mathcal{H}^{(1)}$ to vanish, which yields a new set of angles between all spins in the extended cell.

Taking $a_{1,n}$ as an example, the coefficient in front of it,

$$\begin{aligned}
&3J\left[\frac{1}{S}\left(\rho_{12}-\xi_{12}-\frac{3\rho_1}{4}-\frac{3\rho_2}{4}+\frac{\xi_1}{8}+\frac{\xi_2}{8}\right)+1\right]\sin\theta_{12} \\
&+3J\left[\frac{1}{S}\left(\rho_{13}-\xi_{13}-\frac{3\rho_1}{4}-\frac{3\rho_3}{4}+\frac{\xi_1}{8}+\frac{\xi_3}{8}\right)+1\right]\sin\theta_{13} \\
&+2J_c\left[\frac{1}{S}\left(\rho_{14}-\xi_{14}-\frac{3\rho_1}{4}-\frac{3\rho_4}{4}+\frac{\xi_1}{8}+\frac{\xi_4}{8}\right)+1\right]\sin\theta_{14} \\
&-g\mu_{\mathrm{B}}H\left[\frac{1}{4S}\left(\xi_1-2\rho_1\right)+1\right]\sin\theta_{1\mathrm{h}},
\end{aligned} \tag{5.106}$$

has to be zero. As a result, there are six equations in total that are sufficient for solving six angles $\{\theta_i\}$.

It is not difficult to see this is equivalent to minimizing a corrected ground state energy function,

$$\begin{aligned}
E^{(0)}+\delta E^{(3)}_{\mathrm{HF}} = JS^2\sum_{\langle nm,ij\rangle}&\left[\frac{1}{S}\left(\rho_{ij}-\xi_{ij}-\frac{3\rho_i}{4}-\frac{3\rho_j}{4}+\frac{\xi_i}{8}+\frac{\xi_j}{8}\right)+1\right]\cos\theta_{ij} \\
+J_cS^2\sum_{\langle nn',ii'\rangle}&\left[\frac{1}{S}\left(\rho_{ii'}-\xi_{ii'}-\frac{3\rho_i}{4}-\frac{3\rho_{i'}}{4}+\frac{\xi_i}{8}+\frac{\xi_{i'}}{8}\right)+1\right]\cos\theta_{ii'} \\
-g\mu_{\mathrm{B}}HS\sum_{n,i}&\left[\frac{1}{4S}(\xi_i-2\rho_i)+1\right]\cos\theta_{i\mathrm{h}},
\end{aligned} \tag{5.107}$$

with respect to those angles where spins are still confined in the easy plane. It is more straightforward to see in this way that the correction is in the $1/S$ order.

Like before, these renormalized angles will give $\varepsilon^{(3)}_{\alpha,\mathbf{k}}$ which is part of the self-energies Σ_{HF} from Hartree-Fock correction.

Now the same method can be applied to $\mathcal{H}^{(4)}$ for the quadratic part $\mathcal{H}^{(4)}_{\mathrm{HF}}$. After proper simplification and Fourier transform, $\mathcal{H}^{(4)}_{\mathrm{HF}}$ can be written in the form of Equation (5.84) as the following

$$\mathcal{H}^{(4)}_{\mathrm{HF}} = 3JS\sum_{\mathbf{k}} a^\dagger_{i,\mathbf{k}}\delta A^{ij}_{\mathbf{k}}a_{j,\mathbf{k}} - \frac{1}{2}(a^\dagger_{i,\mathbf{k}}\delta B^{ij}_{\mathbf{k}}a^\dagger_{j,-\mathbf{k}}+\mathrm{h.c.}), \tag{5.108}$$

where the diagonal terms

$$\delta A^{ii}_{\mathbf{k}} = \frac{1}{2S}\sum_j \left[\xi_{ij}(\cos\theta_{ij}-\Delta)+\rho_{ij}(\cos\theta_{ij}+\Delta)+2\rho_j\cos\theta_{ij}\right] + \frac{\alpha}{3S}\left[\xi_{ii'}(\cos\theta_{ii'}-\Delta)+\rho_{ii'}(\cos\theta_{ii'}+\Delta)+2\rho'_i\cos\theta_{ii'}\right], \tag{5.109}$$

$$\delta B^{ii}_{\mathbf{k}} = \frac{1}{4S}\sum_j \left[\rho_{ij}(\cos\theta_{ij}-\Delta)+\xi_{ij}(\cos\theta_{ij}+\Delta)\right] + \frac{\alpha}{6S}\left[\rho_{ii'}(\cos\theta_{ii'}-\Delta)+\xi_{ii'}(\cos\theta_{ii'}+\Delta)\right], \tag{5.110}$$

and the off-diagonal terms

$$\delta A^{ij}_{\mathbf{k}} = \frac{1}{8S}\gamma_{ij}(\mathbf{k})\left[\xi_j(\cos\theta_{ij}-\Delta)+2\rho_j(\cos\theta_{ij}+\Delta)+8\rho_{ij}\cos\theta_{ij}\right], \tag{5.111}$$

$$\delta B^{ij}_{\mathbf{k}} = \frac{1}{8S}\gamma_{ij}(\mathbf{k})\left[2\rho_j(\cos\theta_{ij}-\Delta)+\xi_j(\cos\theta_{ij}+\Delta)+8\xi_{ij}\cos\theta_{ij}\right], \tag{5.112}$$

$$\delta A^{ii'}_{\mathbf{k}} = \frac{\alpha}{12S}\gamma_{ii'}(\mathbf{k})\left[\xi_{i'}(\cos\theta_{ii'}-\Delta)+2\rho_{i'}(\cos\theta_{ii'}+\Delta)+8\rho_{ii'}\cos\theta_{ii'}\right], \tag{5.113}$$

$$\delta B^{ii'}_{\mathbf{k}} = \frac{\alpha}{12S}\gamma_{ii'}(\mathbf{k})\left[2\rho_{i'}(\cos\theta_{ii'}-\Delta)+\Delta_{i'}(\cos\theta_{ii'}+\Delta)+8\xi_{ii'}\cos\theta_{ii'}\right], \tag{5.114}$$

where j represents the nearest neighbor site and i' the inter-layer coupled site.

The above terms will yield $\varepsilon^{(4)}_{\alpha,\mathbf{k}}$, the second part of Σ_{HF}.

Now it is time to look at the three-magnon interactions. Below is the cubic Hamiltonian

in momentum space.

$$\begin{aligned}\mathcal{H}^{(3)} = \frac{2J}{\sqrt{N}}\frac{i\sqrt{2S}}{2}\sum_{<ij>}\sum_{\mathbf{k},\mathbf{q}}\Big\{\gamma_{ij}(\mathbf{k}-\mathbf{q})\left(a^\dagger_{i,\mathbf{k}}a_{i,\mathbf{q}}a_{j,\mathbf{k}-\mathbf{q}} - a^\dagger_{i,\mathbf{k}}a_{i,\mathbf{q}}a^\dagger_{j,-\mathbf{k}+\mathbf{q}}\right) \\ +\frac{1}{8}\left(a^\dagger_{i,\mathbf{k}}a^\dagger_{i,\mathbf{q}}a_{i,\mathbf{k}+\mathbf{q}} - a^\dagger_{i,\mathbf{k}}a_{i,\mathbf{q}}a_{i,\mathbf{k}-\mathbf{q}}\right)\Big\}\cos\theta_{ij} \\ \frac{2J_c}{\sqrt{N}}\frac{i\sqrt{2S}}{2}\sum_{<ii'>}\sum_{\mathbf{k},\mathbf{q}}\Big\{\cos(k_z-q_z)\pi\left(a^\dagger_{i,\mathbf{k}}a_{i,\mathbf{q}}a_{i',\mathbf{k}-\mathbf{q}} - a^\dagger_{i,\mathbf{k}}a_{i,\mathbf{q}}a^\dagger_{i',-\mathbf{k}+\mathbf{q}}\right) \\ +\frac{1}{8}\left(a^\dagger_{i,\mathbf{k}}a^\dagger_{i,\mathbf{q}}a_{i,\mathbf{k}+\mathbf{q}} - a^\dagger_{i,\mathbf{k}}a_{i,\mathbf{q}}a_{i,\mathbf{k}-\mathbf{q}}\right)\Big\}\sin\theta_{ii'} \\ +\frac{g\mu_{\mathrm{B}}H}{4S\sqrt{N}}\frac{i\sqrt{2S}}{2}\sum_i\sum_{\mathbf{k},\mathbf{q}}(a^\dagger_{i,\mathbf{k}}a_{i,\mathbf{q}}a_{i,\mathbf{k}-\mathbf{q}} - a^\dagger_{i,\mathbf{k}}a^\dagger_{i,\mathbf{q}}a_{i,\mathbf{k}+\mathbf{q}})\sin\theta_{i\mathrm{h}}.\end{aligned} \tag{5.115}$$

Here $\{ij\}$ is summed over the nearest neighbor sites considering (*e.g.*, $\{1,2\}$ counts 3 times and $\{1,2\}$ and $\{2,1\}$ both count). $\{ii'\}$ indicating inter-plane coupling follows the same fashion.

$\mathcal{H}^{(3)}$ can be separated into the decay vertices $\hat{V}_3^{(1)}$ and source vertices $\hat{V}_3^{(2)}$. With the Bogolubov transformation, they have the following general expressions.

$$\hat{V}_3^{(1)} = \frac{1}{2!}\sum_{\mathbf{k},\mathbf{q}}\left[\Gamma_1^{\alpha\beta\eta}(\mathbf{k},-\mathbf{q};\mathbf{k}-\mathbf{q})b^\dagger_{\alpha,\mathbf{k}}b^\dagger_{\beta,-\mathbf{q}}b_{\eta,\mathbf{k}-\mathbf{q}} + \mathrm{h.c.}\right], \tag{5.116}$$

$$\hat{V}_3^{(2)} = \frac{1}{3!}\sum_{\mathbf{k},\mathbf{q}}\left[\Gamma_2^{\alpha\beta\eta}(\mathbf{k},-\mathbf{q};-\mathbf{k}+\mathbf{q})b^\dagger_{\alpha,\mathbf{k}}b^\dagger_{\beta,-\mathbf{q}}b^\dagger_{\eta,-\mathbf{k}+\mathbf{q}} + \mathrm{h.c.}\right], \tag{5.117}$$

where α, β and η are implicitly summed over all six magnons.

The factor $1/2!$ in $\hat{V}_3^{(1)}$ is due to its invariance under permutation of $\{\alpha,\mathbf{k}\}$ and $\{\beta,-\mathbf{q}\}$. Likewise, $1/3!$ in $\hat{V}_3^{(2)}$ comes from the invariance under permutation of all three magnon and momentum pairs. $\Gamma_1^{\alpha\beta\eta}(\mathbf{k},-\mathbf{q};\mathbf{k}-\mathbf{q})$ and $\Gamma_2^{\alpha\beta\eta}(\mathbf{k},-\mathbf{q};-\mathbf{k}+\mathbf{q})$ can be expressed in terms of $\mathbf{U_q}$ and $\mathbf{V_q}$ from the Bogolubov transformation.

$$\Gamma_1^{\alpha\beta\eta}(\mathbf{k},-\mathbf{q};\mathbf{k}-\mathbf{q}) = \frac{J}{\sqrt{N}}\frac{i\sqrt{2S}}{2}\sum_{<ij>}\Big\{\gamma_{ij}(-\mathbf{k})\left(V_{-\mathbf{k}}^{j\alpha}-U_{-\mathbf{k}}^{j\alpha}\right)\left(V_{\mathbf{q}}^{i\beta}V_{\mathbf{k}-\mathbf{q}}^{i\eta}+U_{\mathbf{q}}^{i\beta}U_{\mathbf{k}-\mathbf{q}}^{i\eta}\right)$$

$$+\gamma_{ij}(\mathbf{q})\left(V_{\mathbf{q}}^{j\beta}-U_{\mathbf{q}}^{j\beta}\right)\left(V_{-\mathbf{k}}^{i\alpha}V_{\mathbf{k}-\mathbf{q}}^{i\eta}+U_{-\mathbf{k}}^{i\alpha}U_{\mathbf{k}-\mathbf{q}}^{i\eta}\right)$$

$$-\gamma_{ij}(\mathbf{k}-\mathbf{q})\left(V_{\mathbf{k}-\mathbf{q}}^{j\eta}-U_{\mathbf{k}-\mathbf{q}}^{j\eta}\right)\left(U_{-\mathbf{k}}^{i\alpha}V_{\mathbf{q}}^{i\beta}+V_{-\mathbf{k}}^{i\alpha}U_{\mathbf{q}}^{i\beta}\right)$$

$$+\frac{1}{4}\Big[\left(U_{-\mathbf{k}}^{i\alpha}-V_{-\mathbf{k}}^{i\alpha}\right)\left(V_{\mathbf{q}}^{i\beta}V_{\mathbf{k}-\mathbf{q}}^{i\eta}+U_{\mathbf{q}}^{i\beta}U_{\mathbf{k}-\mathbf{q}}^{i\eta}\right)+\left(U_{\mathbf{q}}^{i\beta}-V_{\mathbf{q}}^{i\beta}\right)\left(V_{-\mathbf{k}}^{i\alpha}V_{\mathbf{k}-\mathbf{q}}^{i\eta}+U_{-\mathbf{k}}^{i\alpha}U_{\mathbf{k}-\mathbf{q}}^{i\eta}\right)$$

$$-\left(U_{\mathbf{k}-\mathbf{q}}^{i\eta}-V_{\mathbf{k}-\mathbf{q}}^{i\eta}\right)\left(U_{-\mathbf{k}}^{i\alpha}V_{\mathbf{q}}^{i\beta}+V_{-\mathbf{k}}^{i\alpha}U_{\mathbf{q}}^{i\beta}\right)\Big]\Big\}\sin\theta_{ij}$$

$$+\frac{J_c}{\sqrt{N}}\frac{i\sqrt{2S}}{2}\sum_{<ii'>}\Big\{\gamma_{ii'}(-\mathbf{k})\left(V_{-\mathbf{k}}^{i'\alpha}-U_{-\mathbf{k}}^{i'\alpha}\right)\left(V_{\mathbf{q}}^{i\beta}V_{\mathbf{k}-\mathbf{q}}^{i\eta}+U_{\mathbf{q}}^{i\beta}U_{\mathbf{k}-\mathbf{q}}^{i\eta}\right)$$

$$+\gamma_{ii'}(\mathbf{q})\left(V_{\mathbf{q}}^{i'\beta}-U_{\mathbf{q}}^{i'\beta}\right)\left(V_{-\mathbf{k}}^{i\alpha}V_{\mathbf{k}-\mathbf{q}}^{i\eta}+U_{-\mathbf{k}}^{i\alpha}U_{\mathbf{k}-\mathbf{q}}^{i\eta}\right)$$

$$-\gamma_{ii'}(\mathbf{k}-\mathbf{q})\left(V_{\mathbf{k}-\mathbf{q}}^{i'\eta}-U_{\mathbf{k}-\mathbf{q}}^{i'\eta}\right)\left(U_{-\mathbf{k}}^{i\alpha}V_{\mathbf{q}}^{i\beta}+V_{-\mathbf{k}}^{i\alpha}U_{\mathbf{q}}^{i\beta}\right)$$

$$+\frac{1}{4}\Big[\left(U_{-\mathbf{k}}^{i\alpha}-V_{-\mathbf{k}}^{i\alpha}\right)\left(V_{\mathbf{q}}^{i\beta}V_{\mathbf{k}-\mathbf{q}}^{i\eta}+U_{\mathbf{q}}^{i\beta}U_{\mathbf{k}-\mathbf{q}}^{i\eta}\right)+\left(U_{\mathbf{q}}^{i\beta}-V_{\mathbf{q}}^{i\beta}\right)\left(V_{-\mathbf{k}}^{i\alpha}V_{\mathbf{k}-\mathbf{q}}^{i\eta}+U_{-\mathbf{k}}^{i\alpha}U_{\mathbf{k}-\mathbf{q}}^{i\eta}\right)$$

$$-\left(U_{\mathbf{k}-\mathbf{q}}^{i\eta}-V_{\mathbf{k}-\mathbf{q}}^{i\eta}\right)\left(U_{-\mathbf{k}}^{i\alpha}V_{\mathbf{q}}^{i\beta}+V_{-\mathbf{k}}^{i\alpha}U_{\mathbf{q}}^{i\beta}\right)\Big]\Big\}\sin\theta_{ii'}$$

$$+\frac{g\mu_{\mathrm{B}}H}{4S\sqrt{N}}\frac{i\sqrt{2S}}{2}$$

$$\sum_i\Big[\left(V_{-\mathbf{k}}^{i\alpha}-U_{-\mathbf{k}}^{i\alpha}\right)\left(V_{\mathbf{q}}^{i\beta}V_{\mathbf{k}-\mathbf{q}}^{i\eta}+U_{\mathbf{q}}^{i\beta}U_{\mathbf{k}-\mathbf{q}}^{i\eta}\right)$$

$$+\left(V_{\mathbf{q}}^{i\beta}-U_{\mathbf{q}}^{i\beta}\right)\left(V_{-\mathbf{k}}^{i\alpha}V_{\mathbf{k}-\mathbf{q}}^{i\eta}+U_{-\mathbf{k}}^{i\alpha}U_{\mathbf{k}-\mathbf{q}}^{i\eta}\right)$$

$$-\left(V_{\mathbf{k}-\mathbf{q}}^{i\eta}-U_{\mathbf{k}-\mathbf{q}}^{i\eta}\right)\left(U_{-\mathbf{k}}^{i\alpha}V_{\mathbf{q}}^{i\beta}+V_{-\mathbf{k}}^{i\alpha}U_{\mathbf{q}}^{i\beta}\right)\Big]\sin\theta_{i\mathrm{h}}, \tag{5.118}$$

$$
\begin{aligned}
\Gamma_2^{\alpha\beta\eta}(\mathbf{k},-\mathbf{q};-\mathbf{k}+\mathbf{q}) = \frac{J}{\sqrt{N}}\frac{i\sqrt{2S}}{2}\sum_{ij}\Big\{&\gamma_{ij}(-\mathbf{k})\left(V_{-\mathbf{k}}^{j\alpha}-U_{-\mathbf{k}}^{j\alpha}\right)\left(U_{\mathbf{q}}^{i\beta}V_{\mathbf{k}-\mathbf{q}}^{i\eta}+U_{\mathbf{k}-\mathbf{q}}^{i\eta}V_{\mathbf{q}}^{i\beta}\right)\\
&+\gamma_{ij}(\mathbf{q})\left(V_{\mathbf{q}}^{j\beta}-U_{\mathbf{q}}^{j\beta}\right)\left(U_{\mathbf{k}-\mathbf{q}}^{i\eta}V_{-\mathbf{k}}^{i\alpha}+U_{-\mathbf{k}}^{i\alpha}V_{\mathbf{k}-\mathbf{q}}^{i\eta}\right)\\
&+\gamma_{ij}(\mathbf{k}-\mathbf{q})\left(V_{\mathbf{k}-\mathbf{q}}^{j\eta}-U_{\mathbf{k}-\mathbf{q}}^{j\eta}\right)\left(U_{-\mathbf{k}}^{i\alpha}V_{\mathbf{q}}^{i\beta}+U_{\mathbf{q}}^{i\beta}V_{-\mathbf{k}}^{i\alpha}\right)\\
&+\frac{1}{4}\Big[\left(U_{-\mathbf{k}}^{i\alpha}-V_{-\mathbf{k}}^{i\alpha}\right)\left(U_{\mathbf{q}}^{i\beta}V_{\mathbf{k}-\mathbf{q}}^{i\eta}+U_{\mathbf{k}-\mathbf{q}}^{i\eta}V_{\mathbf{q}}^{i\beta}\right)+\left(U_{\mathbf{q}}^{i\beta}-V_{\mathbf{q}}^{i\beta}\right)\left(U_{\mathbf{k}-\mathbf{q}}^{i\eta}V_{-\mathbf{k}}^{i\alpha}+U_{-\mathbf{k}}^{i\alpha}V_{\mathbf{k}-\mathbf{q}}^{i\eta}\right)\\
&+\left(U_{\mathbf{k}-\mathbf{q}}^{i\eta}-V_{\mathbf{k}-\mathbf{q}}^{i\eta}\right)\left(U_{-\mathbf{k}}^{i\alpha}V_{\mathbf{q}}^{i\beta}+U_{\mathbf{q}}^{i\beta}V_{-\mathbf{k}}^{i\alpha}\right)\Big)\Big\}\sin\theta_{ij}\\
&+\frac{J_c}{\sqrt{N}}\frac{i\sqrt{2S}}{2}\sum_{ii'}\Big\{\gamma_{ii'}(-\mathbf{k})\left(V_{-\mathbf{k}}^{i'\alpha}-U_{-\mathbf{k}}^{i'\alpha}\right)\left(U_{\mathbf{q}}^{i\beta}V_{\mathbf{k}-\mathbf{q}}^{i\eta}+U_{\mathbf{k}-\mathbf{q}}^{i\eta}V_{\mathbf{q}}^{i\beta}\right)\\
&+\gamma_{ii'}(\mathbf{q})\left(V_{\mathbf{q}}^{i'\beta}-U_{\mathbf{q}}^{i'\beta}\right)\left(U_{\mathbf{k}-\mathbf{q}}^{i\eta}V_{-\mathbf{k}}^{i\alpha}+U_{-\mathbf{k}}^{i\alpha}V_{\mathbf{k}-\mathbf{q}}^{i\eta}\right)\\
&+\gamma_{ii'}(\mathbf{k}-\mathbf{q})\left(V_{\mathbf{k}-\mathbf{q}}^{i'\eta}-U_{\mathbf{k}-\mathbf{q}}^{i'\eta}\right)\left(U_{-\mathbf{k}}^{i\alpha}V_{\mathbf{q}}^{i\beta}+U_{\mathbf{q}}^{i\beta}V_{-\mathbf{k}}^{i\alpha}\right)\\
&+\frac{1}{4}\Big[\left(U_{-\mathbf{k}}^{i\alpha}-V_{-\mathbf{k}}^{i\alpha}\right)\left(U_{\mathbf{q}}^{i\beta}V_{\mathbf{k}-\mathbf{q}}^{i\eta}+U_{\mathbf{k}-\mathbf{q}}^{i\eta}V_{\mathbf{q}}^{i\beta}\right)+\left(U_{\mathbf{q}}^{i\beta}-V_{\mathbf{q}}^{i\beta}\right)\left(U_{\mathbf{k}-\mathbf{q}}^{i\eta}V_{-\mathbf{k}}^{i\alpha}+U_{-\mathbf{k}}^{i\alpha}V_{\mathbf{k}-\mathbf{q}}^{i\eta}\right)\\
&+\left(U_{\mathbf{k}-\mathbf{q}}^{i\eta}-V_{\mathbf{k}-\mathbf{q}}^{i\eta}\right)\left(U_{-\mathbf{k}}^{i\alpha}V_{\mathbf{q}}^{i\beta}+U_{\mathbf{q}}^{i\beta}V_{-\mathbf{k}}^{i\alpha}\right)\Big)\Big\}\sin\theta_{ii'}\\
&+\frac{g\mu_{\mathrm{B}}H}{4S\sqrt{N}}\frac{i\sqrt{2S}}{2}\sum_{i}\Big[\left(V_{-\mathbf{k}}^{i\alpha}-U_{-\mathbf{k}}^{i\alpha}\right)\left(U_{\mathbf{q}}^{i\beta}V_{\mathbf{k}-\mathbf{q}}^{i\eta}+U_{\mathbf{k}-\mathbf{q}}^{i\eta}V_{\mathbf{q}}^{i\beta}\right)\\
&+\left(V_{\mathbf{q}}^{i\beta}-U_{\mathbf{q}}^{i\beta}\right)\left(U_{\mathbf{k}-\mathbf{q}}^{i\eta}V_{-\mathbf{k}}^{i\alpha}+U_{-\mathbf{k}}^{i\alpha}V_{\mathbf{k}-\mathbf{q}}^{i\eta}\right)\\
&+\left(V_{\mathbf{k}-\mathbf{q}}^{i\eta}-U_{\mathbf{k}-\mathbf{q}}^{i\eta}\right)\left(U_{-\mathbf{k}}^{i\alpha}V_{\mathbf{q}}^{i\beta}+U_{\mathbf{q}}^{i\beta}V_{-\mathbf{k}}^{i\alpha}\right)\Big]\sin\theta_{\mathrm{ih}},
\end{aligned}
\tag{5.119}
$$

where $\gamma_{ii'}(\mathbf{k}) \equiv \cos k_z\pi$.

Like wise, the self-energies in the order of $\mathcal{O}(1/S)$ are

$$
\Sigma_{11}^{(a),\alpha}(\mathbf{k},\varepsilon) = \sum_{\mathbf{q},\beta\eta}\frac{\left|\Gamma_1^{\alpha\beta\eta}(\mathbf{q},\mathbf{k}-\mathbf{q};\mathbf{k})\right|^2}{\varepsilon-\varepsilon_{\beta,\mathbf{q}}-\varepsilon_{\eta,\mathbf{k}-\mathbf{q}}+i0_+}, \tag{5.120}
$$

$$
\Sigma_{11}^{(b),\alpha}(\mathbf{k},\varepsilon) = -\sum_{\mathbf{q},\beta\eta}\frac{\left|\Gamma_2^{\alpha\beta\eta}(\mathbf{q},-\mathbf{k}-\mathbf{q},\mathbf{k})\right|^2}{\varepsilon+\varepsilon_{\beta,\mathbf{q}}+\varepsilon_{\eta,-\mathbf{k}-\mathbf{q}}-i0_+}, \tag{5.121}
$$

and $\mathrm{Im}\Sigma_{11}^{(a),\alpha}(\mathbf{k},\varepsilon_{\alpha,\mathbf{k}})$ yields the on-shell two-magnon decay rate for the α's magnon mode.

At this point, all terms needed for $1/S$ correction have been prepared. In principle,

one could apply all those corrections as the overall magnon self-energies and calculate the spectral functions for all six magnon modes.

For a qualitative estimate of the two-magnon decays, one could actually calculate the overlaps between the one-magnon and two-magnon density of states. In practice, one just need to compare the one-magnon poles and the two-magnon density of states which is defined as

$$\mathcal{D}_2^{ij}(\mathbf{k},\varepsilon) = \sum_{\mathbf{q}} \delta(\varepsilon - \varepsilon_{i,\mathbf{q}} - \varepsilon_{j,\mathbf{k}-\mathbf{q}}) = \int \frac{\mathrm{d}^3 q}{8\pi^3} \delta(\varepsilon - \varepsilon_{i,\mathbf{q}} - \varepsilon_{j,\mathbf{k}-\mathbf{q}}), \tag{5.122}$$

Ideally, this can be transformed into

$$\mathcal{D}_2^{ij}(\mathbf{k},\varepsilon) = \frac{1}{8\pi^3} \oint \frac{\mathrm{d}l}{\nabla_{\mathbf{q}}(\varepsilon_{i,\mathbf{q}} + \varepsilon_{j,\mathbf{k}-\mathbf{q}})}. \tag{5.123}$$

When analytic expressions for the dispersions are not achievable, the delta function in Equation (5.122) can be written into the Lorentzian function,

$$\mathcal{D}_2^{ij}(\mathbf{k},\varepsilon) = \frac{1}{8\pi^3} \int \mathrm{d}^3 q \frac{1}{\pi} \frac{\gamma}{(\varepsilon - \varepsilon_{i,\mathbf{q}} - \varepsilon_{j,\mathbf{k}-\mathbf{q}})^2 + \gamma^2}, \tag{5.124}$$

and eases the numerical evaluation.

5.3 Conclusions

As the zero-field spin dynamics were reviewed where the spin-wave theory tragically failed to capture the vanishing excitations above $E \sim 1.6$ meV as well as the 3.5 meV mode around M points. Various in-field studies were carried out to examine the system's magnetic excitations in different phases in order to answer two questions. The first one is whether the quasi-2D spin Hamiltonian with easy-plane anisotropy is sufficient. The second one is how far the spin-wave theory can go in terms of describing the spin dynamics.

It turns out that the magnetic excitations in the plateau phase well fit into a semiclassi-

cal spin-wave picture and a reliable spin Hamiltonian was unambiguously extracted from matching the experimental spectra using a modified nonlinear spin-wave technique.

More experiments were conducted in the "umbrella" phase and the low-field co-planar phase. And the corresponding spin-wave calculation was performed based on the extracted spin Hamiltonian.

In the "umbrella" case where a detailed spin-wave calculation with $1/S$ correction was carried out. It was shown that while the simulation is not able to fully describe the experimental data, the observed high-energy mode does support the decay picture.

The data in the low-field co-planar state was able to provide a very detailed view of the field-dependence of the excitation modes as they transform from the "mysterious" zero-field case to the well-defined UUD one. Very interesting behavior was spotted, implying some threshold field between 4 and 6 T. Meanwhile, the overall excitation spectra escape the linear spin-wave picture. Some $1/S$ work was demonstrated without actual simulation which is unfeasible.

More neutron scattering experiments in those explored or unexplored phases with improved energy and momentum space coverage will be challenging but extremely beneficial. For instance, coverage of the $(h, k, 1)$ plane with energy transfer reaching at least 5 meV for the "umbrella" phase will allow a direct comparison with the zero-field dynamics with the Goldstone mode and help tremendously.

From the theoretical perspective, the current limit of the spin-wave theory has been nearly reached and more analytical or numerical techniques are demanded to reveal the full microscopic picture of the system. There is notably some success from the 2D DMRG simulation [98] where the local-minimum behavior of the M point dispersion was correctly predicted. However, it is necessary to point out that Ref. [98] wrongly stated that such behavior was consistent with spin-wave theory and also inappropriately dismissed other unresolved features from this compound such as the presence of the 3.5 meV mode. Apart from DMRG, there is recent progress by VMC simulations [99]. While the energy resolu-

tion is not yet sufficient to unequivocally distinguish one-magnon poles and continuum, it has become a promising method to study spin dynamics effectively.

CHAPTER 6

OUTLOOK

Localized spin systems are very important toy models for studies on many-body quantum problems. The platform provided by $3d$ transition metal oxides realizing these spin systems is the integral part to understanding the nature of magnetic excitations. Equipped with inelastic neutron scattering technique and spin-wave theory, this thesis has presented detailed work on a series of materials with different effective magnetic Hamiltonian dimensions so as to answer how universal the magnon paradigm is in describing the fundamental excitations of those systems or to what extent they remain effective.

Studies on diamond lattices, $CoRh_2O_4$ and $CuRh_2O_4$, showcase the stereotypical success of the spin-wave theory in benchmarking the magnetic excitations in real materials. Spontaneous symmetry breaking naturally happens at finite temperatures for 3D systems and leads to a well-defined condensate of magnons as well as the magnonic excitation. Remarkably, with the combination of various experimental and theoretical tools such as neutron diffraction and mean-field theory, a detailed microscopic understanding is obtained from just the powder-averaged inelastic neutron spectra.

Lacking the experimental evidence of an order parameter down to $T = 30$ mK, the frustrated ferromagnetic spin-1/2 chain, $LiCuSbO_4$, had been regarded as a candidate to realize quantum spin liquid [61]. This is certainly a case where no one would intuitively anticipate the effectiveness of spin-wave theory. Yet it works surprisingly and remarkably well by obtaining a spin Hamiltonian which captures all the features in the inelastic neutron data, which is again powder-averaged data. Moreover, this microscopic understanding is significantly strengthened as it coheres with the thermodynamics properties simulated with tensor network techniques. The calculations on the simplified effective spin-one model are

also qualitatively consistent with the inelastic neutron data with applied magnetic field as well as with effect from the inter-chain coupling.

The quasi-2D spin-1/2 triangular antiferromagnet, $Ba_3CoSb_2O_9$, in contrast, exhibits some mysterious zero-field spin dynamics that spin-wave theory fails to fully account for. However, the investigation on the UUD phase offers an effective spin Hamiltonian that is later used to examine the system's behavior in the "umbrella" phase and low-field co-planar phase. While spin-wave theory fails to offer a completely satisfying description, it is observed to become more effective in higher fields and the data potentially validates the predictions for field-induced magnon-decay. Overall, the observed discrepancies still awaits further experimental and theoretical investigation to be fully resolved.

Originating from strongly correlated electrons, the microscopic details of spin systems cannot be reliably predicted from first-principle techniques. Therefore, detailed benchmarking is rather important to narrow down the number of possible scenarios especially when a few of them seem valid at the same time. It is the advancement of the inelastic neutron scattering technique that has made such benchmarking possible. Meanwhile, scientific research involves ceaseless innovations on top of the routine tools. While spin-wave theory is not something brand new, using it wisely along with proper treatment of the data can often lead to new and inspirational understandings of magnetic materials. Those understandings may hopefully extend to the entire field of quantum many-body physics.

REFERENCES

[1] J. Hubbard, "Electron correlations in narrow energy bands", Proceedings of the Royal Society of London. Series A. Mathematical and Physical Sciences **276**, 238–257 (1963).

[2] A. Auerbach, *Interacting electrons and quantum magnetism* (Springer Science & Business Media, 2012).

[3] J. Tranquada, B. Sternlieb, J. Axe, Y Nakamura, and S Uchida, "Evidence for stripe correlations of spins and holes in copper oxide superconductors", Nature **375**, 561 (1995).

[4] N. R. Council et al., *High magnetic field science and its application in the united states: current status and future directions* (National Academies Press, 2013).

[5] L. Landau and E. Lifshitz, "On the theory of the dispersion of magnetic permeability in ferromagnetic bodies", in *Perspectives in theoretical physics* (Elsevier, 1992), pp. 51–65.

[6] T. Holstein and H. Primakoff, "Field dependence of the intrinsic domain magnetization of a ferromagnet", Phys. Rev. **58**, 1098–1113 (1940).

[7] A. L. Chernyshev and M. E. Zhitomirsky, "Magnon decay in noncollinear quantum antiferromagnets", Phys. Rev. Lett. **97**, 207202 (2006).

[8] A. L. Chernyshev and M. E. Zhitomirsky, "Spin waves in a triangular lattice antiferromagnet: decays, spectrum renormalization, and singularities", Phys. Rev. B **79**, 144416 (2009).

[9] M. Mourigal, M. E. Zhitomirsky, and A. L. Chernyshev, "Field-induced decay dynamics in square-lattice antiferromagnets", Phys. Rev. B **82**, 144402 (2010).

[10] N. B. Christensen, H. M. Rønnow, D. F. McMorrow, A Harrison, T. Perring, M. Enderle, R Coldea, L. Regnault, and G Aeppli, "Quantum dynamics and entanglement of spins on a square lattice", Proceedings of the National Academy of Sciences **104**, 15264–15269 (2007).

[11] N Tsyrulin, T Pardini, R. Singh, F Xiao, P Link, A Schneidewind, A Hiess, C. Landee, M. Turnbull, and M Kenzelmann, "Quantum effects in a weakly frustrated $S = 1/2$ two-dimensional heisenberg antiferromagnet in an applied magnetic field", Physical review letters **102**, 197201 (2009).

[12] N. Headings, S. Hayden, R Coldea, and T. Perring, "Anomalous high-energy spin excitations in the high-T_c superconductor-parent antiferromagnet La_2CuO_4", Physical review letters **105**, 247001 (2010).

[13] K. Plumb, A. T. Savici, G. E. Granroth, F. Chou, and Y.-J. Kim, "High-energy continuum of magnetic excitations in the two-dimensional quantum antiferromagnet $Sr_2CuO_2Cl_2$", Physical Review B **89**, 180410 (2014).

[14] B. Dalla Piazza, M Mourigal, N. B. Christensen, G. Nilsen, P Tregenna-Piggott, T. Perring, M. Enderle, D. F. McMorrow, D. Ivanov, and H. M. Rønnow, "Fractional excitations in the square-lattice quantum antiferromagnet", Nature physics **11**, 62 (2015).

[15] M Powalski, G. Uhrig, and K. Schmidt, "Roton minimum as a fingerprint of magnon-Higgs scattering in ordered quantum antiferromagnets", Physical review letters **115**, 207202 (2015).

[16] J. Chadwick, "Possible existence of a neutron", Nature **129**, 312–312 (1932).

[17] G. L. Squires, *Introduction to the theory of thermal neutron scattering* (Courier Corporation, 1996).

[18] S. W. Lovesey, "Theory of neutron scattering from condensed matter", (1984).

[19] A. Furrer, T. StrÃ, et al., *Neutron scattering in condensed matter physics* (World Scientific Publishing Company, 2009).

[20] T. Chatterji, *Neutron scattering from magnetic materials* (Elsevier, 2005).

[21] I. A. Zaliznyak and S.-H. Lee, "Magnetic neutron scattering.", in Spin, Vol. 5 (2005), p. 1.

[22] G. Shirane, S. M. Shapiro, and J. M. Tranquada, *Neutron scattering with a triple-axis spectrometer: basic techniques* (Cambridge University Press, 2002).

[23] G. Li, G. Bentoumi, Z. Tun, L. Li, and B. Sur, "Thermal neutron scattering cross-section measurements of heavy water", CNL Nuclear Review **6**, 47–53 (2017).

[24] J. Rodriguez, D. Adler, P. Brand, C. Broholm, J. Cook, C. Brocker, R. Hammond, Z. Huang, P. Hundertmark, J. Lynn, et al., "MACS - a new high intensity cold neutron spectrometer at NIST", Measurement Science and Technology **19**, 034023 (2008).

[25] M. B. Stone, J. L. Niedziela, D. L. Abernathy, L DeBeer-Schmitt, G Ehlers, O Garlea, G. Granroth, M Graves-Brook, A. I. Kolesnikov, A Podlesnyak, et al., "A comparison

of four direct geometry time-of-flight spectrometers at the spallation neutron source", Review of Scientific Instruments **85**, 045113 (2014).

[26] N. D. Mermin and H. Wagner, "Absence of ferromagnetism or antiferromagnetism in one-or two-dimensional isotropic heisenberg models", Physical Review Letters **17**, 1133 (1966).

[27] S. T. Bramwell and M. J. Gingras, "Spin ice state in frustrated magnetic pyrochlore materials", Science **294**, 1495–1501 (2001).

[28] J. S. Gardner, M. J. Gingras, and J. E. Greedan, "Magnetic pyrochlore oxides", Rev. Mod. Phys. **82**, 53 (2010).

[29] T Fennell, P. Deen, A. Wildes, K Schmalzl, D Prabhakaran, A. Boothroyd, R. Aldus, D. McMorrow, and S. Bramwell, "Magnetic Coulomb phase in the spin ice $Ho_2Ti_2O_7$", Science **326**, 415–417 (2009).

[30] K. A. Ross, L. Savary, B. D. Gaulin, and L. Balents, "Quantum excitations in quantum spin ice", Phys. Rev. X **1**, 021002 (2011).

[31] A. Krimmel, M. Mücksch, V. Tsurkan, M. M. Koza, H. Mutka, C. Ritter, D. V. Sheptyakov, S. Horn, and A. Loidl, "Magnetic ordering and spin excitations in the frustrated magnet $MnSc_2S_4$", Phys. Rev. B **73**, 014413 (2006).

[32] S. Gao, O. Zaharko, V. Tsurkan, Y. Su, J. S. White, G. S. Tucker, B. Roessli, F. Bourdarot, R. Sibille, D. Chernyshov, T. Fennell, A. Loidl, and C. Ruegg, "Spiral spin-liquid and the emergence of a vortex-like state in $MnSc_2S_4$", Nat. Phys. **13**, 157161 (2016).

[33] V. Fritsch, J. Hemberger, N. Büttgen, E.-W. Scheidt, H.-A. Krug von Nidda, A. Loidl, and V. Tsurkan, "Spin and orbital frustration in $MnSc_2S_4$ and $FeSc_2S_4$", Phys. Rev. Lett. **92**, 116401 (2004).

[34] A. Krimmel, M. Mücksch, V. Tsurkan, M. M. Koza, H. Mutka, and A. Loidl, "Vibronic and magnetic excitations in the spin-orbital liquid state of $FeSc_2S_4$", Phys. Rev. Lett. **94**, 237402 (2005).

[35] N. J. Laurita, J. Deisenhofer, L. Pan, C. M. Morris, M. Schmidt, M. Johnsson, V. Tsurkan, A. Loidl, and N. P. Armitage, "Singlet-triplet excitations and long-range entanglement in the spin-orbital liquid candidate $FeSc_2S_4$", Phys. Rev. Lett. **114**, 207201 (2015).

[36] L. Mittelstädt, M. Schmidt, Z. Wang, F. Mayr, V. Tsurkan, P. Lunkenheimer, D. Ish, L. Balents, J. Deisenhofer, and A. Loidl, "Spin-orbiton and quantum criticality in $FeSc_2S_4$", Phys. Rev. B **91**, 125112 (2015).

[37] K. W. Plumb, J. R. Morey, J. A. Rodriguez-Rivera, H. Wu, A. A. Podlesnyak, T. M. McQueen, and C. L. Broholm, "Antiferromagnetic and orbital ordering on a diamond lattice near quantum criticality", Phys. Rev. X **6**, 041055 (2016).

[38] A. Biffin, C. Rüegg, J. Embs, T. Guidi, D. Cheptiakov, A. Loidl, V. Tsurkan, and R. Coldea, "Magnetic field dependence of excitations near spin-orbital quantum criticality", Phys. Rev. Lett. **118**, 067205 (2017).

[39] T Suzuki, H Nagai, M Nohara, and H Takagi, "Melting of antiferromagnetic ordering in spinel oxide $CoAl_2O_4$", J. Phys. Condens. Matter **19**, 145265 (2007).

[40] G. J. MacDougall, D. Gout, J. L. Zarestky, G. Ehlers, A. Podlesnyak, M. A. McGuire, D. Mandrus, and S. E. Nagler, "Kinetically inhibited order in a diamond-lattice antiferromagnet", Proc. Natl. Acad. Sci. USA **108**, 15693–15698 (2011).

[41] O. Zaharko, S. Tóth, O. Sendetskyi, A. Cervellino, A. Wolter-Giraud, T. Dey, A. Maljuk, and V. Tsurkan, "Unconventional magnetic order in the frustrated diamond-lattice antiferromagnet $CoAl_2O_4$ studied by neutron diffraction and classical monte carlo simulation", Phys. Rev. B **90**, 134416 (2014).

[42] G. J. MacDougall, A. A. Aczel, Y. Su, W. Schweika, E. Faulhaber, A. Schneidewind, A. D. Christianson, J. L. Zarestky, H. D. Zhou, D. Mandrus, and S. E. Nagler, "Revisiting the ground state of $CoAl_2O_4$: comparison to the conventional antiferromagnet $MnAl_2O_4$", Phys. Rev. B.

[43] L. Ge, J. Flynn, J. A. M. Paddison, M. B. Stone, S. Calder, M. A. Subramanian, A. P. Ramirez, and M. Mourigal, "Spin order and dynamics in the diamond-lattice Heisenberg antiferromagnets $CuRh_2O_4$ and $CuRh_2O_4$", Phys. Rev. B **96**, 064413 (2017).

[44] G Blasse, "New type of superexchange", Philips Res. Repts **18**, 383–392 (1963).

[45] F Bertaut, F Forrat, and J Dulac, "Rhodites spinelles", Comptes Rendus Hebdomadaires des Seances de l'Academie des Sciences **249**, 726–728 (1959).

[46] A. Ramirez, "Strongly geometrically frustrated magnets", Annu. Rev. Mater. Sci. **24**, 453–480 (1994).

[47] S Toth and B Lake, "Linear spin wave theory for single-q incommensurate magnetic structures", J. Phys. Condens. Matter **27**, 166002 (2015).

[48] E. F. Bertaut, "Lattice theory of spin configuration", Journal of Applied Physics **33**, 1138–1143 (1962).

[49] L. C. Chapon, "Origin of the long-wavelength magnetic modulation in $Ca_3Co_2O_6$", Phys. Rev. B **80**, 172405 (2009).

[50] J. N. Reimers, A. J. Berlinsky, and A.-C. Shi, "Mean-field approach to magnetic ordering in highly frustrated pyrochlores", Phys. Rev. B **43**, 865–878 (1991).

[51] A. C. Genz and A. Malik, "Remarks on algorithm 006: an adaptive algorithm for numerical integration over an n-dimensional rectangular region", J. Comput. Phys. and Appl. Maths. **6**, 295–302 (1980).

[52] J. Berntsen, T. O. Espelid, and A. Genz, "An adaptive algorithm for the approximate calculation of multiple integrals", ACM Transactions on Mathematical Software (TOMS) **17**, 437–451 (1991).

[53] J.-I. Igarashi, "1/S expansion for thermodynamic quantities in a two-dimensional Heisenberg antiferromagnet at zero temperature", Phys. Rev. B **46**, 10763–10771 (1992).

[54] H. Bethe, "Zur theorie der metalle", Zeitschrift für Physik **71**, 205–226 (1931).

[55] B Lake, D. Tennant, J.-S. Caux, T Barthel, U Schollwöck, S. Nagler, and C. Frost, "Multispinon continua at zero and finite temperature in a near-ideal heisenberg chain", Physical review letters **111**, 137205 (2013).

[56] M. Mourigal, M. Enderle, A. Klöpperpieper, J.-S. Caux, A. Stunault, and H. M. Rønnow, "Fractional spinon excitations in the quantum heisenberg antiferromagnetic chain", Nature Physics **9**, 435 (2013).

[57] J. Sudan, A. Lüscher, and A. M. Läuchli, "Emergent multipolar spin correlations in a fluctuating spiral: the frustrated ferromagnetic spin-1/2 heisenberg chain in a magnetic field", Physical Review B **80**, 140402 (2009).

[58] S.-S. Zhang, N. Kaushal, E. Dagotto, and C. D. Batista, "Spin-orbit interaction driven dimerization in one-dimensional frustrated magnets", Physical Review B **96**, 214408 (2017).

[59] M. Hase, H. Kuroe, K. Ozawa, O. Suzuki, H. Kitazawa, G. Kido, and T. Sekine, "Magnetic properties of $Rb_2Cu_2Mo_3O_{12}$ including a one-dimensional spin-1/2 Heisenberg system with ferromagnetic first-nearest-neighbor and antiferromagnetic second-nearest-neighbor exchange interactions", Physical Review B **70**, 104426 (2004).

[60] M Mourigal, M Enderle, B Fåk, R. Kremer, J. Law, A Schneidewind, A Hiess, and A Prokofiev, "Evidence of a bond-nematic phase in $LiCuVO_4$", Phys. Rev. Lett. **109**, 027203 (2012).

[61] S. E. Dutton, M. Kumar, M. Mourigal, Z. G. Soos, J.-J. Wen, C. L. Broholm, N. H. Andersen, Q. Huang, M. Zbiri, R. Toft-Petersen, and R. J. Cava, "Quantum spin liquid in frustrated one-dimensional $LiCuSbO_4$", Phys. Rev. Lett. **108**, 187206 (2012).

[62] K Tomiyasu, M Fujita, A. I. Kolesnikov, R. I. Bewley, M. J. Bull, and S. M. Bennington, "Conversion method of powder inelastic scattering data for one-dimensional systems", Applied Physics Letters **94**, 092502 (2009).

[63] J. C. Leiner, J. Oh, A. I. Kolesnikov, M. B. Stone, M. D. Le, E. P. Kenny, B. J. Powell, M. Mourigal, E. E. Gordon, M.-H. Whangbo, J.-W. Kim, S.-W. Cheong, and J.-G. Park, "Magnetic excitations of the Cu^{2+} quantum spin chain in $SrCuPtO_6$", Phys. Rev. B **97**, 104426 (2018).

[64] J. Luo, J. Bai, and J. Shao, "Application of the wavelet transforms on axial strain calculation in ultrasound elastography", Progress in Natural Science **16**, 942–947 (2006).

[65] M. Bosiočić, F. Bert, S. E. Dutton, R. J. Cava, P. J. Baker, M. Požek, and P. Mendels, "Possible quadrupolar nematic phase in the frustrated spin chain $LiCuSbO_4$: an nmr investigation", Phys. Rev. B **96**, 224424 (2017).

[66] D. Dey, M. Kumar, S. E. Dutton, R. J. Cava, and Z. G. Soos, "Spin-specific heat determination of the ratio of competing first-and second-neighbor exchange interactions in frustrated spin-1/2 chains", Phys. Rev. B **97**, 064407 (2018).

[67] *ITensor*, `http://itensor.org`.

[68] B. Bruognolo, Z. Zhu, S. R. White, and E. M. Stoudenmire, "Matrix product state techniques for two-dimensional systems at finite temperature", arXiv:1705.05578 (2017).

[69] H.-J. Grafe, S Nishimoto, M Iakovleva, E Vavilova, L Spillecke, A Alfonsov, M.-I. Sturza, S Wurmehl, H Nojiri, H Rosner, et al., "Signatures of a magnetic field-induced unconventional nematic liquid in the frustrated and anisotropic spin-chain cuprate $LiCuSbO_4$", Scientific Reports **7**, 6720 (2017).

[70] G. H. Wannier, "Antiferromagnetism. the triangular Ising net", Phys. Rev. **79**, 357–364 (1950).

[71] B. Kaufman and L. Onsager, "Crystal statistics. iii. short-range order in a binary Ising lattice", Phys. Rev. **76**, 1244–1252 (1949).

[72] P. W. Anderson, "Resonating valence bonds: a new kind of insulator?", Materials Research Bulletin **8**, 153–160 (1973).

[73] L. Capriotti, A. E. Trumper, and S. Sorella, "Long-range Néel order in the triangular Heisenberg model", Phys. Rev. Lett. **82**, 3899–3902 (1999).

[74] S. R. White and A. L. Chernyshev, "Néel order in square and triangular lattice Heisenberg models", Phys. Rev. Lett. **99**, 127004 (2007).

[75] M. Mourigal, W. T. Fuhrman, A. L. Chernyshev, and M. E. Zhitomirsky, "Dynamical structure factor of the triangular-lattice antiferromagnet", Phys. Rev. B **88**, 094407 (2013).

[76] R. Rawl, L. Ge, H. Agrawal, Y. Kamiya, C. R. Dela Cruz, N. P. Butch, X. F. Sun, M. Lee, E. S. Choi, J. Oitmaa, C. D. Batista, M. Mourigal, H. D. Zhou, and J. Ma, "$Ba_8CoNb_6O_{24}$: a spin-1/2 triangular-lattice Heisenberg antiferromagnet in the two-dimensional limit", Phys. Rev. B **95**, 060412 (2017).

[77] Y. Cui, J. Dai, P. Zhou, P. S. Wang, T. R. Li, W. H. Song, J. C. Wang, L. Ma, Z. Zhang, S. Y. Li, G. M. Luke, B. Normand, T. Xiang, and W. Yu, "Mermin-wagner physics, (H, T) phase diagram, and candidate quantum spin-liquid phase in the spin-1/2 triangular-lattice antiferromagnet $Ba_8CoNb_6O_{24}$", Phys. Rev. Materials **2**, 044403 (2018).

[78] Y. Shirata, H. Tanaka, A. Matsuo, and K. Kindo, "Experimental realization of a spin-1/2 triangular-lattice Heisenberg antiferromagnet", Physical review letters **108**, 057205 (2012).

[79] Y Kamiya, L Ge, T. Hong, Y. Qiu, D. Quintero-Castro, Z Lu, H. Cao, M Matsuda, E. Choi, C. Batista, et al., "The nature of spin excitations in the one-third magnetization plateau phase of $Ba_3CoSb_2O_9$", Nature communications **9**, 2666 (2018).

[80] T. Susuki, N. Kurita, T. Tanaka, H. Nojiri, A. Matsuo, K. Kindo, and H. Tanaka, "Magnetization process and collective excitations in the $S = 1/2$ triangular-lattice Heisenberg antiferromagnet $Ba_3CoSb_2O_9$", Phys. Rev. Lett. **110**, 267201 (2013).

[81] F. Mila, "Ladders in a magnetic field: a strong coupling approach", The European Physical Journal B-Condensed Matter and Complex Systems **6**, 201–205 (1998).

[82] K. Totsuka, "Magnetization plateau in the S-1/2 Heisenberg spin chain with next-nearest-neighbor and alternating nearest-neighbor interactions", Physical Review B **57**, 3454 (1998).

[83] P. Corboz and F. Mila, "Crystals of bound states in the magnetization plateaus of the shastry-sutherland model", Physical review letters **112**, 147203 (2014).

[84] T. Coletta, T. A. Tóth, K. Penc, and F. Mila, "Semiclassical theory of the magnetization process of the triangular lattice Heisenberg model", Phys. Rev. B **94**, 075136 (2016).

[85] M. Gvozdikova, P. Melchy, and M. Zhitomirsky, "Magnetic phase diagrams of classical triangular and kagome antiferromagnets", Journal of Physics: Condensed Matter **23**, 164209 (2011).

[86] A. V. Chubukov and D. I. Golosov, "Quantum theory of an antiferromagnet on a triangular lattice in a magnetic field", J. Phys.: Condens. Matter **3**, 69 (1991).

[87] M. E. Zhitomirsky, A. Honecker, and O. A. Petrenko, "Field induced ordering in highly frustrated antiferromagnets", Phys. Rev. Lett. **85**, 3269–3272 (2000).

[88] G Koutroulakis, T Zhou, Y Kamiya, J. Thompson, H. Zhou, C. Batista, and S. Brown, "Quantum phase diagram of the S-1/2 triangular-lattice antiferromagnet $Ba_3CoSb_2O_9$", Physical Review B **91**, 024410 (2015).

[89] J. Ma, Y. Kamiya, T. Hong, H. B. Cao, G. Ehlers, W. Tian, C. D. Batista, Z. L. Dun, H. D. Zhou, and M. Matsuda, "Static and dynamical properties of the spin-1/2 equilateral triangular-lattice antiferromagnet $Ba_3CoSb_2O_9$", Phys. Rev. Lett. **116**, 087201 (2016).

[90] S. Ito, N. Kurita, H. Tanaka, S. Ohira-Kawamura, K. Nakajima, S. Itoh, K. Kuwahara, and K. Kakurai, "Structure of the magnetic excitations in the spin-1/2 triangular-lattice Heisenberg antiferromagnet $Ba_3CoSb_2O_9$", Nature Communications **8** (2017).

[91] J. Alicea, A. V. Chubukov, and O. A. Starykh, "Quantum stabilization of the 1/3-magnetization plateau in Cs_2CuBr_4", Physical review letters **102**, 137201 (2009).

[92] J. White, C. Niedermayer, G Gasparovic, C Broholm, J. Park, A. Y. Shapiro, L. Demianets, and M Kenzelmann, "Multiferroicity in the generic easy-plane triangular lattice antiferromagnet $RbFe(MoO_4)_2$", Physical Review B **88**, 060409 (2013).

[93] T. Ono, H. Tanaka, H. Aruga Katori, F. Ishikawa, H. Mitamura, and T. Goto, "Magnetization plateau in the frustrated quantum spin system Cs_2CuBr_4", Phys. Rev. B **67**, 104431 (2003).

[94] W. Fuhrman, M Mourigal, M. Zhitomirsky, and A. Chernyshev, "Dynamical structure factor of quasi-two-dimensional antiferromagnet in high fields", Physical Review B **85**, 184405 (2012).

[95] P. A. Maksimov, M. E. Zhitomirsky, and A. L. Chernyshev, "Field-induced decays in XXZ triangular-lattice antiferromagnets", Phys. Rev. B **94**, 140407 (2016).

[96] K. Momma and F. Izumi, "VESTA 3 for three-dimensional visualization of crystal, volumetric and morphology data", Journal of applied crystallography **44**, 1272–1276 (2011).

[97] S. M. Winter, K. Riedl, P. A. Maksimov, A. L. Chernyshev, A. Honecker, and R. Valentí, "Breakdown of magnons in a strongly spin-orbital coupled magnet", Nature communications **8**, 1–8 (2017).

[98] R. Verresen, R. Moessner, and F. Pollmann, "Avoided quasiparticle decay from strong quantum interactions", Nature Physics **15**, 750–753 (2019).

[99] F. Ferrari and F. Becca, "Dynamical structure factor of the J_1-J_2 heisenberg model on the triangular lattice: magnons, spinons, and gauge fields", Physical Review X **9**, 031026 (2019).